Neutron Star X-ray Binaries with MeerKAT

Kelebogile Gasealahwe
Supervisor: Dr I. Monageng [1,2]
Co-supervisor: Prof. R. Fender [1,3], Prof. P.A. Woudt [2]

2025

A thesis presented to the University of Cape Town in full fulfilment of the degree:
Doctor of Philosophy in Astrophysics and Space science
UNIVERSITY OF CAPE TOWN

[1] University of Cape Town
[2] South African Astronomical Observatory
[3] University of Oxford

Abstract

X-ray binaries make up a large fraction of transient systems. These soucres are categorized into black hole and neutron star systems based on the compact object. The dichotomy between neutron star X-ray binaries and black hole X-ray binaries was well established up to the early 2000s. However, the fundamental differences have come into question since the correlation between the radio continuum and X-ray waveband of an increasing amount of neutron stars systems revealed parallel trends to the black hole counterparts. In this study we make use of a sample set of low-mass neutron star X-ray binary systems to investigate the nature of the disc (X-ray) and the jet (radio) activity during outburst events. The sample includes SAX J1808.4-3658 an Accreting millisecond pulsar, two transitional Z/Atoll-sources Cir X-1 and XTE J1701-462 and Z-sources Cyg X-2, GX 340+0, GX 17+2, GX 13+1 and GX 349+2. To investigate the disc and jet activity the sources were observed with radio telescopes MeerKAT and AMI and X-ray telescopes *Swift*-XRT, MAXI and NICER. SAX J1808.4-3658, Cir X-1 and XTE J1701-462 were observed for the full outbursts in 2019, 2021 and 2022/23 respectively. The group of Z-sources only had single observations made in 2021. The outbursts were analysed through radio imaging and examining the lightcurves. Radio flaring events were identified in the lighcurves and the minimum energy of these flares calculated for XTE J1701-462. On the other hand, for Cir X-1, the minimum energy was calculated for the nebula by measuring the size of the structure directly from the radio image. The Cir X-1 image is a deep field L-band radio image, through which we discovered the jets breaking out of the natal supernova remnant in the structure the nebula revealed. By placing the sources on the radio – X-ray our results suggest that some neutron star X-ray binaries follow a similar trend (slope of the plane) as black hole X-ray binaries. Therefore, the physical nature of the compact object may not play a significant role in the relationship of the jet production and the accretion disc of X-ray binaries.

Acknowledgements

I am immensely grateful to my supervisors; Dr. Monageng, Prof. Fender, and Prof. Woudt. You have imparted valuable knowledge and skills. Seen my potential and shown a commitment to help improve my abilities as a researcher and grow my expertise in a field I was so new to at the start of this project. I have grown tremendously through this degree and you have greatly contributed to that.

I humbly acknowledge the University of Cape Town and my sponsors. The National Research Foundation's Doctoral Scholarship, the South African Astronomical Observatory and the prestigous Dr. Esther Mahlangu Doctoral Fellowship awarded through the Department of Science and Innovation SAWiSA award.

ThunderKAT and XKAT, being part of this collaboration is a great pleasure. It is an honour to be part of this science community. Your encouraging guidance, advice, and passion for team work is a pleasure to witness.

When I say I stand on the shoulders of multitudes, I speak of those who came before me, raised me, molded me. My family, thank you. My husband and my greatest supporter, Bakang, thank you for your love and encouraging me to chase my dreams. My children, I do it to show you that anything is possible.

I am truly humbled by the teachings of this degree and eternally grateful for the opportunity to present my work to the world.

Modimo ke naledi ya me ya bokone

Plagiarism Declaration

I, Kelebogile Verginia Stephanie Gasealahwe, know the meaning of plagiarism and declare that all of the work in the document, save for that which is properly acknowledged, is my own both in concept and execution.

Declaration on the Inclusion of Publications in a PhD Thesis

I confirm that I have been granted permission by the University of Cape Town's Doctoral Degrees Board to include the following publication(s) in my PhD thesis, and where co-authorships are involved, my co-authors have agreed that I may include the publication(s):

- The 2019 outburst of AMXP SAX J1808.4-3658 and radio follow up of MAXI J0911-655 and XTE J1701-462. Gasealahwe, K. V. S. ; Monageng, I. M. ; Fender, R. P. ; Woudt, P. A. et al. Monthly Notices of the Royal Astronomical Society, Volume 521, Issue 2, pp.2806-2813
- Radio observations of the 2022 outburst of the transitional Z-Atoll source XTE J1701-462. Gasealahwe, K. V. S. ; Monageng, I. M. ; Fender, R. P. ; Woudt, P. A. et al. Monthly Notices of the Royal Astronomical Society, Volume 533, Issue 2, pp.1800-1807
- A relativistic jet from a neutron star breaking out of its natal supernova remnant. Gasealahwe, K. V. S. ; Savard, K. ; Monageng, I. M. ; Fender, R. P. ; Woudt, P. A. et al. Monthly Notices of the Royal Astronomical Society. (Submitted for review)

Signature: 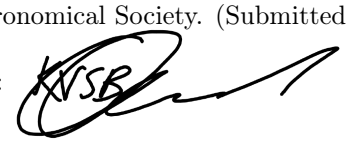 Date: 03 June 2025

Student Name: Kelebogile Gasealahwe Student Number: BNKKEL001

Contents

List of Figures

List of Tables

Chapter 1

Introduction to X-ray binaries

1.1 X-ray binaries

X-ray binaries (XBs) are objects that have either neutron star (NS) or black hole (BH) primary component paired with a companion star such that the primary accretes material from the companion (see Fig. 1.1). A neutron star is an object that remains when a star reaches the end of its evolution, with mass $\sim 1.4 M_{\odot}$ with a radius estimate of 10 km (Morton 1964, Oppenheimer and Volkoff 1939). A black hole is an object that has undergone gravitational collapse completely, does not give off any luminosity and has a mass dependence radius ($r = 2GM/c^2$, the Schwarzschild radius where M is the mass and c the speed of light) (Leibovitz and Hube 1971). The brightest class of X-ray sources in the sky are X-ray binaries and an example of which is shown in the artist impression in Fig. 1.2. X-ray binaries are typically transient sources varying on timescales of a few days as well as decaying over several tens or hundreds of days (van Paradijs and Verbunt 1984, White et al. 1984). The can also be divided into low-mass X-ray binary (LMXB, < 1 $M_{\odot}$) and high-mass X-ray binary (HMXB) systems depending on the spectral type of the donor star as well as the mass. HMXBs are typically O or B spectral type and LMXBs later than A type (Reig 2011). Transient systems recur on timescales which range from days up to years and some are periodic while others are random. Lewin et al. (1997) proposes three factors used to identify and categorise these sources; the optical wavelength, to determine the mass donating companion star's nature, the accretion flow geometry and the X-ray source mass. Lewin et al. (1997) further states the factors which determine the emission properties of accreting compact objects; (1) whether the compact object is a neutron star or a black hole, (2) in the case of it being a neutron star, the magnetic field's geometry and strength and (3) the accretion flow geometry and if the accretion from the companion is spherical or in disk form. These are the factors which dictate the region of the emission, if it is the small magnetic polar cap of the neutron star, a black hole's hot accretion disk, if there is a shock heated region within a spherical inflow or if the accretion disk and the neutron star have a boundary layer between them (Lewin et al. 1997). Moreover, the factors that influence the total luminosity, the time variability and spectral shape of the emission are the mass of the primary object and that of the accretion rate.

The process of the outbursts differ from system to system and the hardness intensity diagram (HID) (see Figure 1.3) describes the journey through the outburst cycle. This highlights the stages when the X-ray source has a hard - soft spectrum within a luminosity range. Moscibrodzka (2024) describes a low-hard state as low

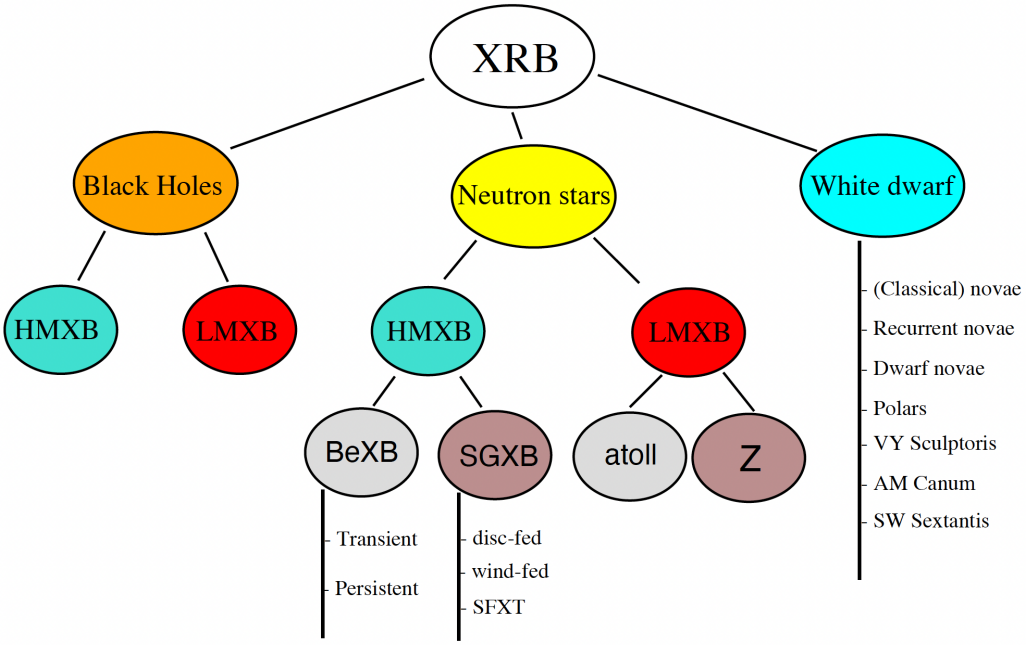

Figure 1.1: *A diagram describing the different types of X-ray binaries and the sub-classes of systems based on the mass of the companion, (note that white dwarfs are the primary components of Cataclysmic variables (CV) and the sub classes of the CVs are shown in the diagram) (Reig 2011).*

luminosity where a power law is in the X-ray spectrum with a persistent radio component. On the other hand, the high-soft state is described as having a luminosity close to the Eddington luminosity and the spectrum is thermally dominated with a quenched radio component (Moscibrodzka 2024). The general idea is that in quiescence the mass transfer rate surpasses the rate of accretion onto the primary component, the disc temperature rises while the viscosity increases (Fender and Belloni 2012) (A - B of Figure 1.3). Fender and Belloni (2012) state that the higher central mass accretion rate triggers a bright central X-ray source referred to as the outburst. Since the accretion rate exceeds the binary mass transfer rate, the mass of the disc decreases and cools off (Fender and Belloni 2012). This is a cycle in which the X-ray emission ranges between hard and soft. The luminosity brightens (A - B) and dims (D - E - F) as the jets flare up (B - C) in the radio waveband and the accretion disc puffs up (C - D) and drops in mass.

When the compact object is a black hole the inner disk is the region that emits the X-rays. This results from viscous overheating (Shakura and Sunyaev 1973) while the emission region experiences instabilities, and the influence on the nearby accretion flow may cause rapid fluctuations or quasi periodic oscillations. When the compact object is a neutron star an X-ray burst may occur; this happens when a critical mass is reached as the material accumulates onto the neutron star and there is a thermonuclear flash ignited that causes the X-ray burst (formally known as Type I bursts). X-ray bursts are also produced by accretion instabilities and these are typically referred to as Type II bursts (Taam and Fryxell 1988). Type I profiles show a spectral softening during the tail of the burst since there is a drop in the effective temperature and the neutron star atmosphere cools. The timescales for the rise of the Type I burst range between 1 – 10 seconds and the decay times are from 10 seconds to minutes (Parikh et al. 2013) (see example of Fig. 1.4 left panel). Moreover, Type II bursts show a constant temperature and the bursts can last between 2 – 700 seconds, occurring in intervals between

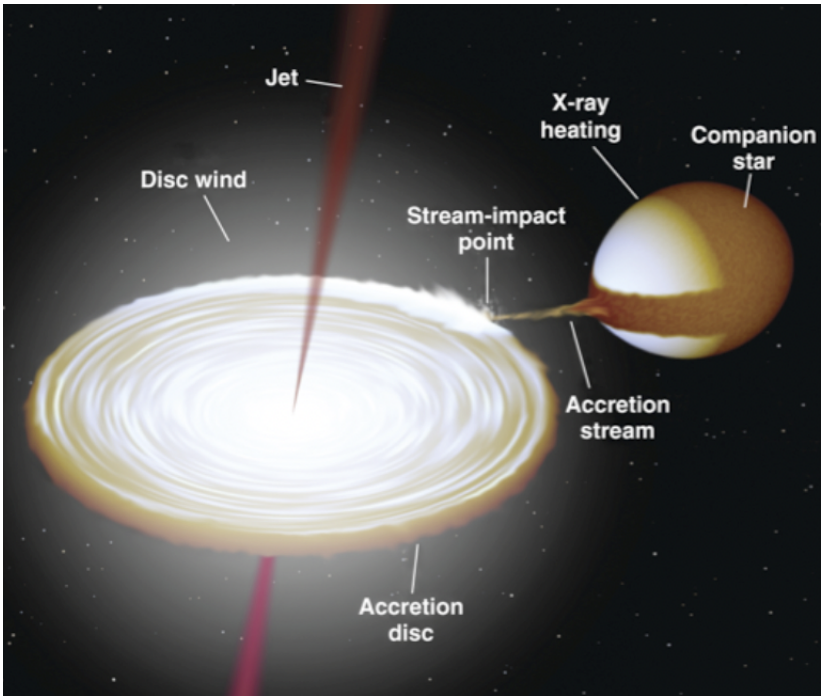

Figure 1.2: *A schematic of X-ray binary systems indicating the main components (original by Dr Rob Hynes) Fender et al. 2004a).*

7 seconds to 1 hr (the right panel of Fig. 1.4 shows an example of Type II burst). Furthermore, X-ray bursts indicate a low mass companion, which is usually a main sequence star with $M < 1M_{\odot}$ (Parikh et al. 2013). The spin of the neutron star can be inferred from the X-ray burst through the X-ray pulsations or nearly-coherent oscillations (Staubert et al. 2019).

The companion in the LMXBs with later spectral type than type A may also be very evolved like a white dwarf. There are no natural strong winds to power X-ray sources in later type or degenerate stars. There is significant mass transfer only when the critical gravitational potential lobe known as the Roche lobe is filled (an example of a Roche Lobe is shown in Fig. 1.5). X-ray heating of the accretion disk and the companion star is largely observed in the optical such that LMXBs seem as faint as blue stars (see Bradt and McClintock 1983). In the high mass X-ray binaries, companion stars are typically O type or B type stars that have optical or UV luminosities comparable to the X-ray source (Conti 1978, Petterson 1978). There is little X-ray heating such that the optical properties are largely due to the companion.

1.2 Accretion flow and spectral states

In investigating the accretion flow, it is found that the angular momentum determines the flow of the geometry, if the critical Roche lobe is filled by the companion (Lubow and Shu 1975). The stream of the material can be driven through the inner Lagrangian point, orbiting the compact object at a specific radius the angular momentum determines (Lubow and Shu 1975). The gas stream expands into a disk through the viscous interactions and conservation of angular momentum and the limiting tidal forces on the outer disk radius transfer angular momentum back to the binary orbit (see Fig. 1.5). The specific angular momentum from the stellar wind is

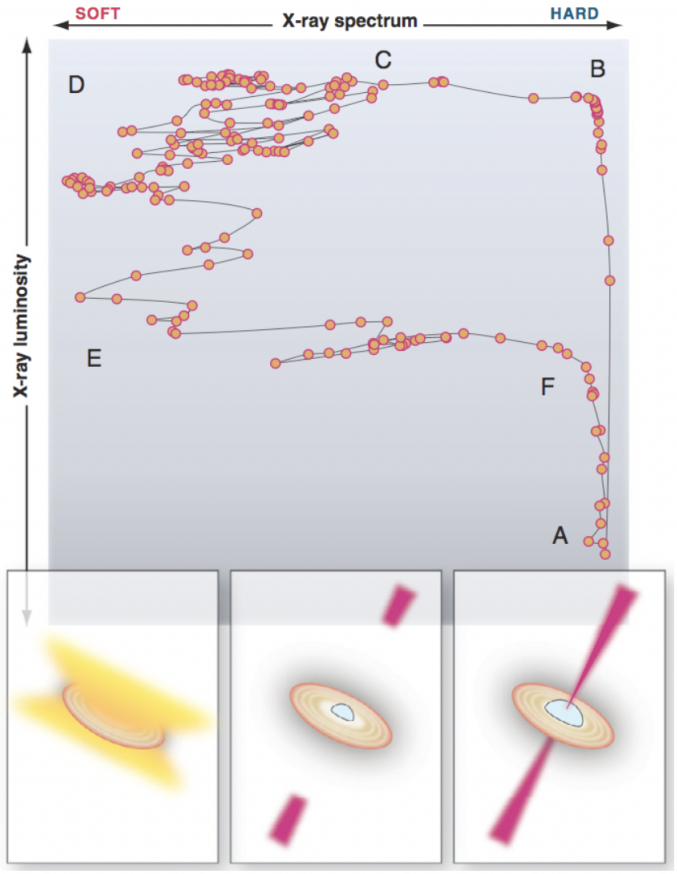

Figure 1.3: *The hardness intensity diagram of an outburst, illustrating at which points during the outburst the source has jets outflows and how the disk expands (Fender et al. 2004a).*

derived by the gradients and asymmetries in the wind through the accretion cylinder such that the magnitude of the specific angular momentum is smaller (see Fig. 1.6) (Davies and Pringle 1980, Shapiro and Lightman 1976). Therefore, the accretion disk may be weaker and for neutron stars the important environmental factors that influence the accretion flow are the neutron star magnetosphere, corona, the accretion disk and wind, as well as the companion star atmosphere and interstellar medium.

When the neutron star has a magnetic field considered to be strong (10^{12} G) the accretion flow is disrupted at several hundred radii of the neutron star and it funnels material onto the the magnetic poles (Davidson and Ostriker 1973, Pines et al. 1973, Pringle and Rees 1972). At a particular distance, the disk is disrupted by a strong magnetic field. Along the magnetic field lines is the infalling ionized plasma up to the polar caps, thus creating accretion columns on the star (eg. Fig. 1.7). The plasma is heated at the accretion columns so that the large temperatures leads to the production of X-rays such that an X-ray pulsar is observed (Lamb et al. 1973). On the other hand, a weak magnetic field ($< 10^{10}$ G) occurs when the neutron star surface and the disk being close enough to touch. The emission is dominated by the energy releases between the inner accretion disk and the boundary layer between the disk and the neutron star. van den Eijnden et al. (2021) describes that twisted magnetic field lines may play a role in the formation of jets from an accretion flow. In the two models for the jet accretion flow, the twisted magnetic field lines near the compact object are seen to launch material away

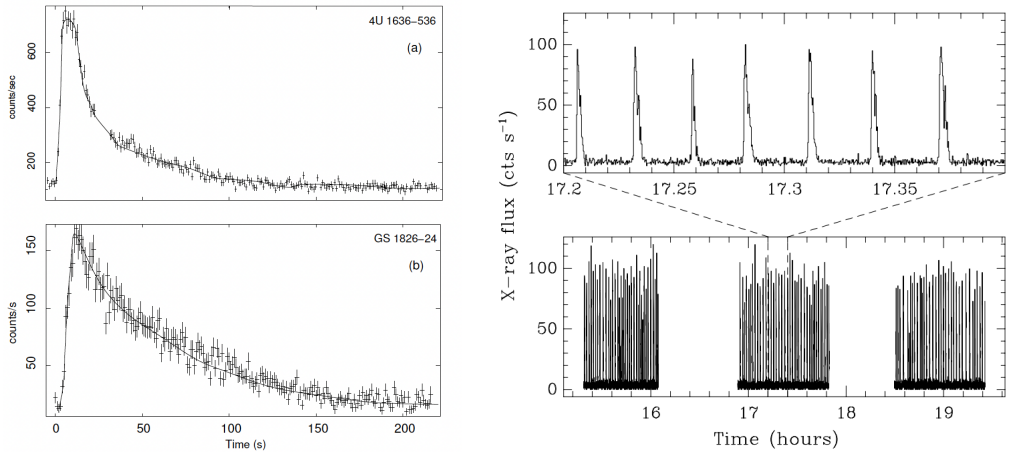

Figure 1.4: *On the left are examples of Type I X-ray burst light curves from (a) 4U 1636-536 and (b) GS 1826-24 (Parikh et al. 2013). On the right is an example of Type II bursts seen in the rapid burster MXB 1730–335 (Masetti et al. 2000).*

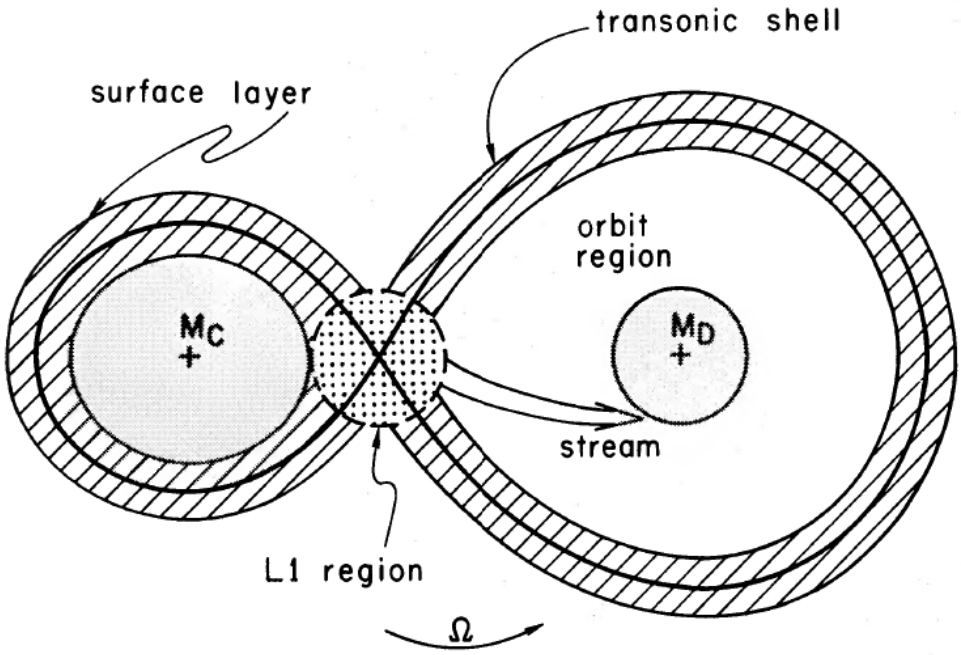

Figure 1.5: *The schematic above displays an example of a Roche lobe, including the elements therein (M_C is the companion and M_D the primary and the L1 is the inner Lagrangian point). The companion star funnels material onto the primary and this is indicated by the stream (Lubow and Shu 1975).*

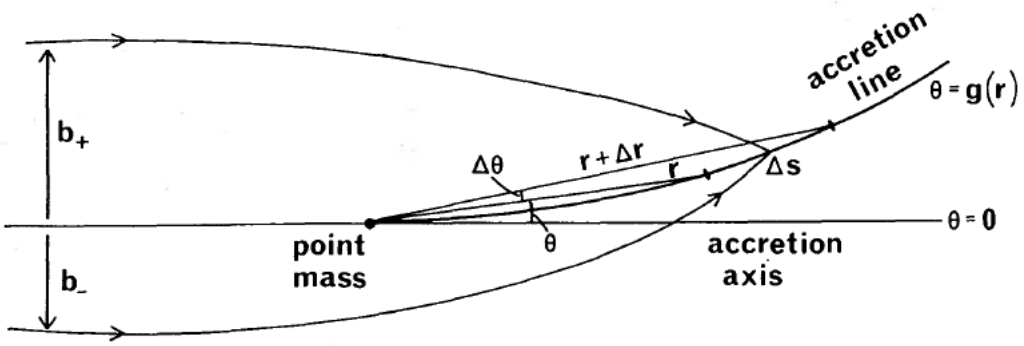

Figure 1.6: *The geometry of the accretion flow indicating the gradients and asymmetries of the wind in the system, where $\theta = g(r)$ is the accretion line (Davies and Pringle 1980).*

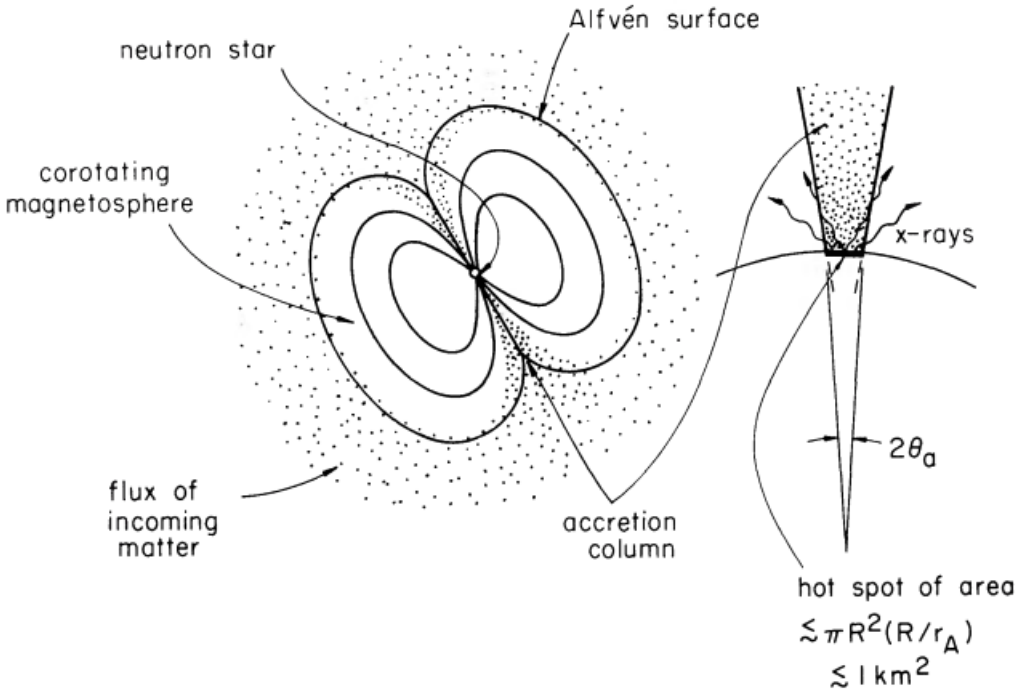

Figure 1.7: *A schematic showing a neutron star with a rotating magnetosphere influencing a hot spot from the in-falling plasma/matter through an accretion column (Lamb et al. 1973).*

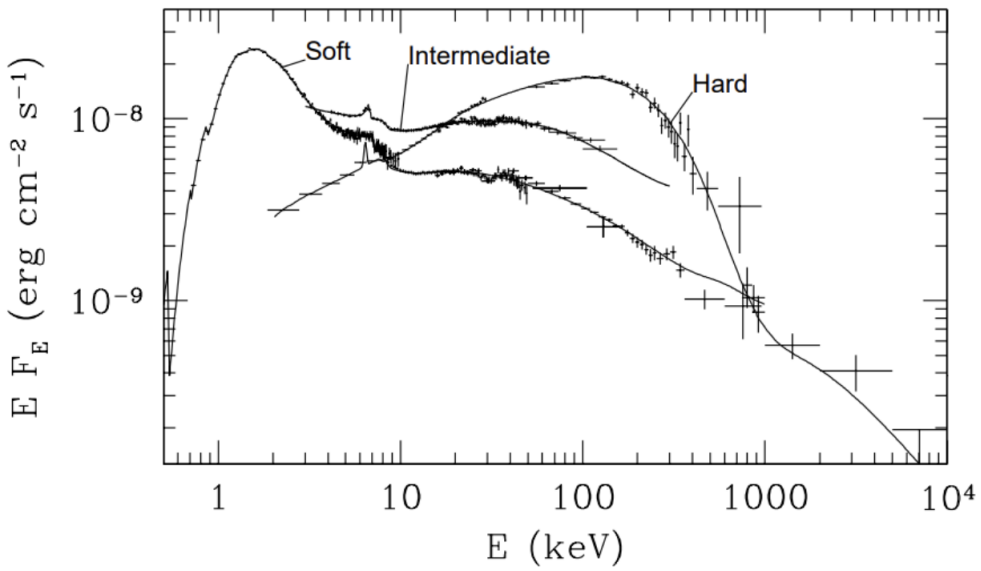

Figure 1.8: *The X-ray spectrum of Cyg X-1 illustrating the spectral states lines of the spectrum (Gierliński et al. 1999). The soft state occurs at lower energies, the intermediate state follows at higher energies and the hard state thereafter.*

from the accretion flow (see detailed descriptions in Blandford and Payne 1982, Blandford and Znajek 1977. The origin of the twisted magnetic field lines is an important factor, for accreting black hole and neutron stars the main difference for jet formation is the solid stellar surface in neutron stars (van den Eijnden et al. 2021). Furthermore, in neutron stars the anchored magnetic fields and a compact object spin are measurable through the pulsations.

Spectral state transitions

BHXBs and NSXBs undergo similar outbursts, however, there are key differences. During the outburst the spectral states change through mechanisms that influence the production and flow of the accretion disk and the relativistic jet outflows. BHXBs near Eddington luminosity often enter the very high state (VHS) (Figure 1.3 B - C) where the components representing both the thermal and the power-law are strong in the spectral energy distribution (SED) (Gallo et al. 2003). During the high/soft state (Figure 1.3 C - D) the quasi thermal component then dominates at the lower luminosities and the power law becomes steeper and extends towards the gamma-ray band. The thin accretion disk surrounding the BH is the physical component that contributes to the soft part of the X-ray spectrum (Shakura and Sunyaev 1973) (an example of the X-ray spectrum is demonstrated using the BHXB Cygnus X-1 in Fig. 1.8). This is referred to as the thermal blackbody, while a non-thermal continuum is also observed, in this instance from inverse-Comptonization of high energy plasma or corona with the soft radiation from the disk (Chakrabarti and Titarchuk 1995, Sunyaev and Titarchuk 1980). The reflection of Comptonized coronal radiation off the accretion disk is responsible for the reflection hump and Fe emission line at 30 keV and 6.4 keV respectively (Reynolds and Nowak 2003) . When the accretion rate is low, a hard state is observed, this shows a high energy dominated spectrum with a non-thermal power law component. The advection-dominated accretion flow contributes to a spectrum of this nature where you have a truncated outer thin disk and hot inner flow. During the low/hard (Figure 1.3 F - A) the luminosities drops to the lower end, below a few percent the Eddington, the spectra becomes dominated by a hard power law com-

ponent completely while a quasi thermal component is very weak and may be absent. An increasing accretion rate suggests the intermediate state (IS) is occurring. The IS occurs when the luminosities are intermediate of the hard and soft states. There is an inward expansion of the thin disk, slowing down the soft thermal and non-thermal components. Below 10^{-5} Eddington, the quiescent stage is reached having properties similar to the low/hard state. The low/hard, very high state, the intermediate state are defined through the existence of strong band-limited noise as high frequencies are reached with steepening in the power spectra, while for high/soft state a hard power law component will have very weak and absent features. The accretion rate is assumed as the driving factor between transitions of states, although Homan et al. (2001) suggests a second parameter (the Comptonizing region's size) may also play a role. During the X-ray binary's state transitions jet launching occurs. When the hard state is encountered with an increase in the luminosity the compact jet is launched (A - B Fig. 1.3). When the state transitions from hard to soft, the jet goes from being unstable to launching a major flare originating from an internal shock due to the fast transient jet colliding with the pre-existing slower jet from the hard state (B - D Fig. 1.3) (Fender et al. 2009)). The jet subsequently turns off in the soft state (D - E Fig. 1.3) and when it transitions back to the hard state it forms without a major flare.

For the neutron stars the thermal component originates from the surface and the inner disk and the Comptonized component comes from the the hot corona. The soft component similarly dominates at high accretion rates but from the neutron star surface instead, while at low accretion rates the hard state is observed. A high magnetic field also induces a hard state for the neutron star. During the hard state the spectrum may be Compton dominant with the addition of a power law component. The non thermal emission for the neutron star is in the corona Bhuvana and Nandi (2025).

The disk instability

The periodic outbursts that accretion disks undergo are influenced by thermal-viscous instabilities. Initially the mass transfer rate and viscosity are low but when rate of mass accretion onto the compact object increases it leads to rapid X-ray brightening. When the disk effective temperature reaches 104 K the instability occurs so that the hydrogen is partially ionized (Meyer and Meyer-Hofmeister 1981). This process is described by the disk instability model (DIM) in Lasota (2001).

The initial assumptions of the stability are a thermal stability and longer perturbations timescale compared to the thermal timescale. Therefore, the instabilities attributed to clumping gas rings in Lightman and Eardley (1974) are considered such that the diffuse equation in Bath and Pringle (1981), Lightman (1974);

$$\frac{\partial \sum}{\partial t} = \frac{3}{r}\frac{\partial}{\partial r}\Big[r^{\frac{1}{2}}\frac{\partial}{\partial r}\Big(r^{\frac{1}{2}}\bar{\nu}\sum\Big)\Big] \tag{1.1}$$

The average of the viscosity coefficient per unit mass $\nu = \eta/\varrho$ is $\bar{\nu}$.

$$F = \frac{9}{8}\frac{GM}{r^3}\bar{\nu}\sum \tag{1.2}$$

$$F \sim \sum^{s} r^{q} \tag{1.3}$$

The hot branch is s >0 and the cool branch has s<0 so that

$$\bar{\nu} \sum \sim \sum^{s} r^{3+q} \tag{1.4}$$

The small, local, perturbation in $\sum : \sum = \sum_0 (1 + \sigma)$ is referenced in partial such that

$$\partial \sum \partial t \approx s\sigma \tag{1.5}$$

Now s > 0 implies stability and s < 0 implies instability Smak (1982)

1.3 The Jet production and the radio spectrum

The magnetic fields in accreting BH systems provide the rotational energies of the inner accretion disk to produce relativistic jets (Hawley et al. 2015). The Blandford–Payne (BP) (Blandford and Payne 1982) mechanism describes a co-rotating mechanism between the magnetic field lines and the disk, in this case the magnetic field lines accelerate a fraction of gas in the accretion disk. It is sufficient to conclude that the BP mechanism results in accelerating outflows because the rotational velocity is only a few times smaller than the final velocity of the gas (Pudritz et al. 2006). In the Blandford–Znajek (BZ) mechanism, spinning BHs power the jet outflows (Blandford and Znajek 1977). However, some mechanisms described in Yuan et al. 2009 show that relativistic discs or spinning BHs may not be required and large-scale magnetic fields remains a key component in jet production (Cao and Lai 2019).

In the context of jet production, it is important to determine the physical processes that lead to both the appearance and disappearance of the jet. The Poynting-Robertson cosmic battery (hereafter PRCB; Contopoulos and Kazanas 1998) is used to describe the production of jets. The X-ray spectral and timing properties can be used to split low magnetic field NSXBs into two classes Z - and Atoll- sources (later described in Section 1.4.2) (Hasinger and van der Klis 1989). While the neutron stars trace a similar 'q' shape on the HID compared to the BH systems, there's a complexity with neutron stars because of the solid surface and stellar magnetic field.

The major differences between the jets of the BH and NS X-ray binaries are that the radio luminosities for NSXBs jets are 30 times less than the BH jets at similar X-ray luminosities (Fender and Kuulkers 2001, Migliari et al. 2003). Furthermore, although the radio emission is not detected in the soft state of BHXBs, it has been detected for NSXBs (Migliari et al. 2004) in the soft state. The solid surface of the neutron star and the PRCB explains the differences mentioned above. The accretion disks extend to the surface of the weak magnetic field NSXBs such that the inner most stable circular orbit (ISCO) coincides with the stellar surface, whereas the accretion extends inward to the ISCO for the BHXBs (Kylafis et al. 2012).

The low frequency, radio emission is seen as synchrotron radiation which eludes to the spiraling of relativistic electrons in magnetic fields such that photons get emitted (see example of what a synchrotron spectrum looks like in Fig. 1.10). The spectral indices, known as the slope of the radio spectrum is measured by the energy distribution of the electrons. A steep more negative slope reveals that there is a larger loss of high energy electrons. The aging and breaking refers to how radiation is fainter at higher frequencies as the electrons are overcome by a loss of energy and a break frequency is approached in the spectrum Carilli et al. (1991). Therefore creating

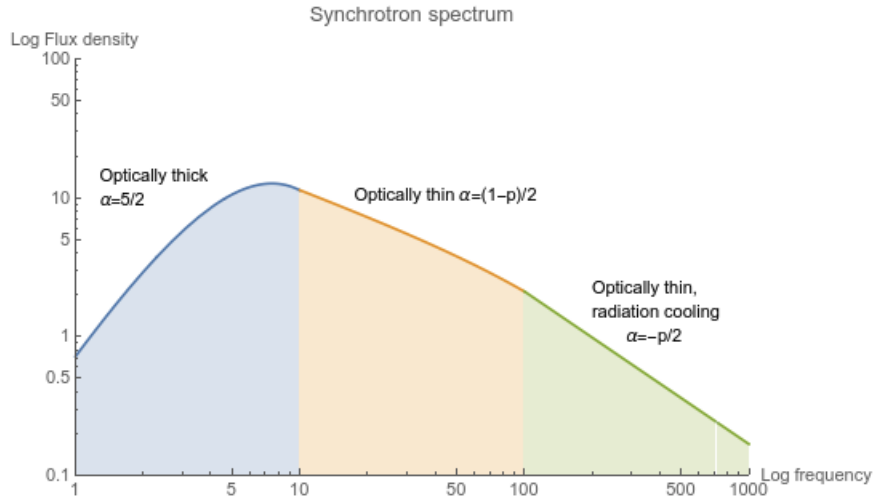

Figure 1.9: *The spectrum (see more detail in* `https://github.com/robfender/ThunderBooks` *) above illustrates the low radio frequencies such that the radiation observed is mostly synchrotron.*

a mechanism to determine the age of the electron populations in jet outflows. Self absorption occurs when at high enough electron and photons densities synchrotron photons are absorbed by other relativistic electrons such that the radio spectrum reaches a flattening or turnover. There are competing models of the SED, the Single-Shot Injection and Continuous Processes Carilli et al. (1991). The former assumes a single shot injected particle and the latter a continuous acceleration process. In the spatially distributed model, distributing the particle acceleration spatially within the lobes and around the jet hotspots is considered opposed to the single injection. Absorption mechanisms is also addressed in the models, whether synchrotron, self absorption, or free-free emission contributes to the absorption while also factoring in the magnetic fields. Overall there are multiple models to try to explain the jet activity in the low frequency range, however, the true mechanism remains uncertain.

1.4 Sub classes of low-mass NSXBs

1.4.1 Millisecond X-ray pulsar (MSP)

Slowly rotating ($< 100\,\mathrm{Hz}$), high magnetic field ($\mathrm{B} \sim 10^{12}\,\mathrm{G}$) neutron stars can change to rapidly spinning (spinning frequencies $\geq 100\,\mathrm{Hz}$) objects with weak magnetic fields ($\mathrm{B} \sim 10^{8}\,\mathrm{G}$)(Patruno and Watts 2021). LMXBs are suggested to be responsible for the spin up of pulsars by transferring angular momentum through an accretion process known as the recycling scenario (Alpar et al. 1982, Campana and Di Salvo 2018, Radhakrishnan and Srinivasan 1982, Srinivasan 2010). During the recycled scenario, a radio pulsar in the 'pulsar graveyard' (where the radio pulsed emission is turned off) moves into a prolonged state of mass transfer from the companion to the NS. This is when the pulsar in a binary system with a companion that is a non-collapsed low or intermediate mass star (example of mass range) comes into Roche lobe contact (Bhattacharya and van den Heuvel 1991, Tauris and van den Heuvel 2006). Patruno and Watts (2021) describe that large specific angular momentum transfers the mass and the NS is spun up by the accretion torques produced. Furthermore, switching on the millisecond radio pulsar once the mass transfer is complete.

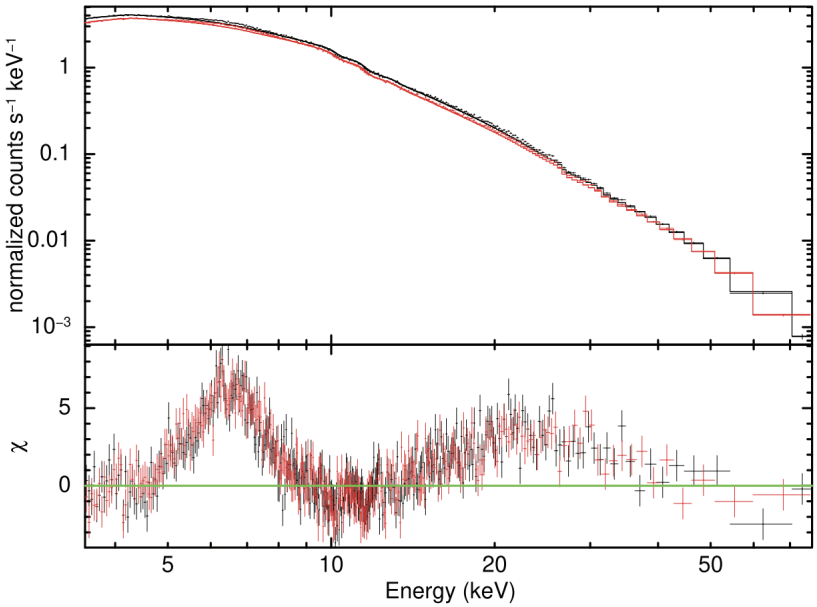

Figure 1.10: *The X-ray spectrum of a low mass NSXB 4U 1636−536 where NuSTAR's focal plane module telescopes A and B data are shown in black and red respectively. This figure from Mondal et al. (2021) highlights the Fe - K emissionline and Compton backscattering in the residuals shown at the bottom panel for energies 5 - 8 keV and 10 - 20 keV.*

An accreting millisecond pulsar (AMXP) is a accretion powered pulsar with a spinning frequency ≥ 100 Hz. AMXPs are in a low mass binary systems that experience Roche lobe overflow mass transfer with weak magnetic fields (B$\sim 10^{8-9}$ G) (Patruno and Watts 2021). The first of these AMXP systems is SAX J1808.4–3658 (Wijnands and van der Klis 1998a), discovered in 1998 to have 2.49 ms X-ray pulsations. There are over 20 AMXPs known to date (Campana and Di Salvo 2018), demonstrating that NSs in LMXB systems may spin at millisecond rates (Baglio et al. 2020).

1.4.2 The Z-source and the Atoll source

The low mass NS XRBs can be grouped into Z-sources and Atolls according to the timing properties and the shapes formed through the colour-colour diagram (CD) and the hardness intensity diagram (HID) (Hasinger and van der Klis 1989). The CD and HID describe the Z-sources shape with a horizontal branch (HB), normal branch (NB) and flaring branch (FB) (see the example CDs in Fig. 1.11) . The Atolls on the other hand are different since their CDs show what is known as an island state (I), lower banana (LB), and upper banana (UB) state, although Homan et al. (2010) further includes an extreme island state (see top left labeled example in Fig. 1.12). While Z-source appear to be quite stable as they move along the Z track, a distinguishable transient characteristic is the excess from Hard X-rays (> 30 keV) for sources on the horizontal branch and correlated to the to episodic radio emission of the jet (D'Amico et al. 2001, Farinelli et al. 2009, Paizis et al. 2006). There are six normal Z-sources, additionally XTE J1701-462 and Cir X-1 are Z-like with Atoll behaviour. Cir X-1 was shown to have timing and spectral characteristics in Shirey et al. (1999) while Ding et al. (2003) showed the evolutionary behaviour is similar to Z-sources through the hard X-ray spectra.

Among Z-sources, kHz quasi-periodic oscillations (QPOs) are observed to have similar traits. The kHz QPOs

experience an rise in frequency and at higher frequencies the amplitude decreases as the sources move along the Z-track and the mass transfer rate increase (Wijnands et al. 1998). Wijnands et al. (1998) note that the frequency of QPOs increases with the observed mass transfer rate when comparing Z- and- Atoll sources. Furthermore, shown that highest photon energy bands holds strongest kHz QPOs with maximum frequencies of 1000 – 1200 Hz and kHz QPO separation of 250 and 370 Hz (van der Klis 1998).

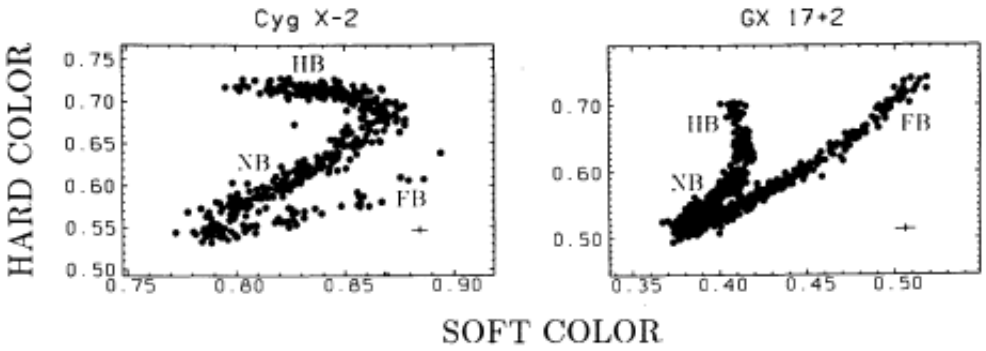

Figure 1.11: *An example of the hard vs soft X-ray Colour Diagram for a Z-source is shown above. This diagram illustrates the colour ratios a Z-source may follow through the given trajectories described as a horizontal branch (HB), normal branch (NB) and flaring branch (FB) of the Z track (Hasinger and van der Klis 1989).*

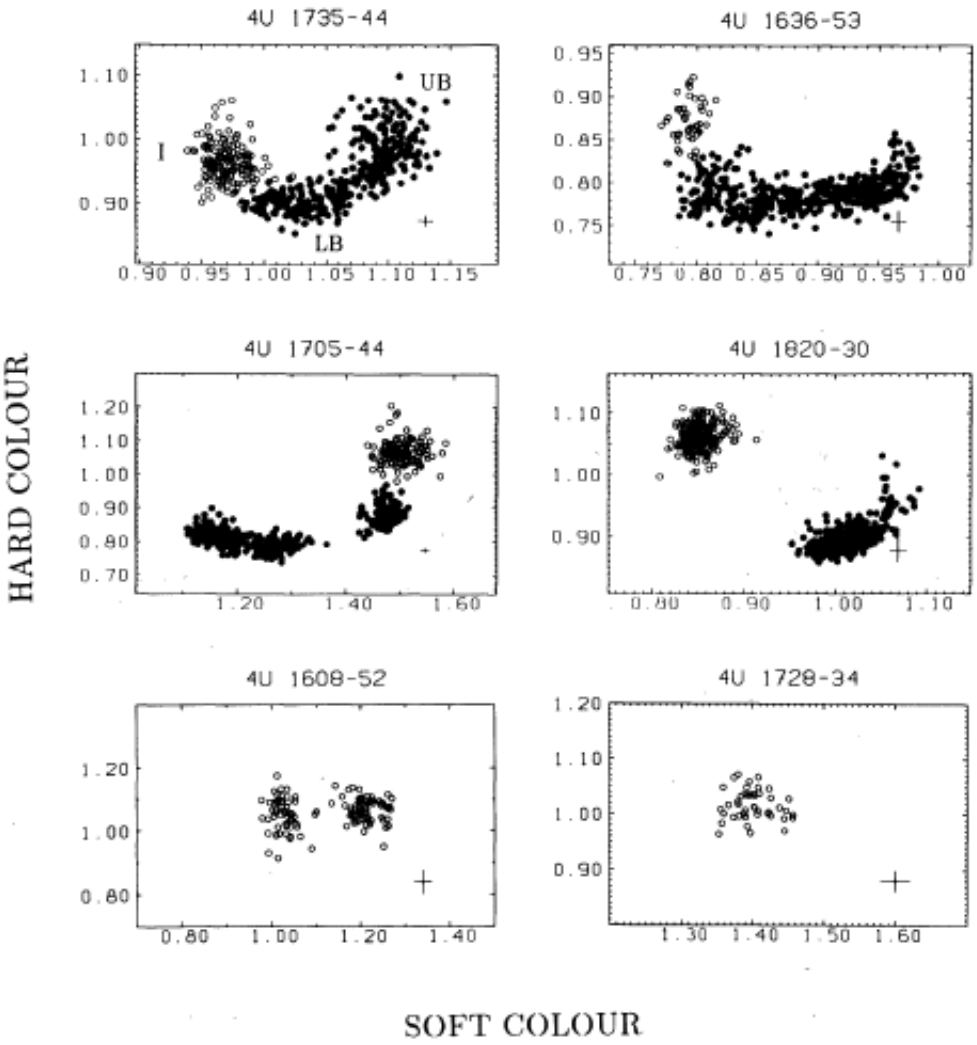

Figure 1.12: *An example of what an Atoll source looks like on the the hard vs soft X-ray CD. In the diagram above, the different positions of the color ratios for Atoll sources are called banana with an upper (UB) and lower (LB) branch and isolated islands positions (Hasinger and van der Klis 1989).*

1.5 Radio X-ray correlation

Relativistic jets and the existence of a powerful compact power law X-ray emission which is often associated with the inner part of the accretion flow indicates the presence of a black hole. This implies that there is a correlation between accretion onto compact objects and relativistic outflows known as the disk–jet phenomenon (Begelman et al. 1984, Falcke and Biermann 1995, Rawlings and Saunders 1991). Supermassive black holes and stellar mass black holes are similar regarding jet morphological and spectral properties as observed from the cores in radio and X-rays (Merloni et al. 2003). Merloni et al. (2003) suggest it is commonly assumed that jets are launched from the inner most part of the accretion flow , in this case the similarities can be studied on systems of the same class. Therefore radio and hard X-ray emission can be studied to directly probe the mechanisms and fundamental parameters in the black holes such as the black hole central mass, angular momentum and disk/jet coupling.

X-ray features, such as the relative strength of a soft blackbody component around 1 keV, the spectral hardness seen at high energies, the luminosity from the X-ray as well as the timing properties are used to classify black hole systems (Nowak 1995, Poutanen 1998). During the low/hard state the power-law spectrum is dominant and a low luminosity with an exponential cut off above 100keV is observed itself with no soft or thermal component. This is related to synchrotron radiation with a steady self-absorbed outflow in the radio spectrum. Exceedingly low X-ray flux characterises the quiescent state, it may be considered the hard state with low radiative efficiency as well as accretion rates. Thermal radiation dominates during the high/soft state as well as the core radio emission becomes non detectable which may be due to the jet suppression. When the very high state follows, components representing power-law and thermal conditions both provide considerably to the distribution of the spectral energy.

Gallo et al. (2003) determine the observed radio and X-ray luminosities scales correlation in the following manner

$$\frac{L_{radio}}{L_X} \propto (L_X)^{-0.3} \tag{1.6}$$

$$L_R \propto L_X^{0.7} \tag{1.7}$$

Gallo et al. (2003) state that as that X-ray luminosity decreases, there is a powerful relation between the radiative jets and X-rays. The self-absorption effects influence a non-linearity between radio luminosities as well as the total jet power ($L_{/rmradio}$ and $L_{/rmjet}$ respectively) for a flat spectrum defined by an optically thick jet model. Furthermore, Blandford and Königl (1979), Falcke and Biermann (1996), Markoff et al. (2001) determine $L_{radio} \propto (L_{jet}^{1.4})$ such that the relationship becomes

$$L_{radio} \propto (L_{jet}^{x}) \tag{1.8}$$

and the scaling for the fractional jet power is represented by

$$\frac{L_{jet}}{L_X} \propto (L_X)^{\frac{0.7}{x-1}} \tag{1.9}$$

Based on observational data, the slope of the relation for BHXBs may be between 0.6 and 0.7 (see Corbel et al. 2013, Gallo et al. 2014) such that

$$\frac{L_{jet}}{L_X} \propto (L_X)^{\frac{0.6-0.7}{x-1}} \tag{1.10}$$

In the following section, the correlation (i.e slope) between the jet (radio) and the accretion disk (X-ray) are determined and compared to the 0.6 – 0.7 BHXB correlation.

1.5.1 The NSXBs radio X-ray correlation

Migliari and Fender (2006) studied a sample of NSXBs, which include Z-sources, Atolls, AMXPs and other accreting pulsars. The authors confirmed that two of the sources, 4U 1728-34 and Aql X-1, were in the hard spectral state. As a result, they were able to use the slope (β) from the power law model $L_R \propto L_X^{\beta}$ to compare the radio : X-ray correlation in BH systems (note, the slope is denoted Γ in Migliari and Fender (2006)). The slope determined by the authors for 4U 1728-34 is $\beta = 1.40 \pm 0.25$ and with Aql X-1, it is $\beta = 1.38 \pm 0.23$. The slope the authors determine for the set of Z-sources is 0.66 ± 0.07. Therefore, Migliari and Fender (2006)

assumes $\beta_{BH} \sim 0.7$ and $\beta_{NS} \gtrsim 1.4$ (due to the hard spectral type nature) so that $L_R \propto L_J^{1.4}$ becomes $L_J \propto L_X^{0.5}$ for BHs and $L_J \propto L_X$ for NSs. The authors state that the accretion rate and jet power coupling could be different in the two types of XRB systems. Furthermore, assuming L_X and $\dot{m}$ is similar for BHs and NSs, consolidates the above statement.

Migliari and Fender (2006) argues however, that L_X and $\dot{m}$ must be different in the two types of XRBs. Assuming that there is radiative efficiency for NS systems because it accretes onto the NS solid surface (contrary to the event horizon of the BHs). The linear relation thus becomes $L_J \propto L_X \propto \dot{m}$. If L_J, and not the accretion rate $\dot{m}$ and L_X are assumed to be similar for both types of XRBs. Due to $\dot{m} \propto L_X + L_J$ and estimating $L_X > L_J$, the relation in Eddington units for NSXBs is
$L_X \sim \dot{m}$
With the same accretion and jet power coupling for BHXBs, the relation becomes $L_J \propto L_X^{0.5} \propto \dot{m}$ for BHXBs. Migliari and Fender (2006) conclude that the difference between the $L_R : L_X$ correlation for the two types of XRB systems is that the NSs states in their sample are dominated by X-rays and the BHs are dominated by the jet.

Deller et al. (2015) discusses the transitional MSP PSR J1023+0038 and it's $L_R|L_X$ relationship. Although they do not determine a slope similar to the ~ 0.7 (BHXB) or ~ 0.6 (Z-sources) found in Migliari and Fender (2006), they do propose that the NSXBs that have similar correlation slopes to BHXBs are propeller systems that cease at high accretion rates because most of the material is expelled.

More recently, Gallo et al. (2018) lead a study investigating the radio X-ray correlation for a group of NSXBs. The authors determined that the BHXBs follow a slope $\beta = 0.59 \pm 0.02$ and NSXBs a slope of $\beta = 0.44^{+0.05}_{-0.04}$, such that they are consistent within 2.5σ. Separating the NSXBs by class of AMXP and Atoll they find slopes of $\beta = 0.27^{+0.09}_{-0.10}$, and $\beta = 0.71^{+0.11}_{-0.09}$ respectively (Gallo et al. 2018). Therefore, reinforcing the question of how close the correlation of NSXB compares to BHXBs.

1.6 Research sample

The research sample consists of four main sources, these are all neutron star systems considered to have low mass companions. I list the objects below and discuss the details of their discoveries and some of the outbursts previously observed.

1.6.1 SAX J1808.43658

SAX J1808.43658 (referred to as SAX J1808 hereafter) is a low mass X-ray binary that is the prototype of the millisecond X-ray pulsars (AMXP). The source was initially discovered in 1996 with the BeppoSAX satellite and the detection of 401 Hz pulsations a couple of years later showed this as the first AMXP known (Wijnands and van der Klis 1998b). The sample size of the AMXPs has grown, although SAX J1808 is still the archetype of AMXPs (Campana and Di Salvo 2018). SAX J1808 is located 3.5 kpc away and has short, semi-regular outburst with recurrence times of 2 – 4 years. To date, 6 outbursts have been observed since its discovery. An AMXP is characterised by coherent pulsed emission with nearly sinusoidal oscillations from a localised emission region like a hot spot on the surface of the neutron star. The dynamically relevant stellar magnetosphere creates the

hotspot through channeling in-falling plasma as the accretion columns impact the neutron star's surface within confined regions near the magnetic poles (see schematic in Fig. 1.7).

An abundance of details about this NS are revealed through the pulsations and these include the compactness of the star (Poutanen and Gierliński 2003) and the phase evolution, further showing the star and the binary's spin evolution through time (Hartman et al. 2008). Bult et al. (2020) reported that there is no measurable spin that is powered by accretion. (Bult et al. (2020) finds a binary orbit of 2:01 hr as seen in Chakrabarty and Morgan (1998) as well as a perculiar long term variation of the binary period. After monitoring SAX J1808 within the first decade of discovery it was observed that highly non-conservative mass transfer or the spin-orbit angular momentum interchange within the companion star (Hartman et al. 2009, Patruno et al. 2012) is the reason for an expanding binary period with an unusually fast rate ($\sim 3.5 \times 10^{-12} ss^{-1}$ Hartman et al. 2009), similar to the short term orbital variability seen in millisecond black widow radio pulsars. Bult et al. (2020) reports the outbursts of 2011, 2015 later showed that the orbital expansion rate was itself evolving rapidly but a lack of data points could not show the rate at which this evolution is occurring (Patruno et al. 2017, Sanna et al. 2017a).

1.6.2 Circinus X-1

The source, discovered in 1971, showed it as a BH (Margon et al. 1971). Later, the Type I X-ray bursts discovered in 1985, indicated that the system has a NS primary (Tennant et al. 1986), which was later confirmed by the Rossi X-ray Timing Explorer (RXTE) (Remillard et al. 2006) detection of Type I bursts (Linares et al. 2010b). An extensive jet powered nebula surrounds the central source and is believed to be its nascent origin (Fig. 1.13 shows the total intensity of the nebula) (Heinz et al. 2013, Tudose et al. 2006) There are regular outbursts occurring every 16.6 days. The X-ray lightcurve has shown perculiar bright intensities over the years since discovery. Linares et al. (2010b) suggested that Cir X-1's accretion rate changes, along with the temperature changes of the neutron star are potentially the cause of the drop in the average X-ray intensity and the type I X-ray bursts reappearing, respectively. In this case the X-ray bursts appear to occur at the lower accretion rate range, since the thermonuclear instabilities are suppressed by the high accretion rates (Cornelisse et al. 2003). It does not, however, fully explain why there were no bursts observed during the years 2006 and 2010 after which there had already been a drop in X-ray emission. Linares et al. (2010a) proposes the behaviour is a result of cooling the neutron star during the period from 2006 and 2010 by means of a thermal-hysteresis such that Cir X-1 had stabilised nuclear burning with no 'burst-like' behaviour before the source is cooled. In the thermal-hysteresis scenario the accretion rate changes of the X-ray behaviour could also be the reason for the more powerful and 'burst-like' flows generated in the neutron star and therefore the stronger synchrotron emission (radio) observed from 2006. Long-term monitoring shows that the scenario is most likely because the average as well as peak intensity of the X-ray lowered enough during 1996 and 2006 and over that period the radio luminosity has increased and decreased again by a factor of 100-1000. Type I bursts were again later observed by Armstrong et al. (2013), who argue that there is likely no connection to the radio behaviour since the Type I burst have a thermal hysteresis dependence and the powerful radio flaring largely relies on the accretion rate. However, Russell et al. (2024) have since shown, for an accreting NSs system that there is a relation between Type I bursts and radio emission.

Cir X-1 is a source that has synchrotron flaring behaviour and superposed mini flares that are often opti-

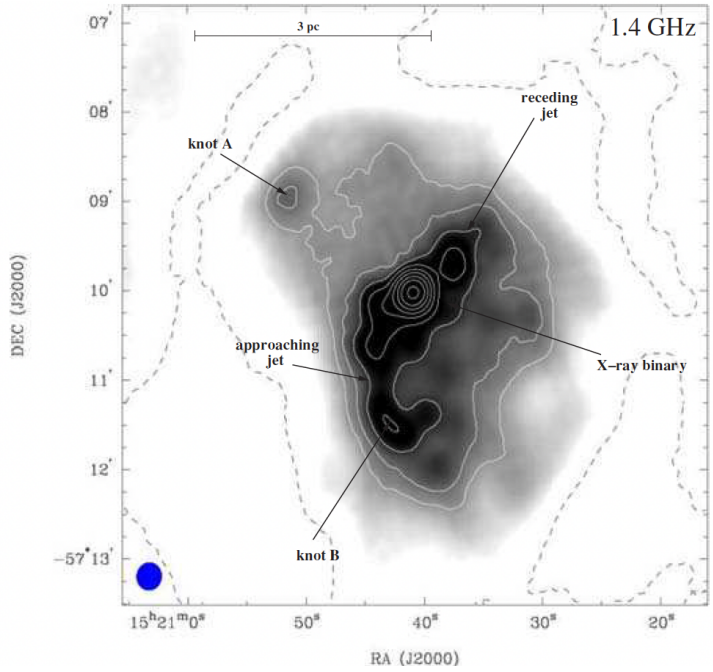

Figure 1.13: *The radio total intensity map of Cir X-1, taken with ATCA (1.4 GHz) during August 2001 (Tudose et al. 2006).*

cally thin in nature. It is suggested that these arise due to further jet-ISM (interstellar medium) shock action which could be related to knot re-brightening because similar timescales occurrences of the relativistic ejections re-brightening when lowered radio flaring epoch was observed (Fender et al. 2004b)). Fender et al. (2004b) proposed that there are two mechanisms thought to be the cause of the large disparity of radio luminosity during the long period observation. One is large flares which are apparent or intrinsic as a result of Doppler beaming or a possible change of the accretion rate. The jets of Cir X-1 have been argued to have a small, varying angle to the line of sight and regular precession is thought to not fully explain the apparent bimodal behaviour since the precession period is very long. The jet may be precessing aperiodically, however, and would require an aperiodic oscillation which occasionally aligns to the strong boosted line of sight. The radio brightening could be tested with complete high cadence resolution coverage to check whether it is a result of stronger relativistic boosting because is would have more contraction time (blue shifted) in the evolution of the approaching blobs. In the instance of identical physical properties, the relativistic moving blobs must be observed to be brighter and be evolving faster when seen close to the motion axis. Current facilities like MeerKAT in the S-band frequency range will be able to reveal more details on the precession of the jets.

1.6.3 XTE J1701-462

XTE J1701-462 (XTE J1701 hereafter) was first discovered on 18 January 2006 with the All sky monitor onboard the Rossi X-ray Timing Explorer (RXTE) (Remillard et al. 2006). Early results showed that XTE J1701 acts like a Z-source due to the nature of the CDs and the timing similarities consistent with Z-sources (Homan et al. 2006a,b, 2007b). Later, it was shown that the source transitioned into an Atoll source towards the end of the outburst (Homan et al. 2007a). The 2006 outburst revealed two types of tracks on the CDs displaying a Z and a 'v-like' (see the plot on the right of Fig. 1.11) track during the Z-source stages (Homan et al. 2007b). After the analysis of the RXTE observations of XTE J1701 it is found that for the later Atoll stage either

the disk or the NS evolves along $L_X \propto T^4$. The blackbody radius, and inner disk radius of the NS remain constant during this evolution and the inner disk which was similar to the NS radius was determined by the ISCO. Through the Z-source stage, however, the disk or the NS moved away from the $L_X \propto T^4$ and the inner disk radius increased as the source intensity increased that could be local Eddington limit signature in the disk. As a result, it is assumed that the magnetosphere of the NS may play a key role in how the inner disk and the disk structure evolves and it is tenable that the inner edge of the disk can't move beyond the ISCO or the radius of the magnetosphere. The ISCO sets the inner disk when the magnetosphere is pushed against by the gas pressure during the Atoll source stage. Through the Z-source stages, however, due to the disk thickening from radiation pressure, it is found that the disk gas pressure decreases, magnetosphere enlarges while the inner disk radius finally heightens. As a result, the magnetospheric radius can set the inner disk radius, while varying with the mass accretion rate during the Z-source stage (Ding et al. 2011).

Two scenarios are thought to explain the the relation between Z- and- Atoll sources; first is a similarity of the two types of sources and the differences are a result of their difference in $\dot{m}$, and second that their differences are a result of additional parameters like the magnetic field strength of the NS surface as well as the disk inclination instead of the $\dot{m}$ (Hasinger and van der Klis 1989). Scenario 1 can lead to the Z- and- Atoll patterns interchanging for the sources that have large ranges in $\dot{m}$ such that these sources switch between the Z- and- Atoll source behaviours. This scenario was excluded because it had not been observed. Hasinger and van der Klis (1989) therefore argued that scenario 2 is the reason for the difference between the Z and Atoll sources, suggesting that the mass accretion rate and the magnetic field strength of the NS surface could be bigger in the Z sources as opposed to the Atoll sources, indicating a different evolutionary history.

Later work revealed that XTE J1701 was shown to be a transitional source, where both Z and Atoll behaviour was observed through the Z and 'v-like' tracks on the CD evolving to an Atoll pattern (Homan et al. 2010, Lin et al. 2009a). XTE J1701 therefore plays a crucial role in linking the Z and Atoll sources (Lin et al. 2009a). Although it is observed that the mass accretion rates largely differentiate between Z- Atoll, exploring the characteristics of the structures, the accretion disk evolution, the hard X-ray emission and magnetic field of the NS could further explain the evolution of Z to Atoll source. Furthermore, the surface magnetic field strength of the NS appears to be larger in the Z sources compared to Atolls.

XTE J1701 evolved from Cyg-like to Sco-like behaviour (where a Cyg-like object shows a Z-track named after Cyg X-2 and a Sco-like source shows a 'v-like' track named after Sco X-1 Homan et al. 2010) during the Z source phase when the 2006/7 outburst occurred. It was after this Z-source period that it then evolved into an Atoll. This links the evolution to the mass accretion rate instead of the magnetic field strength since it was improbable that the magnetic field strength varied so largely during a short period of time. Due to the transient Z-source evolving to an Atoll at low luminosities, one may propose that the magnetic field strength will not change or evolve that fast and it could be due to two different types of NSXBs. However, no clear differences between the magnetic field strengths in the Z and Atoll sources exist, as indicated by scenario 1 from Hasinger and van der Klis (1989). Therefore the source appear as either a Z or Atoll source at low or high accretion rates Ding et al. (2011). Fender et al. (2007) report on the variable radio counterpart of XTE J1701 off the discovery outburst in January 2006. They demonstrate a coupling of the X-ray and radio luminosities, similar to those established for other Z-sources. The authors interpret their results as a relation between accretion flows and relativistic jet production.

1.6.4 Cyg X-2

Cygnus X-2 is a low mass NS XRB that is categorized as a Z-source due to the X-ray colour ratios, and therefore has high X-ray luminosities (Hasinger and van der Klis 1989, Spencer et al. 2013). Below 20 keV, the spectrum of Cyg X-2 and persistently bright NS LMXBs is usually described by a soft and hard component, where the accretion disk attributes to the soft component as reported from Mitsuda et al. (1984, 1989) eastern model and White et al. (1986, 1988) western model from the NS while the hard component is assumed to come from the corona (see full discussion in Farinelli et al. 2009). Wijnands et al. (1998) discovered QPOs in Cyg X-2 which were reported as two simultaneous kHz QPOs with frequencies 500 Hz and 860 Hz. They further discuss that the higher frequency QPO increased when a transition from the left end of the HB to the upper NB occurred and Cyg X-2 is part of the majority of Z sources displaying kHz QPOs (Wijnands et al. 1998).

Spencer et al. (2013)'s investigation with the Very Long Baseline Interferometry (VLBI) and Swift XRT of Cyg X-2 show that the there is a sub-relativistic jet when the source is on the HB. Examining the radio data alongside the X-ray data, it was shown that the radio observation from 22 and 23 February 2013 revealed a 0.59 mJy single core and weakened the following day towards the bright head in the south east direction which was 141° east of north. The X-ray spectrum was described by a soft multicolour disc component and unsaturated thermal Comptonization within the plasma temperature (kTe $\sim$ 3 keV) with a large Thomson optical depth ($\tau \sim 5 - 10$, depending on the geometry) (Farinelli et al. 2023).

1.7 Research Aim and motivation

The aim is to investigate the jet outflows of the low-mass NSXBs sample described in the section above. This was achieved through a multiwavelength study focusing on radio and X-ray analyses by determining the lightcurves of the sources in both bands. Comparing the disk and jet nature of each source via the radio – X-ray correlation for the outbursts observed. An effort to quantify the jet/disk coupling and address an open question of the behaviour of this jet/coupling for NSXBs. The radio and X-ray luminosities and the correlation plane are presented at 5 GHz (where a flat spectral index is assumed to support consistency in the radio flux measurements) for the radio and 1 - 10 keV for the X-rays. As a result the data is analysed within this parameter space. The research makes use of radio and X-ray telescopes (discussed in Chapter 2), these telescopes and instruments are discussed below along with the tools required and used for the data reduction.

The thesis includes papers published in the high impact Monthly Notices of the Royal Astronomical Society. These results are revealed in Chapters 3, 4 and 5 and my contribution to the papers was as lead investigator and writer of the objects studied. This was completed under the guidance of my supervisors and the co-authors through an iterative process of comments, corrections and suggestions. In the third paper (Chapter 5) I maintained the leading role of the paper, particularly for the observational radio part and the theoretical simulation part was lead by the second author.

Chapter 2

Telescopes and radio data analyses tools

2.1 Telescopes and Instruments

The physical specifications of the telescopes and instruments used in this research are described below. This selection of telescopes is motivated by the resolution capabilities, the potential high cadence of observations and the accessibility due to the collaboration of the project. Particularly, ThunderKAT for MeerKAT monitoring and in partnership *Swift*KAT for the X-ray follow-up with the *Swift* telescope. Furthermore, the tools of the analyses and the data reduction processes are discussed.

2.1.1 MeerKAT

The MeerKAT radio telescope, located in the Karoo of the Northern Cape province in South Africa, is a precursor to the Square Kilometre Array (SKA). The telescope is operated by the South African Radio Astronomy Observatory (SARAO) and has numerous key science programmes. This particular project is facilitated under the ThunderKAT LSP, one of the MeerKAT Large Survey Projects (MLSPs), for image-domain (explosive) radio transients (Fender et al. 2016). MeerKAT comprises 64 dishes, each with a diameter of 13.5 m. Fig. 2.1 shows a schematic of a typical MeerKAT dish. MeerKAT currently uses three frequency bands known as the UHF band, the L band and the S band that have frequency ranges 0.58–1.015 GHz, 0.9–1.67 GHz and 1.75–3.5 GHz respectively. The maximum baseline is 7.7 km, and the minimum is 29 m. The wideband mode has 32768 channels, providing ≈ 0.1 km/s resolution for narrow-band zoom modes. The telescope has an optimization for point-source sensitivity due to the requirement among all of the LSPs [2].

2.1.2 *Swift*

The Swift Gamma Ray Burst Explorer was chosen October 1999 as NASA's next MIDEX mission and launched on the 20 November 2004 (Burrows et al. 2005). There are three instruments onboard Swift, a Burst Alert Telescope (BAT) that identifies gamma-ray bursts and establishes the position of the bursts within arcminutes

[2](see more details and specifications here `https://skaafrica.atlassian.net/wiki/spaces/ESDKB/pages/277315585/MeerKAT+specifications`)

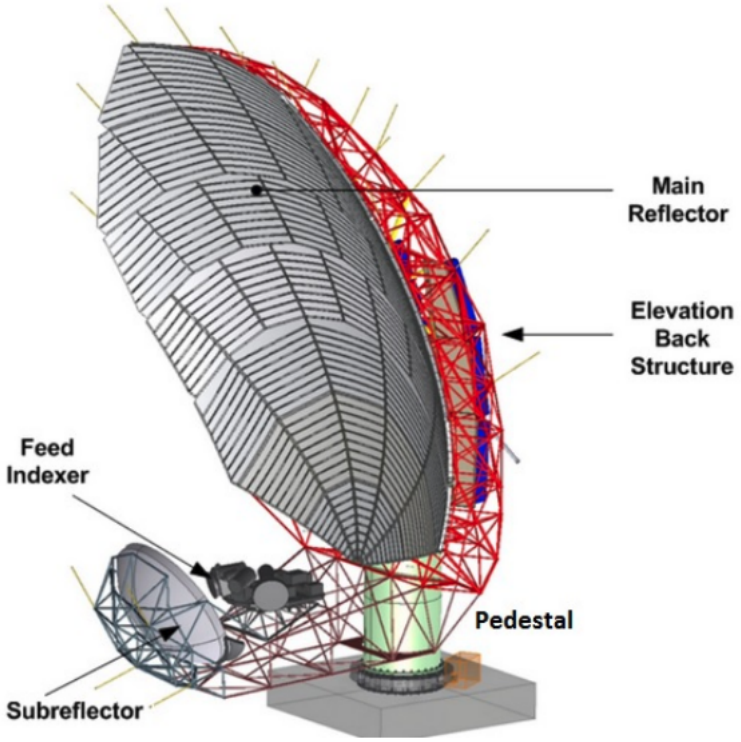

Figure 2.1: *The structure and main elements (including the main and sub reflectors, the back structure elevation, index feeder and and pedestal) of the MeerKAT radio dish are shown in the above schematic (Jonas and MeerKAT Team 2016).*

with a 15 - 150 keV energy range ; the Ultraviolet/Optical Telescope (UVOT) that has a sensitivity limit of magnitude 24 in 1000s, a position accuracy of 0.3 arcseconds within the wavelength range of 170 650 nm; as well as the X-ray Telescope (XRT) that detects between 0.2 - 10 keV (Burrows et al. 2005). The instruments are combined to provide a powerful multiwavelength observatory. XRT focuses the X-rays onto a thermoelectrically cooled CCD, using a grazing incidence Wolter I telescope. The instrument is described in detail in Fig. 2.2 as it is encased in the telescope tube Fig. 2.3. In the complete image of the instrument, there is a door which protects the mirror while it is launched. There is a thermal baffle such that the front end of the mirrors have a warm environment, preventing thermal gradients within the mirror module which the Point Spread Function could be warped from. The JET-X flight spares contributed towards the mirrors and they were calibrated at the Panter X-ray Calibration Facility of the Max-Planck-Institute fur Extraterrestrische Physik in 1996 and in 2000. The focal plane camera is held in the composite telescope tube that contains a single e2v CCD22 detector. A thermoelectric cooler (TEC) is coupled with the thermal radiator which is mounted on the anti-solar side of the spacecraft and is designed to cool the detector off to -100 C. Figure 2.4 shows the field of view (large circle) for an XRT observation where the points in this image represent each X-ray photon.

2.1.3 AMI

The Arcminute Microkelvin Imager (AMI) centered at 15.7 GHz spans between an antenna diameter of 3.7 m and 12.8 m for the small array (SA) and long array (LA) respectively. The SA (not used in this research) has 10 antennas with 45 baselines and LA has 8 antennas with 28 baselines and the configurations of the antennas are shown in Figure 2.5. The primary beam is 20.1 arcmin and 5.5 arcmin while the synthesized beams is 3 arcmin

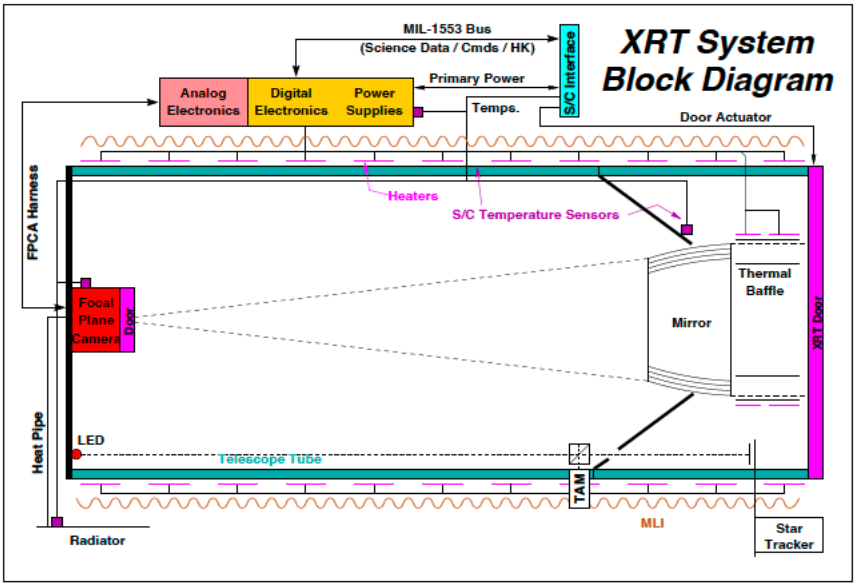

Figure 2.2: *The XRT block design is shown above where a focal plane camera door and XRT door are highlighted to protect the the mirror. FPCA is the Focal Plane Camera Assembly and TAM is the Telescope Alignment mirror (Burrows et al. 2005).*

and 30 arcmin for the SA and LA respectively. The bandwidth is 4.3 GHz, while there are 6 channels and the system temperature is 25 K (Zwart et al. 2008).

2.1.4 MAXI

All Sky Monitors (ASMs) and surveying are investigated through the MAXI mission (see telescope overview in Figure 2.6). Astronomers are alerted through MAXI of GRBs, X-ray novae and flare-up increases of the X-ray sources upon occurrence (Matsuoka et al. 2009a). Special time scale variabilities like long term periodic and quasi-periodic signals of X-ray sources can be determined through the long term data. The two types of cameras; the gas slit camera (GS) and solid-state slit camera (SSC), have energy ranges of 2 - 30 keV and 0.5 - 12 keV respectively (Matsuoka et al. 2009a). Multiwavelength observations and collaborations with other ground based and space observatories can be promoted through MAXI and the systematic observations of variable activity of Active Galactic Nuclei (AGNs) and black holes help determine where and how variable activities are produced (Matsuoka et al. 2009a). Monthly and bi-annual categories of lightcurves are provided through the MAXI mission and give long term variabilities. A map of soft X-rays and medium energy X-rays is possible through MAXI and the maps provide line features like Oxygen X-ray lines, very useful for investigating geocoronal recombination lines and the evolution of hot gas in the Galaxy (Fujimoto et al. 2007, McCammon and Sanders 1990, Tanaka and Bleeker 1977).

2.1.5 NICER

NICER, formally known as the Neutron star Interior Composition ExploreR, is a NASA Goddard space mission which is jointly led by Massachusetts Institute of Technology (MIT), the commercially rendered partners and an inter-university scientific team (Gendreau et al. 2012a). The telescope is onboard the International Space Station (ISS) (see Figure. 2.7 illustrating the components of the telescope) . The mission is to perform rotation

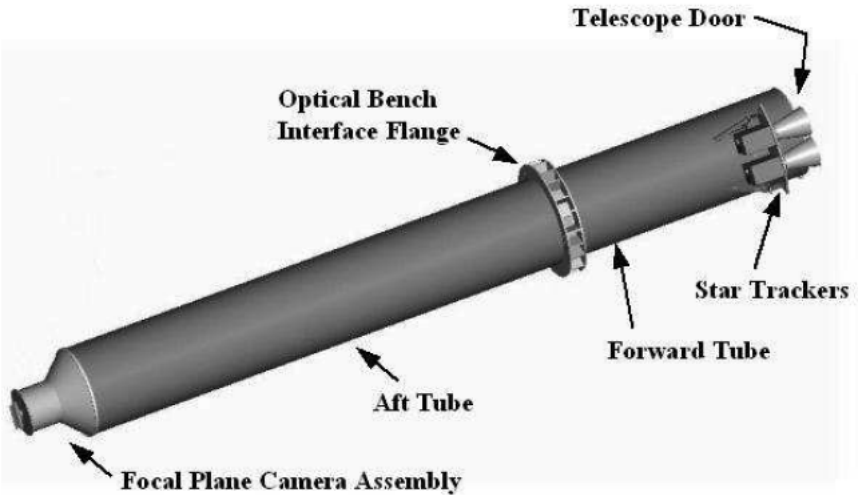

Figure 2.3: *The telescope tube in which the XRT instrument is encased is displayed, indicating the telescope door, the optical bench interface flange, the forward tube, the star trackers, the aft tube and where the focal plane camera assembly is. The focal length of the telescope is 3.50 m and the total instrument length is 4.67 m while the diameter is 0.51 m (Burrows et al. 2005).*

resolved spectroscopy of NS which are rapidly rotating, such that we can infer the structures, dynamics and energetics of the constrained models of these objects (Gendreau et al. 2012a). The key science outcomes intended for this mission is to consolidate the predictions of nuclear theory regarding mass-radius relationships. This is achievable through analysis of the NS' X-ray flux modulation from rotating hot spots on the object. Gendreau et al. (2012a) further discuss that the results from *NICER* lightcurve analysis have a $\pm$ 5 % radius measurement uncertainty. The lower and upper energy ranges are 0.2 keV and 12 keV respectively (Gendreau et al. 2012a). The timing and energy resolutions are 100 ns and 85 eV at 1 keV respectively. And the collecting area and photon time tagging precision from the telescope is adequate for X-ray measurements of general relativistic Shapiro delay in binary systems to determine the masses of NSs. Moreover, where the orbital periods of rotating or accreting millisecond pulsars are longer than a few days, the masses are obtained through Shapiro's delay using the pulse time of arrival measurements (Gendreau et al. 2012a).

Table 2.1: *The table below describes the telescope sensitivities. The field of view (FOV), the resolution and the rms noise achieved for observations.*

Telescope	FOV	Resolution	RMS noise	Reference
MeerKAT L-band	1 square degree	4 - 10 arcseconds	3 μJy	[1]
AMI LA	-	0.7 arcseconds	60 μJy	(Zwart et al. 2008)
Swift	23.6 x 23.6 arcminutes	18 arcseconds	-	(Burrows et al. 2005)
MAXI				(Matsuoka et al. 2009a)
GSC:	1.5degree x 160degree	18% (5.9 keV)	-	
SSC:	1.5degree x 90degree	$\leq$150 eV (5.9 keV)	-	
Nicer	15 arcmin^2	3% 6 keV, 8% 1 keV	-	(Gendreau et al. 2016)

[1] `https://skaafrica.atlassian.net/wiki/spaces/ESDKB/pages/277315585/MeerKAT+specifications`

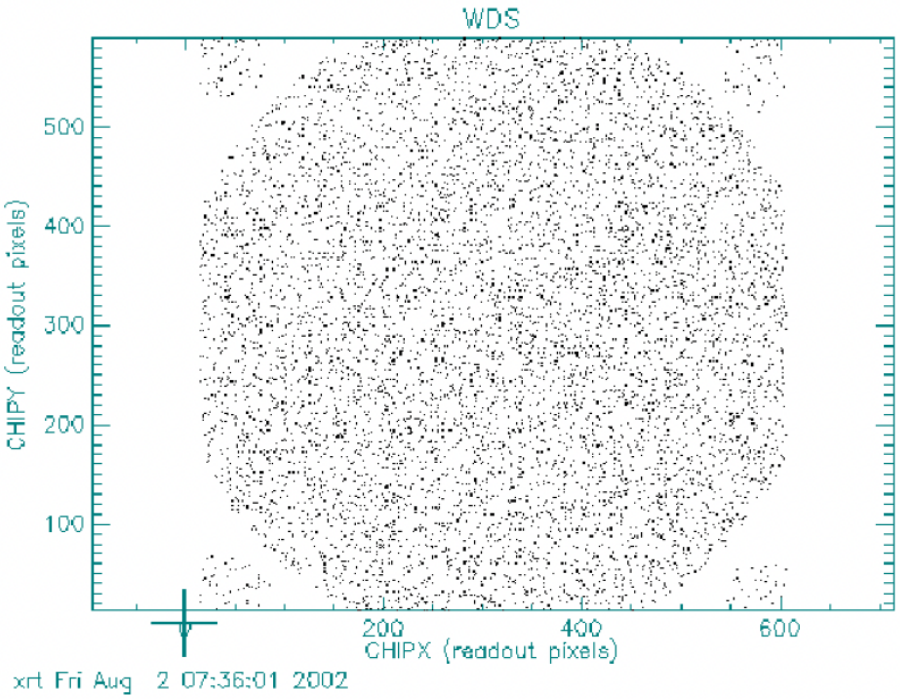

Figure 2.4: *The figure above describes the field of view taken with XRT. The* ^{55}Fe *calibration source placed on the inner camera door produces the large circle and the smaller circles in the image (CCD corners) are produced by sources which illuminate the CCD corners throughout the flight (Burrows et al. 2005).*

2.2 Radio data analysis tools

The MeerKAT radio data were processed and imaged using the OXKAT pipeline, thereafter, the flux measurements were obtained via two analyses software namely CASA and PYBDSF by fitting 2 Dimensional Gaussians and all the errorbars quoted are 1σ for thesis. These tools are briefly described below.

2.2.1 CASA

The CASA software is used to reduce and analyse radio astronomical data. By means of advanced calibration, CASA images and analyses data via the PYTHON interface visualization (CASA Team et al. 2022). The architecture builds on C++ and FORTRAN programming languages. McMullin et al. (2007) states the architecture includes a command line interface and user reference documentation. The key application elements are a table based data model, facilities compatible with loading external format data, a python interface that includes scripting, utilities for displaying and editing data, image formation and deconvolution McMullin et al. (2007).

2.2.2 OXKAT

OXKAT is a semi-automated pipeline, used to calibrate and image MeerKAT radio data. Making use of PYTHON[1] and CASA (see CASA Team et al. 2022, McMullin et al. 2007), WSCLEAN (Offringa et al. 2014) , CUBICAL (Kenyon et al. 2018) and other radio astronomy software, the raw visibilities in the measurement sets undergo flagging and reference calibration. Heywood (2020) states thereafter, imaging is processed, then self calibration

[1] `https://www.python.org/`

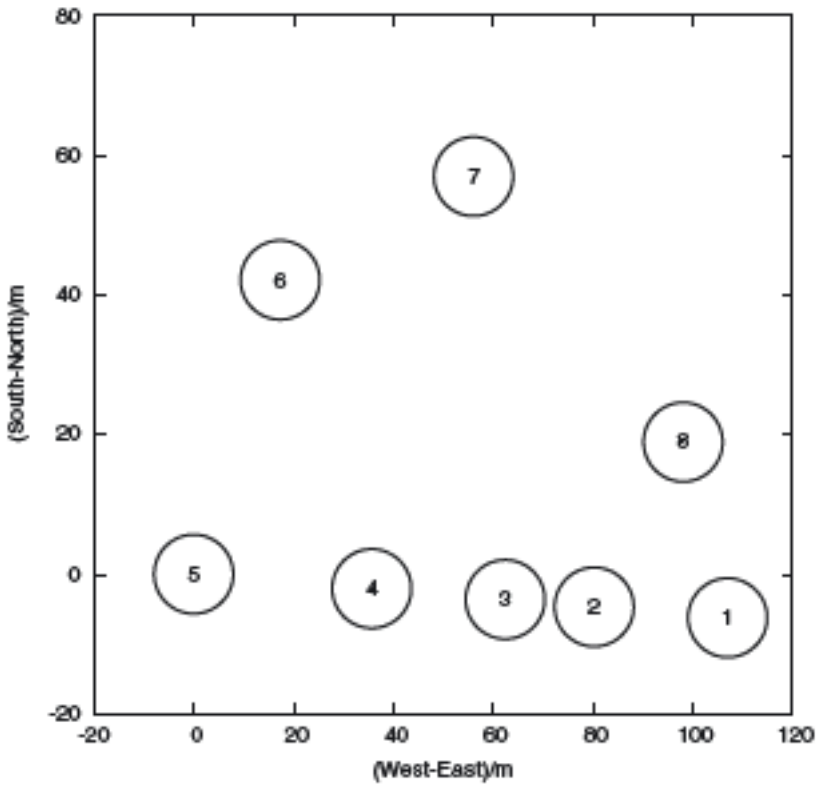

Figure 2.5: *The LA array configuration of AMI (Zwart et al. 2008).*

and the optional direction dependent calibration. The scripts are submitted to Ilifu/ Institute for Data Intensive Astronomy (IDIA) and Centre for High Performance Computing (CHPC) clusters via slurm and PBS jobs schedulers. These are generated automatically while catering for MeerKAT data processing HPC facilities.

To image the data I follow the standard imaging process described above with the default parameters. The gain and visibilities were determined using the 1GC script. By creating a job to be executed and run on the Ilifu/IDIA and CHPC clusters the following commands are run; python setups/1GC.py idia and $./submit1GCjobs.sh$. The plots produced during this step are similar to the example in Fig. 2.8. Once the initial step was completed, the data were flagged creating radio image outputs (see left panel of Fig. 2.9). Thereafter the self calibration was performed using the 2GC script such that the data products were similar to the example of XTE J1701 products in Fig. 2.9 right panel.

2.2.3 PyBDSF

The development of PYBDSF (initially named PYBDSM) to process the LOw Frequency ARray 1 (LOFAR) data. PYBDSF is now compatible for other telescope data, like MeerKAT, ASKAP, Mileura Array). This is a source extraction software and in radio astronomy that is a Gaussian fitting process since interferometer images use a Gaussian when convolved after the deconvolution (Mohan and Rafferty 2015).

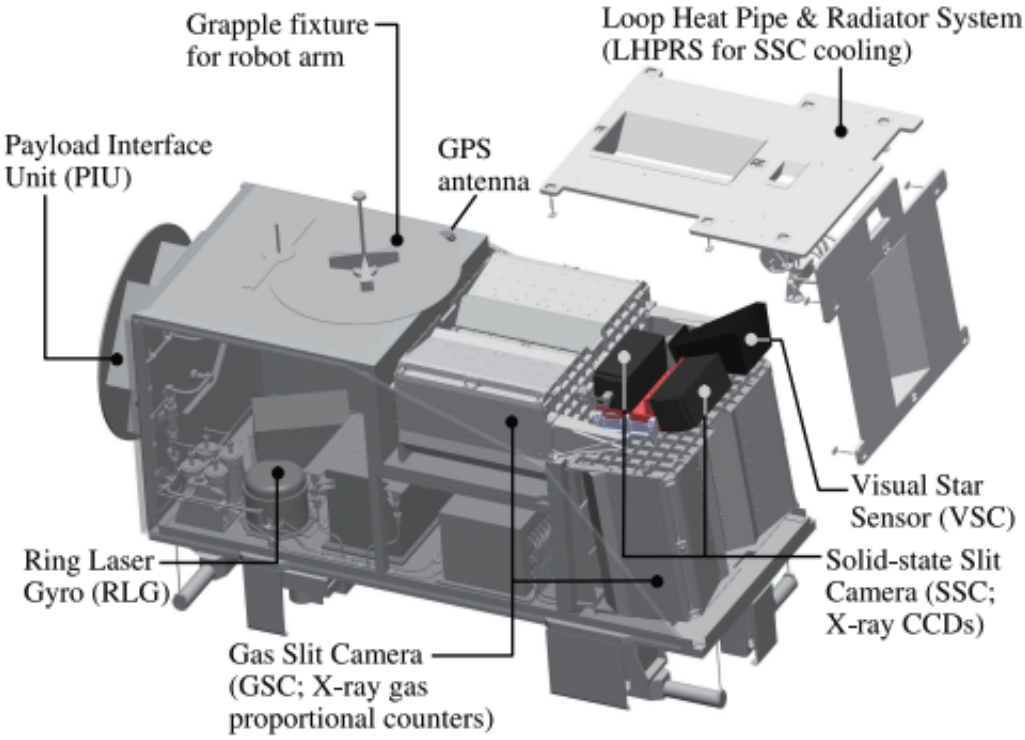

Figure 2.6: *The MAXI telescope and the major subsystems are displayed in the above figure and these are the payload interface unit, the ring laser, gas and solid state slit cameras, the GPS antenna, the visual star sensor and the loop heat pipe radiator system (Matsuoka et al. 2009a).*

2.3 X-ray data analysis tools

The X-ray data from the telescopes, Swift [1], MAXI [2] and NICER [3] are all retrievable from their respective web interfaces. The data products include background, response, auxilary files etc. which are used in XSPEC to plot and fit the spectra. This is an X-ray spectral fitting package that was developed for the EXOSAT observatory but designed to be adaptable to other instruments. It generates a simulated spectra given a theoretical model (see example for model created for the SAX J1808 *NICER* spectra Fig. 2.12) and a detector response (see map on the process of fitting Fig. 2.10) (Arnaud 1996). The X-ray spectra are fit within the 1 - 10 keV range to maintain consistency for the radio : X-ray correlation plane (all the previous data sources are fit within this range). The (DISK + BBODYRAD) model was used to fit the spectra due to the physical nature of accreting neutron stars and the initial parameters were subject to the individual sources (ie., n_H values which assume unabsorbed local flux around the source, see example details of the fit parameters in Fig. 2.12 and the spectral fit in Fig.2.13).

In case the spectral fitting is not required to extract the flux measurements, eg. the MAXI lightcurve data is used. WebPIMMS together with literature values of the sources n_H and X-ray spectral index values were used to convert to unabsorbed flux measurements within the correct energy band (1 10 keV).

[1] `https://www.swift.ac.uk/user_objects/`
[2] `https://maxi.riken.jp/top/lc.html`
[3] `https://heasarc.gsfc.nasa.gov/docs/nicer/nicer_archive.html`

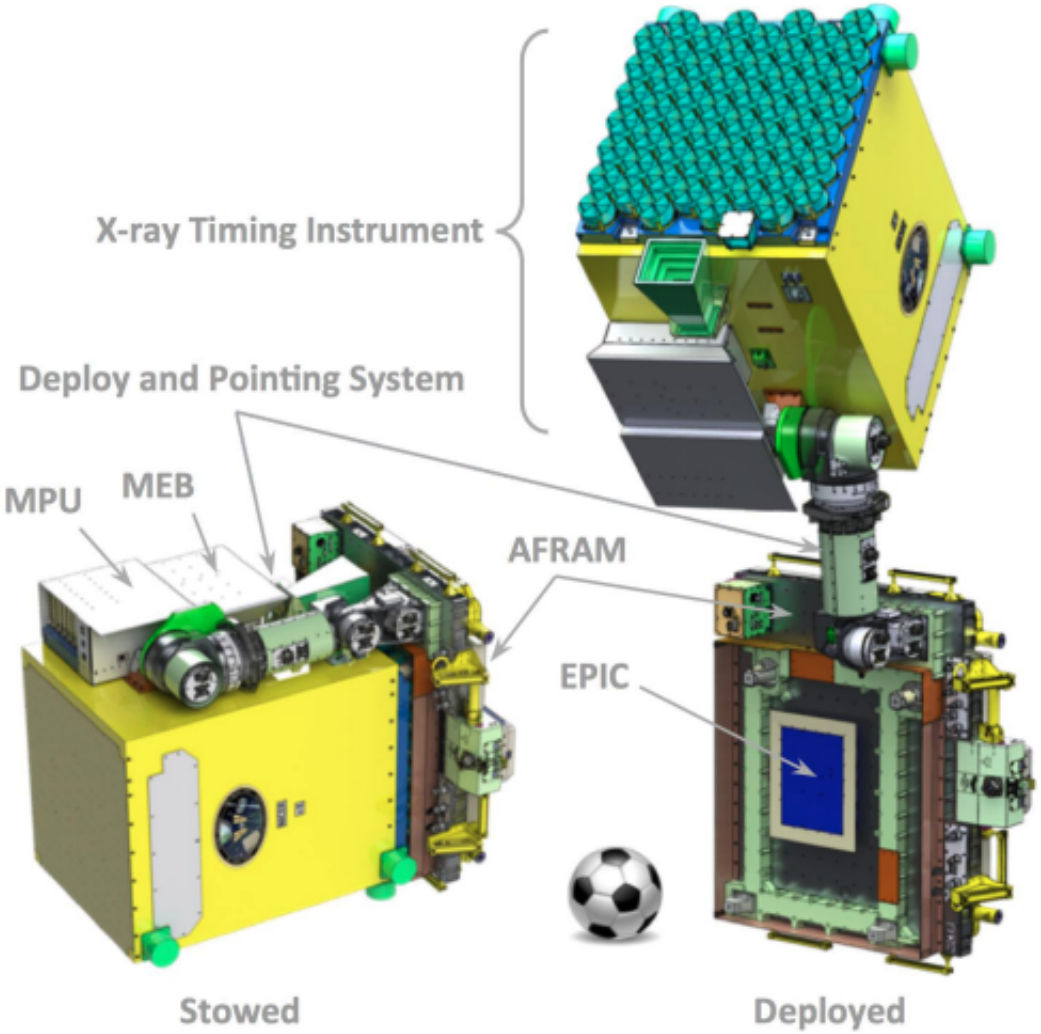

Figure 2.7: *The NICER telescope, illustrating the X-ray timing instrument and the deploy and pointing systems (Gendreau et al. 2016)*

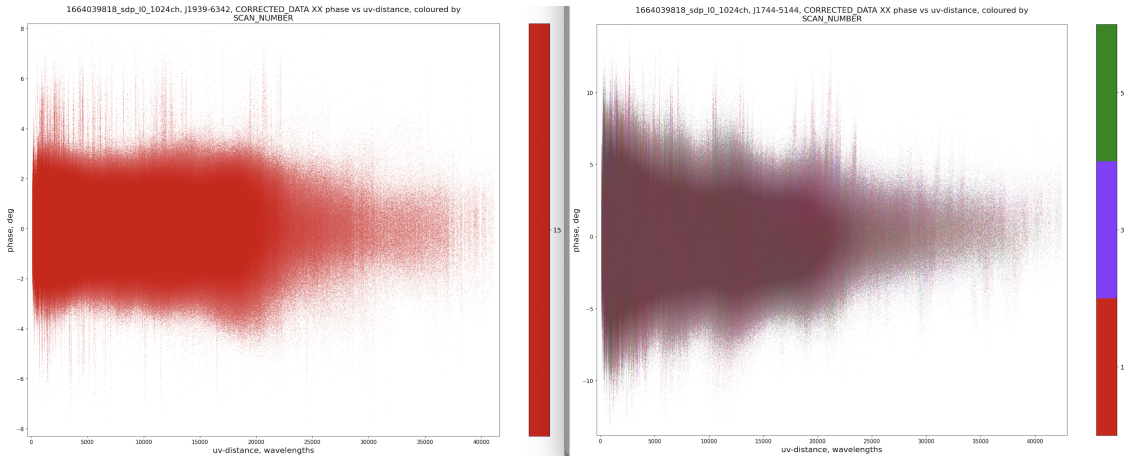

Figure 2.8: *Examples of visibility plots for the primary and secondary calibrators left and right panel respectively of an XTE J1701 observation.*

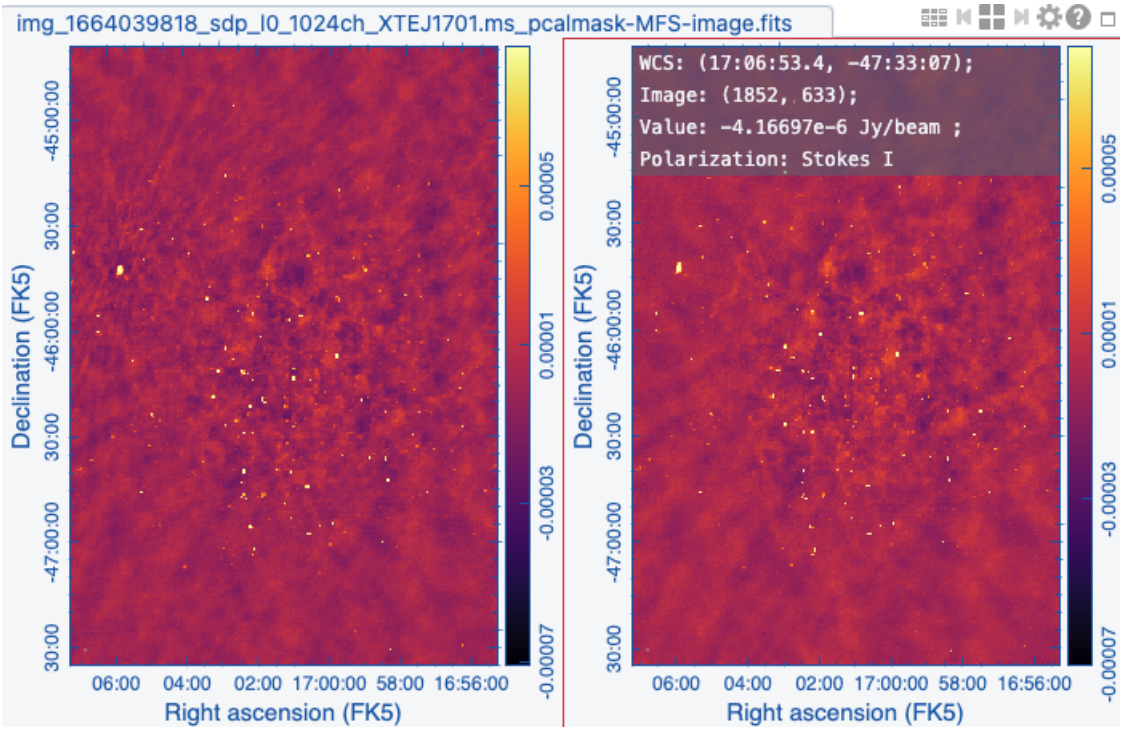

Figure 2.9: *For an observation of XTE J1701 the process of flagging and removing RFI produces the image on the left. Once the flagging is complete, self calibration is performed and the image is improved. The image on the right shows this improvement of the radio image.*

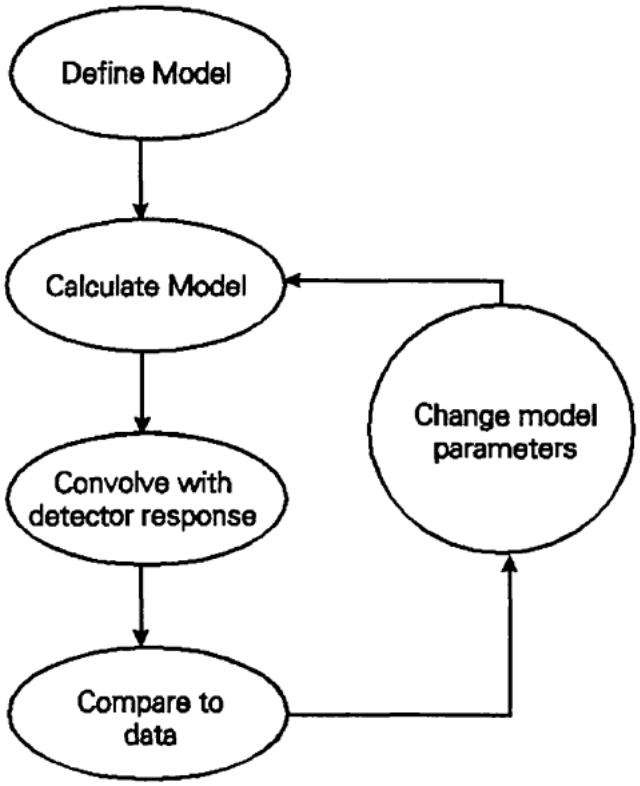

Figure 2.10: *The* XSPEC *fitting process of spectra given a theoretical model with initial parameters described in the map above (Arnaud 1996).*

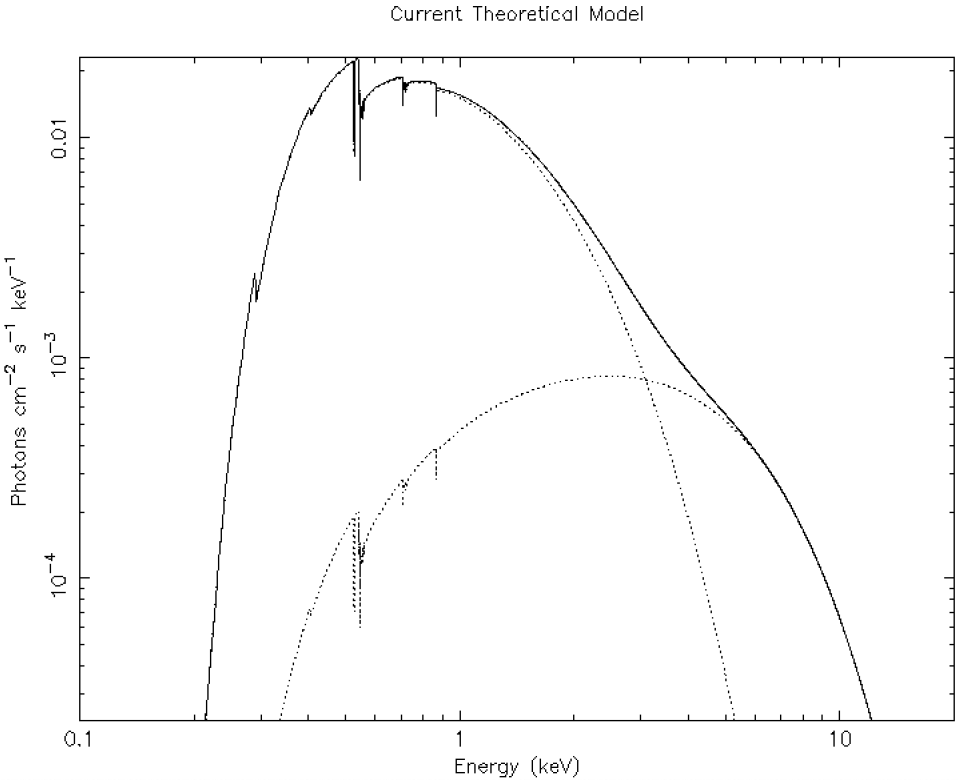

Figure 2.11: *The figure above illustrates the theoretical model (*DISK + BBODYRAD*), used as input for fitting the spectra from SAX J1808's NICER data.*

```
XSPEC12>fit 10000
                                   Parameters
Chi-Squared  |beta|/N    Lvl    7:lg10Flux         8:Tin        9:norm         10:kT       11:norm
248.91       0.018593      2      -10.2767      0.551208   1.00000e+24       1.46003      0.598719
248.91       0.0185631     2      -10.2767      0.551209   2.96283e+19       1.46003      0.598719
============================================================
 Variances and Principal Axes
                7        8        9       10       11
 5.8618E-18|  0.0000  -1.0000   0.0000   0.0000   0.0000
 2.8364E-04|  0.0000   0.0000   0.0000   0.8235   0.5673
 6.2863E-02|  0.0000  -0.0000   0.0000  -0.5673   0.8235
 1.1607E-01|  1.0000   0.0000   0.0000   0.0000   0.0000
 8.4109E+73|  0.0000   0.0000  -1.0000  -0.0000   0.0000
------------------------------------------------------------

============================================================
  Covariance Matrix
        1           2           3           4           5
   1.161e-01   1.679e-03   3.123e+36   9.850e-03  -1.666e-02
   1.679e-03   3.104e-04   4.155e+34   2.072e-03  -3.205e-03
   3.123e+36   4.155e+34   8.411e+73   2.327e+35  -3.999e+35
   9.850e-03   2.072e-03   2.327e+35   2.105e-02  -3.032e-02
  -1.666e-02  -3.205e-03  -3.999e+35  -3.032e-02   4.460e-02
------------------------------------------------------------

======================================================================
Model TBfeo<1>(cflux<2>*diskbb<3> + bbodyrad<4>) Source No.: 1   Active/On
Model Model Component  Parameter  Unit     Value
 par  comp
   1    1   TBfeo      nH         10^22    0.117000     frozen
   2    1   TBfeo      O                   1.00000      frozen
   3    1   TBfeo      Fe                  1.00000      frozen
   4    1   TBfeo      redshift            0.0          frozen
   5    2   cflux      Emin       keV      0.500000     frozen
   6    2   cflux      Emax       keV      10.0000      frozen
   7    2   cflux      lg10Flux   cgs      -10.2767     +/-  0.340685
   8    3   diskbb     Tin        keV      0.551209     +/-  1.76186E-02
   9    3   diskbb     norm               2.96283E+19  +/-  9.17107E+36
  10    4   bbodyrad   kT         keV      1.46003      +/-  0.145093
  11    4   bbodyrad   norm               0.598719     +/-  0.211184
----------------------------------------------------------------------

Fit statistic  : Chi-Squared                 248.91     using 267 bins.
```

Figure 2.12: *The fit parameters for the spectra from SAX J1808's NICER data.*

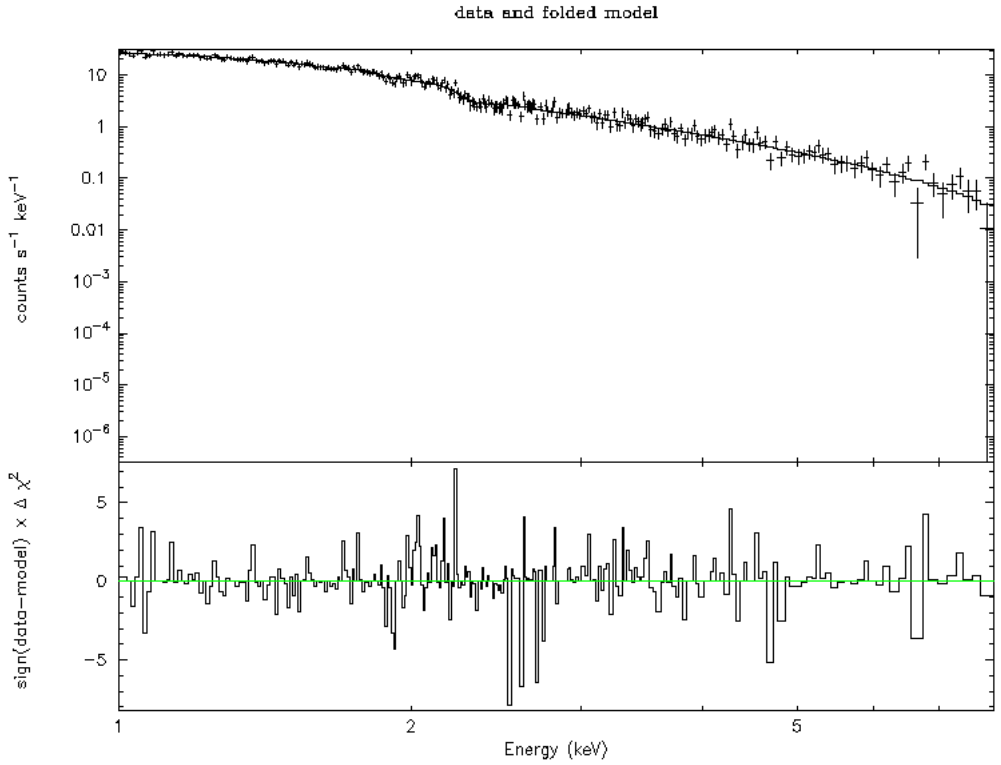

Figure 2.13: *The spectral fit of SAX J1808's NICER data using a model of (*DISK + BBODYRAD*).*

Chapter 3

SAX J1808 Publication -

The following chapter is based on a published paper summarizing the SAX J1808 results. Journal: Monthly Notices of the Royal Astronomical Society, Volume 521, Issue 2, pp.2806-2813.

The 2019 outburst of AMXP SAX J1808.4–3658 and radio follow up of MAXI J0911–655 and XTE J1701–462

K. V. S. Gasealahwe,[1,2] I. M. Monageng,[1,2] R. P. Fender,[1,3] P. A. Woudt,[1] S. E. Motta,[3,4] J. van den Eijnden,[3] D. R. A. Williams, [5] I. Heywood,[3,6,7] S. Bloemen,[8] P. J. Groot,[1,2,8] P. Vreeswijk,[8] V. McBride,[1,2,9] M. Klein-Wolt,[8] E. Körding,[8] R. Le Poole,[10] D. Pieterse[8] and S. de Wet[1]

[1]Department of Astronomy, University of Cape Town, Private Bag X3, 7701 Rondebosch, South Africa
[2]South African Astronomical Observatory, P.O. Box 9, 7935 Observatory, South Africa
[3]Department of Physics, University of Oxford, Denys Wilkinson Building, Keble Road, Oxford OX1 3RH, UK
[4]Istituto Nazionale di Astrofisica, Osservatorio Astronomico di Brera, via E. Bianchi 46, 23807 Merate (LC), Italy
[5]Jodrell Bank Centre for Astrophysics, School of Physics and Astronomy, The University of Manchester, Manchester, M13 9PL, UK
[6]Department of Physics and Electronics, Rhodes University, PO Box 94, Makhanda 6140, South Africa
[7]South African Radio Astronomy Observatory, 2 Fir Street, Black River Park, Observatory 7925, South Africa
[8]Department of Astrophysics/IMAPP, Radboud University, P.O. 9010, 6500 GL, Nijmegen, The Netherlands
[9]IAU Office of Astronomy for Development, P.O. Box 9, 7935 Observatory, South Africa
[10]Leiden Observatory, Leiden University, P.O. Box 9513, NL-2300 RA Leiden, The Netherlands

Abstract

We present radio coverage of the 2019 outburst of the accreting millisecond X-ray pulsar SAX J1808.4–3658, obtained with MeerKAT. We compare these data to contemporaneous X-ray and optical measurements in order to investigate the coupling between accretion and jet formation in this system, while the optical lightcurve provides greater detail of the outburst. The reflaring activity following the main outburst peak was associated with a radio re-brightening, indicating a strengthening of the jet in this phase of the outburst. We place quasi-simultaneous radio and X-ray measurements on the global radio:X-ray plane for X-ray binaries, and show they reside in the same region of luminosity space as previous outburst measurements, but significantly refine the correlation for this source. We also present upper limits on the radio emission from the accreting millisecond X-ray pulsar MAXI J0911–655 and the transitional Z/Atoll-type transient XTE J1701–462. In the latter source we also confirm that nearby large-scale structures reported in previous radio observations of the source are persistent over a period of ~ 15 years, and so are almost certainly background radio galaxies and not associated with the X-ray transient.

Keywords

radio continuum: transients – X-rays: binaries – stars:neutron

3.1 Introduction

Neutron Star (NS) X-ray binaries (XRBs) are binary systems comprising a NS that accretes matter from a companion star. A subgroup of these are systems with low-mass ($M_{companion} < 1\ M_{\odot}$) companions, and are thought to be considerably older than systems with a higher mass ($M_{companion} \gtrsim 8\ M_{\odot}$; Joss et al. 1978). In a subset of the low-mass systems, the NS is observed to spin at periods significantly smaller than a second, either through the detection of pulsations in their X-ray flux or oscillations during thermonuclear Type I X-ray bursts on their surface (Patruno and Watts 2021). In accreting millisecond X-ray pulsars (AMXPs), of which SAX J1808.4–3658 (Wijnands and van der Klis 1998a) is the prototype, the accretion and millisecond combination may be explained by the scenario of recycled pulsars. In this scenario the pulsar originates as a 'normal' pulsar that eventually spins down on a timescale of $t \approx 10^6$ yrs, possibly in combination with magnetic field decay. The pulsar is spun up again through an accretion phase and manifests as an AMXP (Alpar et al. 1982, Backer et al. 1982, Srinivasan 2010) which emits pulsed X-rays with a period of 1-10 ms. Some pulsars are estimated to have a relatively low magnetic field strength of $\sim 10^8$ G. Two other empirical classifications of NS-XRBs at high accretion rate and low magnetic field ($\leq 10^9$ G) systems are known: the Atoll and Z sources. The former may also exhibit pulsations. These two classes are distinctly classified according to the ratio of their X-ray soft and hard energy bands often referred to as X-ray colours, traced over different time-scales (Hasinger and van der Klis 1989). For the Z sources, the hard and soft colours plotted against each other reveal a 'Z-shape' pattern traversed on time-scales of hours to days, while Atoll sources show a 'C-shape' pattern generally accompanied by an 'island' at large hard colours on time-scales ranging from weeks to months (Muno et al. 2002). Some sources display a blend of properties of the two classes as well as properties that enter in neither (e.g. Cir X-1; Moin et al. 2011). Most dramatically the neutron star transient XTE J1701–462 demonstrated a clear transition from Z-like to Atoll-like properties as its luminosity dropped resulting from a high mass transfer rate ($\dot{m}$) to a lower $\dot{m}$ during the outburst decay. This allowed to connect the two classes to accretion rate (Homan et al. 2007a). This blurring of some Atoll and Z sources coupled with properties of AMXPs makes the distinction of the different classes of NS-XRBs poorly understood.

Interesting in their own right, accreting low-magnetic field neutron stars in the Z/Atoll/AMXP classes play a crucial role as a control sample to the Black Hole (BH) population in the context of the coupling between accretion and jet formation in BHs, which have no surface. While detailed studies of individual sources are important, a key global diagnostic of this jet:outflow (where the radio is from the jets and X-rays are observed from accretion flow) coupling is the use of the radio:X-ray luminosity plane (Gallo et al. 2003). One key result from such global studies is that the sample of black holes are typically more radio-loud (exhibiting brighter radio luminosities) than the populations of neutron stars for a given X-ray luminosity (Fender and Kuulkers 2001, Migliari and Fender 2006). Another key result is the slope of the radio:X-ray correlation. In BH systems in the hard X-ray state (or: at relatively low luminosities) accretion is believed to be inefficient, as a large fraction of the gravitational potential energy is not radiated, but lost across the BH event horizon (Fender and Belloni 2012). In contrast, in NS systems accretion may be efficient as all the potential energy of the accreting matter is released at the NS surface. This may result in a steeper correlation (see e.g. discussion in Coriat et al. 2011). Multiple studies of NS systems, however, suggest that the slope of the correlation for some NS-XRBs is inconsistent with this assumption (Deller et al. 2015, Gallo et al. 2018, Migliari and Fender 2006, Tudose et al. 2009). The correlation slope of some NSs being similar to that of BHs is surprising because the physical properties are different between the compact objects. In order to develop a better understanding of the radio:X-ray correlation for NS-XRBs, a quantitative analysis of luminosity strength is required of these systems. In this study we do not consider high-magnetic field accreting neutron stars, which are less radio luminous and may well have a quite different flow geometry close to the NS, but we direct the interested reader to van den Eijnden et al. (2021) for details.

SAX J1808.4–3658 (SAX J1808 hereafter), is an X-ray binary with an X-ray pulsation at 401 Hz. SAX J1808 was discovered in 1998 by the *Rossi X-ray Timing Explorer (RXTE)* (Levine et al. 1996), and was the first confirmed AMXP (Wijnands and van der Klis 1998a). SAX J1808 displays Type I thermonuclear X-ray bursts based on which a distance of 3.5 kpc was estimated (Galloway and Cumming 2006, in 't Zand et al. 1998). An orbital period of $\approx$ 2 hr (Chakrabarty and Morgan 1998) is known for the source. SAX J1808 is reported to go into semi-regular outbursts with recurrence times between 2 and 4 years. Previous outbursts from SAX J1808 were recorded in 1999, 2002, 2005, 2015 (Tudor et al. 2017), 2019 (Ambrosino et al. 2021, Baglio et al. 2020, Bult et al. 2020, Goodwin et al. 2020) and 2022 (Illiano et al. 2023). We report on the 2019 outburst of SAX J1808 as observed with MeerKAT (in radio Williams et al. 2019). SAX J1808 was observed with the X-ray telescope (XRT) onboard the Neil Gehrels Swift telescope (*Swift*; Burrows et al. 2005) and the *Neutron Star Interior Composition ExploreR* (*NICER*; Gendreau et al. 2012b) in the X-rays and additionally show the optical Las Cumbres Observatory LCO data reported in Baglio et al. (2020) to trace the main outburst via a multi-wavelength approach, and to measure the radio:X-ray correlation for this outburst of the source.

Additionally, while we compare SAX J1808 to the rest of the AMXP radio and X-ray luminosity measurements ($L_R L_X$), we also report short MeerKAT observations of the AMXP MAXI J0911–655 (MAXI J0911 hereafter, Homan et al. 2016, Serino et al. 2016) and transitional Atoll/Z-source XTE J1701–462 (XTE J1701 hereafter, Homan et al. 2007a).

3.2 Observations

3.2.1 MeerKAT observations

The 2019 outburst of SAX J1808 was monitored with MeerKAT at 1.28 GHz, through the ThunderKAT Large Survey Programme (Fender et al. 2016) and by *Swift* as part of an associate observing program. MeerKAT consists of 64 dishes and on average 61 dishes were available per observation. The outburst was monitored nearly weekly for 6 epochs (Table 3.1) from 2019 July 31 to August 31, for 15 mins every week. J1939–6342 was observed for 5 mins at the start of each observation, as the primary calibrator for flux and bandpass calibrations. The secondary calibrator, J1830–3602, was observed for 2 mins before and after the target in each observation. All observations were performed with a total bandwidth of 860 MHz, divided into 4096 channels of width 209 kHz. The MeerKAT data were reduced using the semi-automated pipeline, OXKAT[1] (Heywood 2020). The first generation process of OXKAT involves making use of CASA (McMullin et al. 2007) to perform averaging, flagging and do cross- and self-calibration. Once the visibility and gain solution plots produced were satisfactory after inspection, the data were then flagged and imaged using the TRICOLOUR and WSCLEAN packages respectively (Offringa et al. 2014). Thereafter, the second generation processing was initiated to do self calibration, plot gain solutions and a second output of images were produced. The flux densities were then determined using PYBDSF (Mohan and Rafferty 2015).

MAXI J0911 and XTE J1701 were observed with MeerKAT in the same way as SAX J1808. MAXI J0911 was observed around a phase of hard X-ray emission (Ng et al. 2021) on the 8 and 26 July 2021 while XTE J1701 was observed on the 26 July 2021 as part of a broader study of NS-XRBs with ThunderKAT. The sources were observed for 15 min for each observation and the reduction and analysis procedures are the same as those described above for SAX J1808, except the primary and secondary calibrator for MAXI J0911 were J0408-6545 and J0906-6829 respectively, and the secondary calibrator for XTE J1701 was J1744-5144.

3.2.2 X-ray observations

Swift/XRT provided a total of 21 observations of SAX J1808 of variable duration, of which 10 were between 31 July to 31 August 2019, taken quasi-simultaneously with MeerKAT. The overall *Swift*/XRT exposure time was formed by a number of snapshots, taken in both Windowed Timing (WT) mode and Photon Counting (PC) mode (Burrows et al. 2005), both providing data in the 0.3–10.0 keV energy band. Following the XRT reduction threads [2] we extracted spectra from circular regions centred at the source position, with a radius of 30 pixels. When fitting the energy spectra we ignored data below 0.6 keV since spectra can be dominated by strong redistribution effects associated with the WT readout process, as well as trailing charge released from deep charge traps in the CCD on time-scales comparable to the WT readout time. The above might result in additional low energy events that may distort the spectrum. Spectra were then extracted following standard extraction procedures [3].

Based on the radio observations taken of MAXI J0911 and XTE J1701, we followed up to check if any observations were taken with *Swift* at the time. *Swift*/BAT survey data was found of both sources, which were within a day of quasi-simultaneity of the first epoch of MAXI J0911 radio observations and the single epoch of

[1] for more details see, `https://github.com/IanHeywood/oxkat`
[2] `http://www.swift.ac.uk/analysis/xrt/#abs`
[3] See, e.g., `https://www.swift.ac.uk/analysis/xrt/spectra.php`

XTE J1701.

The *NICER* telescope observed the 2019 outburst of SAX J1808 extensively in X-rays, providing near-daily coverage of the outburst between 30 July and 28 September 2019 (Bult et al. 2019). In order to probe the overall evolution of the outburst, we analysed the cumulative data taken on each day, often combining a number of shorter exposures per MJD. We applied the FTOOL NICERL2 to perform the most recent calibration, after which we extracted the source count rate between 0.5 and 10 keV. To calculate the background count rate, we applied the *nicer_bkg_estimator* model, based on *RXTE* blank sky background fields (Jahoda et al. 2006), in the same energy band. During days where the source count rates does not exceed three times the background, we report 3σ upper limits. For the remaining observations, we show the light curve in the top panel of Figure 3.1. Due to the small background rate compared to the source count rate during the majority of the outburst, for simplicity we plot the source count rates not background-corrected. Both the *Swift*/XRT and *NICER* spectra were fitted with a model in the form (tbfeo $*$ [continuum]), where tbfeo is an ISM model and *[continuum]* was either a powerlaw (POWER in XPEC), a disk-blackbody component (DISKBB), or a combination of disk-blackbody and a blackbody component (DISKBB + BBODYRAD). In modelling the interstellar absorption, we assumed abundances from Wilms et al. (2000) and cross-sections from Verner et al. (1996). The *Swift*/XRT and *NICER* spectra were fitted in the 0.6–10keV and 0.2–10keV energy range, respectively. In both cases, we fixed the equivalent Hydrogen column density to $n_H = 0.117 \times 10^{22} cm^{-2}$ [1].

3.3 Results

3.3.1 SAX J1808

In the X-rays, our *NICER* results reveals the outburst of SAX J1808 to have a main outburst and subsequent reflaring (top panel of Figure 3.1) within the 1 – 10.0 keV energy band. The main outburst rises around 6 August 2019 (MJD = 58701) and the reflaring around 27 August 2019 (MJD = 58722). The 5 detections we record here from *Swift* only display the decline of the main outburst with a peak flux at $(7.27\pm0.16) \times 10^{-10}$ erg/s/cm^2 on the 12 August 2019 (MJD = 58708.47, second panel of Figure 3.1). While our *NICER* results reveal a peak flux $(6.20\pm0.018)\times10^{-10}$ erg/s/cm^2 (247 counts/s, MJD = 58705.01 in the first panel of Figure 3.1), similarly Bult et al. (2019) record a peak bolometric flux of $(4.7\pm0.5)\times10^{-10}$ erg/s/cm^2 within the 0.01 – 100 keV energy band. SAX J1808 was undetected in the first two epochs of the MeerKAT monitoring. These non-detections have upper limits of 0.075 mJy/beam and 0.12 mJy/beam at 3σ, respectively (indicated with upside-down triangles in the third panel of Figure 3.1). The lightcurve was constructed using the flux measurements from PYBDSF such that the radio flare is seen to peak at 0.59 ± 0.034 mJy/beam. We observe a decline in the radio lightcurve between 10 – 23 August (MJD = 58705 – 58718) but the rise of a reflare event is seen between the 5$^{\text{th}}$ and 6$^{\text{th}}$ epoch (23 – 31 August, MJD = 58718 – 58726) as an increase from 0.11 – 0.16 mJy/beam is measured. In addition to the LCO optical data, the source was observed with MeerLICHT, a prototype of the BlackGEM array (Bloemen et al. 2016, Groot 2019) which provides simultaneous monitoring of the same area of the sky as MeerKAT. The data were processed automatically with the BLACKBOX/ZOGY pipeline (Vreeswijk and Paterson 2021), which performs primary reductions that include bias subtraction, overscan corrections and flat-fielding, as well as astrometric and photometric calibrations. Daily averages of each band were determined by co-adding the images and ranged between 17.89 ± 0.04 – 19.38 ± 0.06 magnitudes across all bands. The results

[1] See `https://heasarc.gsfc.nasa.gov/cgi-bin/Tools/w3nh/w3nh.pl`

Table 3.1: *The MeerKAT radio flux densities (1.28 GHz) and luminosities at 5GHz, along with Swift and NICER X-ray flux and luminosities matches from the 1-10 keV energy band. The upper limits are 3σ and the uncertainties in the table are 1σ. The luminosities are based on distance estimates of 3.5 kpc, 10.4 kpc and 10 kpc for SAX J1808, MAXI J0911 and XTE J1701, respectively. The Swift and NICER radio:X-ray matches are indicated as $S^{1,2,3}$ and $N_{1,2,3,4,5,6}$ respectively, next to the MJDs.*

MJD	F_r [mJy/beam]	$F_{xNICER} \times 10^{-10}$ [erg/s/cm^2]	$F_{xSwift} \times 10^{-10}$ [erg/s/cm^2]	$L_r \times 10^{28}$ [erg/s]	$L_{xNICER} \times 10^{36}$ [erg/s]	$L_{xSwift} \times 10^{36}$ [erg/s]
SAX J1808						
58695.02_{N1}		0.0040 ± 0.0002			0.00059 ± 0.00003	
58695.74_{N1}	<0.075			<0.56		
58699.27_{N2}		0.0060 ± 0.0002			0.00088 ± 0.00003	
58699.82_{N2}	<0.12			<0.86		
58705.01_{N3}		6.20 ± 0.02			0.910 ± 0.003	
58705.81^{S1}_{N3}	0.59 ± 0.04			4.32 ± 0.25		
58708.47^{S1}			7.27 ± 0.16			$1.065^{+0.023}_{-0.024}$
58710.40			6.33 ± 0.16			0.930 ± 0.023
58711.05_{N4}		4.70 ± 0.01			0.700 ± 0.002	
58711.95^{S2}_{N4}	0.36 ± 0.02			2.67 ± 0.15		
58712.65^{S2}			3.98 ± 0.14			0.58 ± 0.02
58718.70_{N5}	0.11 ± 0.02			0.83 ± 0.15		
58719.00_{N5}		0.920±0.005			0.1300±0.0007	
58726.79^{S3}_{N6}	0.16 ± 0.02			1.20 ± 0.13		
58726.98_{N6}		0.80 ± 0.02			0.20± 0.02	
58728.45^{S3}			$1.390^{+0.063}_{-0.066}$			$0.2030^{+0.0092}_{-0.0096}$
58740.81			$0.937^{+0.078}_{-0.065}$			$0.137^{+0.012}_{-0.010}$
58741.79						
MAXI J0911						
59403.25	<0.055		<2.32	<3.57		<3
XTE J1701						
59421.75	<0.072		<2094	<4.29		<2500

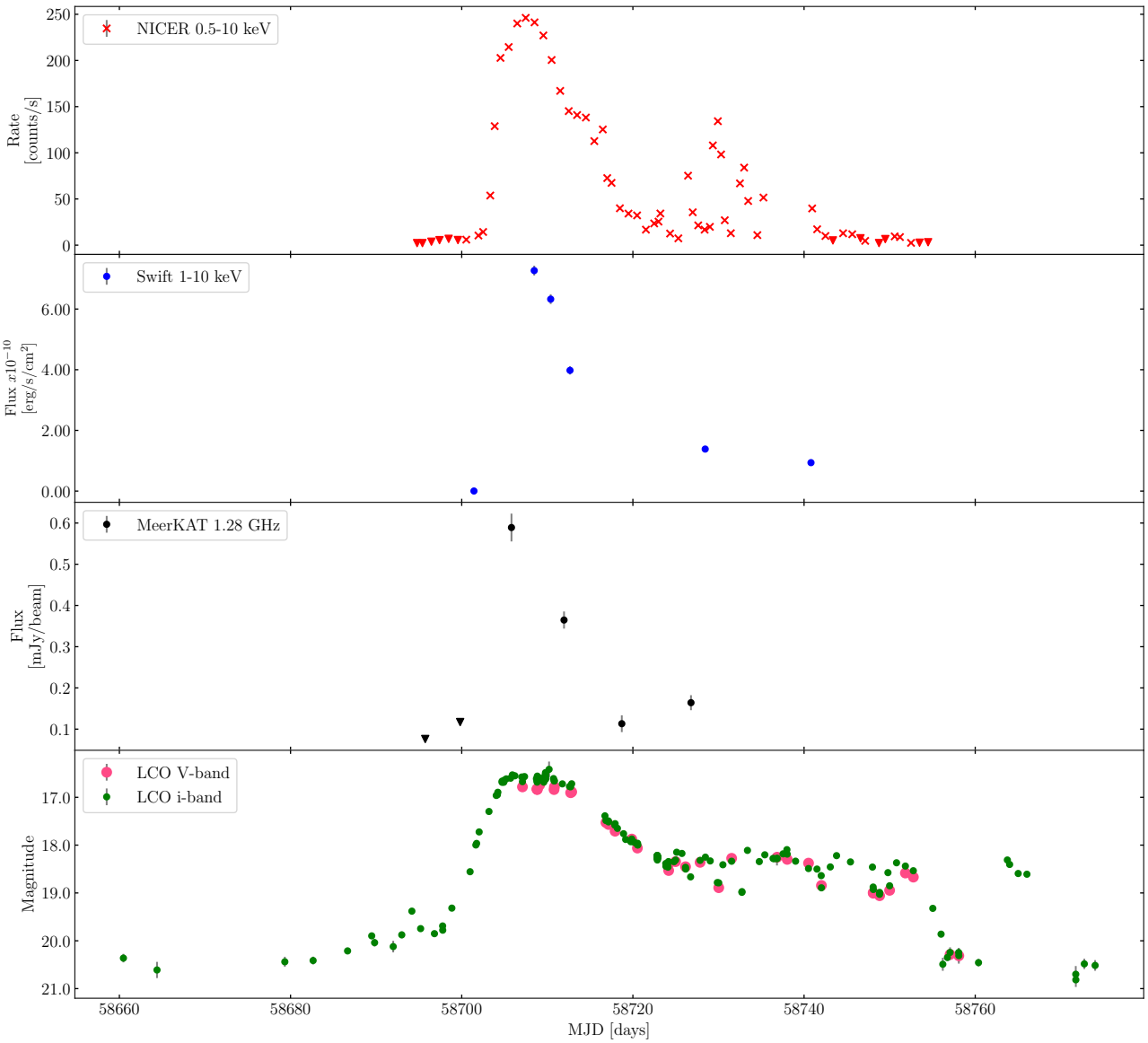

Figure 3.1: *The 2019 outburst of SAX J1808 as seen in the X-ray (top panel: 0.5–10 keV, second panel: 1–10 keV), radio (third panel: 1.28 GHz) and optical (bottom panel: V and i band). The upper limits from NICER and the non-detections of the first two epochs in the radio are indicated with the red and black upside down triangles, respectively.*

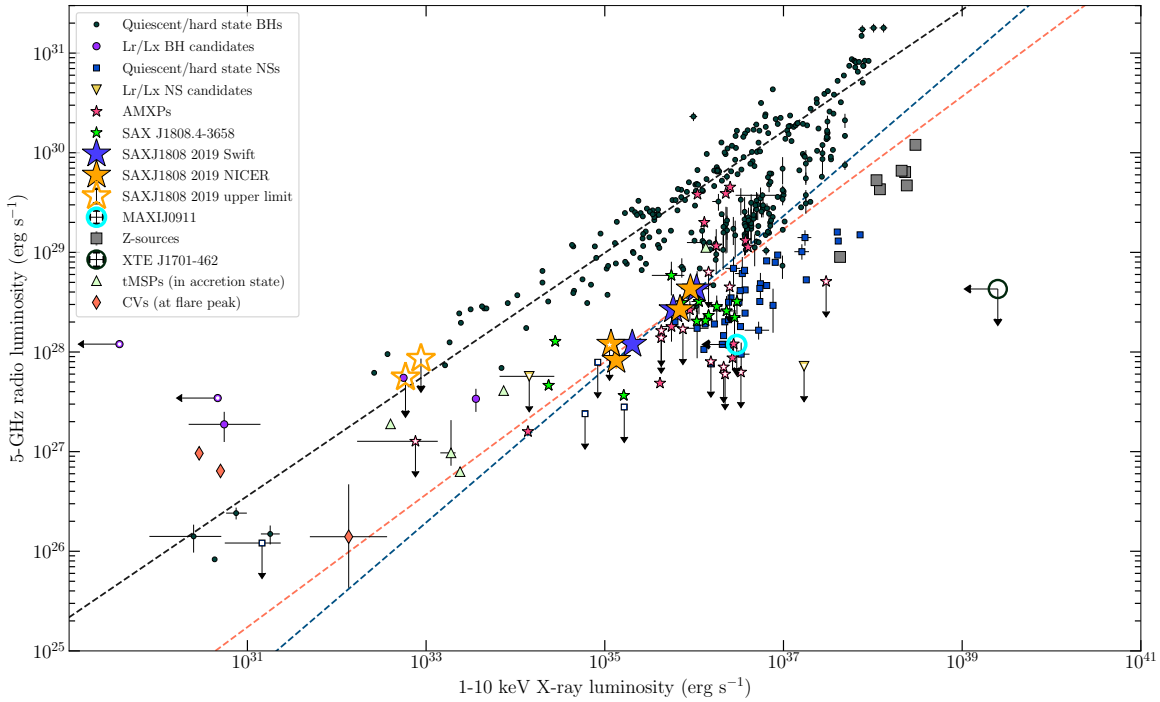

Figure 3.2: *The radio:X-ray correlation for BH and NS sources labeled in terms of class (Bahramian et al. 2018, Migliari and Fender 2006), with previous SAX J1808 detections indicated with green stars and the results from this work with the blue and orange stars, with the dashed blue line indicating the slope of the Swift matches and the orange dashed line the slope of the NICER detection matches. The NICER upper limit matches are the open orange stars. The BH population slope is indicated with the black dashed line and the upper limits from the MAXI J0911 and XTE J1701 observations are indicated with the cyan and black open circles respectively*

from MeerLICHT, which we do not plot, confirm the results from the more comprehensive data from LCO displayed in the bottom panel of Figure 3.1.

3.3.2 MAXI J0911 and XTE J1701

In the radio, neither MAXI J0911 nor XTE J1701 were detected. The 3σ upper limits presented in Table 3.1 represent that of the single radio:X-ray matches for each source. Assuming a flat spectral index the radio flux was converted to a frequency of 5 GHz such that the luminosity νL_ν is $5L_5$ (referred to as radio luminosity L_R in the paper). The luminosity upper limits are $L_R < 3.57 \times 10^{28}$ erg/s and $L_R < 4.29 \times 10^{28}$ erg/s taken on MJD 59421.65 and 59421.76 respectively (26 July 2021) for MAXI J0911 and XTE J1701 respectively. These luminosities were determined using distances 10.4 kpc (Tudor et al. 2016) and 10 kpc (Fender et al. 2007) for MAXI J0911 and XTE J1701 respectively and the upper limits are plotted in cyan (MAXI J0911) and black open circles (XTE J1701) in Figure 3.2.

Table 3.2: *The peak flux density of the extended sources B C D of XTE J1701 as indicated in Figure 5 of Fender et al. (2007), along with the spectral index between the MeerKAT (1.28 GHz) 2021 observation and the ATCA (4.8, 8.6 GHz) 2006 observations in Fender et al. (2007).*

Source	$F_{1.28}$ $[\frac{\text{mJy}}{\text{beam}}]$	$F_{4.8}$ $[\frac{\text{mJy}}{\text{beam}}]$	$F_{8.6}$ $[\frac{\text{mJy}}{\text{beam}}]$	α (4.8-8.6)	α (1.28-4.8-8.6)
B	22.23	2.5	0.9	-1.7	-1.7
C	16.38	2.0	0.5	-2.4	-1.7
D	16.55	1.5	0.3	-2.7	-1.9

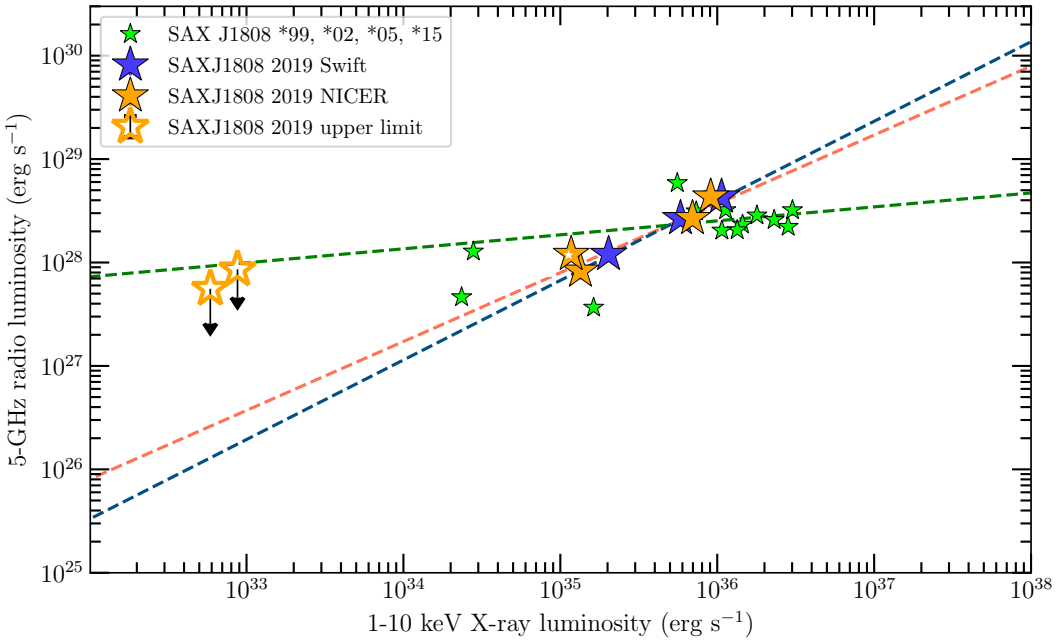

Figure 3.3: *The radio:X-ray correlation slopes for the SAX J1808 outbursts; 2019 outburst (blue and orange), a group of four of the older outbursts reported (green). The combination of all older outburst points on the figure (1999, 2002, 2005, 2015) are fit to a slope of* β=0.33 ± 0.23 *and indicated with the green dashed line. The blue and orange dashed lines represent the detection matches (excluding upper limits) with slopes* β=0.77 ± 0.13 *and* β=0.67 ± 0.33 *for the Swift and NICER 2019 outburst, respectively. The NICER radio upper limit matches are presented as open orange stars.*

3.4 Discussion

In this section we discuss the 2019 outburst of SAX J1808 and the placement of the sources (in this work) on the radio:X-ray correlation. We only provide single upper limits of MAXI J0911 and XTE J1701, but the 2019 outburst results significantly extend SAX J1808's X-ray luminosity range on the plane.

3.4.1 SAX J1808 2019 Outburst

Our results show that the X-ray peak follows the radio peak where maximum flux density is recorded as 0.59 ± 0.034 mJy/beam, indicating jet action from 10 August 2019 (MJD 58705). The optical reports of the 2019 outburst recorded (see Baglio et al. 2020, Goodwin et al. 2020) observations from Las Cumbres Observatory (LCO) and the Southern African Large Telescope (SALT). Goodwin et al. (2020) caught the rise of the outburst with a peak optical flux > 1.2 mJy around the 10 August and we present the Baglio et al. (2020) lightcurve in bottom panel of Figure 3.1 where we note two rise and dips occurrences (around 22 July – 3 August 2019 corresponding to MJDs 58686 – 58698) before the peak of the main outburst is seen around 11 August 2019 (MJD 58706). The reflaring event started around the 24 August 2019 and while we only see the start of this reflare in our radio results (third panel Figure 3.1), it shows the jets are still present as suggested in Baglio et al. (2020). In Goodwin et al. (2020) the X-ray peak was detected on the 14 August 2019 (MJD 58709). These reports together with our results suggest the optical peaked first and the X-ray and radio outbursts peaked later. This result may be explained by an outside-in outburst (see Ioannou et al. 1999) starting from the outer edges of the disk. The early optical activity in the 2019 outburst is discussed in more detail in Goodwin et al. (2020), proposing scenarios that stem from mass transfer variations and geometrical effects of the disk. The cadence of our radio observations was not high enough to quantify the outside-in outburst mechanism.

3.4.2 The radio:X-ray correlation of SAX J1808

Figure 3.1 illustrates the evolution of the radio (MeerKAT) and X-ray (*NICER*, *Swift*) outburst in the first three panels. A flat spectral index is assumed and the radio luminosity is determined similarly to MAXI J0911 and XTE J1701 mentioned in Section 3.2; in the case of SAX J1808 the luminosities are based on a distance of 3.5 kpc (Galloway and Cumming 2006). Based on the 10 quasi-simultaneous *Swift* observations, the source was only detected in 6 epochs. After inspection, 3 epochs were selected which were within Δt $\sim$ 2 days of 3 of the radio observations (see matches $S^{1,2,3}$ in Table 3.1). The radio and X-ray luminosities from the selected MJDs, were used to determine SAX J1808's position on the radio:X-ray correlation plot. Since the *NICER* observations are taken at higher cadence, we were able to match the 6 radio observations within Δt $\sim$ 1 day (see matches $N_{1,2,3,4,5,6}$ in Table 3.1). The radio:X-ray correlation is shown in Figure 3.2 where the blue stars indicate the 2019 outburst results based on the *Swift* matches and the orange stars are the *NICER* matches for the 6 radio observations. The previous $L_R L_X$ measurements of the source are shown with the green stars. In this figure SAX J1808 lies among the AMXP class of sources which are indicated with the pink stars. This is an expected result for the source since it is the cornerstone of the AMXP class, and we note that these results have less scatter than the previous outbursts. The upper limits of the *NICER* matches extend to lower radio and X-ray luminosities, revealing how extensive the luminosity range of the source can get on the correlation plane. The PYTHON module, LINEAR REGRESSION, in the SKLEARN library was used to determine a best fit of the SAX J1808 2019 outburst, the data points were fed into the model and as a result produced slopes β=0.77 ± 0.13 and β=0.67 ± 0.33 for the detection matches (excluding upper limits) of *Swift* and *NICER*, respectively. We also fit

all the *NICER* matches (including the upper limits) and the best fit slope was β=0.35±0.38. The older outbursts results produced a fit of (β=0.33 ± 0.23), the combination of complete SAX J1808 points (β=0.34 ± 0.20) and the complete AMXP class (β=0.38 ± 0.23) only included the set of *Swift* matches (Figure 3.3). These less steep slopes are suspected to be due to the increase in scatter of the overall sample of points of the source. The slope which includes the low luminosity upper limits from *NICER* is small too but with larger error, in contrast a recent report on intermittent AMXP Aql X-1 at low X-ray luminosities finds a slope of β=$1.17^{+0.30}_{-0.21}$ where detection and upper limits of multiple outbursts are included for the fit (see more details in Gusinskaia et al. 2020). Gusinskaia et al. (2020) also fit detections only, these slopes (based on different hardness ratios) ranged between $\beta \sim 0.73 - 0.96$. This indicates that a single NS-XRB can have a varying slope depending on the outburst and the detections included in the fit. Furthermore, the radio:X-ray correlation for BHXBs and NS-XRBs from Coriat et al. (2011) reports the radiatively inefficient and efficient branches have slopes $\beta \sim 0.7$ and $\beta \sim 1.4$ for the BHXBs and NS-XRBs respectively. Similarly seen in Migliari et al. (2003), while some NS-XRB systems follow this trend, the slopes of SAX J1808 in this work match more closely to that of the BHXBs. This is a result that has been observed before for NS-XRBs. Tudor et al. (2017) demonstrated that the slope of AMXP IGR J00291+5934 is 0.77 ± 0.18, hence it does appear the correlation slopes of some NSs behave differently.

3.4.3 MAXI J0911-655

MAXI J0911, which resides in the globular cluster NGC 2808, was first detected with MAXI/GSC's nova alert system in February 2016 (Mihara et al. 2011, Serino et al. 2016). The X-ray activity from the source was detected about a week later with *Swift*/BAT (Sanna et al. 2017b). Later detections of X-ray activity prompted simultaneous radio follow-up with ATCA (Tudor et al. 2016), yielding an upper limit $L_R < 4.5 \times 10^{28}$ erg/s at 5 GHz. Assuming a flat spectrum and distance 10.4 kpc, we derive a 3σ upper limit $L_R < 3.57 \times 10^{28}$ erg/s based on MeerKAT observations taken in July 2021 (see cyan open circle in Figure 3.2) after weak hard X-rays were detected in Ng et al. (2021).

3.4.4 XTE J1701

XTE J1701 is an important source in the study of NS-XRBs as it exhibited behaviour associated with both 'Z' and 'Atoll'-type binaries, establishing that these classifications depend upon accretion state (Lin et al. 2009b). Fender et al. (2007) reported a small number of radio detections of XTE J1701, which were broadly consistent with those reported for other Z-sources. They also reported an extended structure (labelled sources B C and D in Figure 5 of Fender et al. (2007)) approximately three arcmin to the south which they speculated could be a large-scale jet associated with the outburst of the binary. This structure is visible in our MeerKAT image at flux densities consistent with being constant over $\sim$ 15 years (see luminosity upper limits at 10 kpc (Fender et al. 2007) in Table 3.1 and spectral indexes Table 3.2, while the source is placed as the black open circle on the radio:X-ray plane in Figure 3.2). We therefore rule out any association with a transient jet associated with the binary, and attribute these sources to background extragalactic sources instead. The limit on the core radio luminosity from XTE J1701 is not particularly constraining given the quiescent state during the July 2021 observation.

3.5 Conclusion

NS-XRBs are an interesting class to study the disk/jet coupling since the radio:X-ray correlation tends to vary considerably in different sources and accretion regimes. We report here on the 2019 outburst of SAX J1808 as well as follow up observations of MAXI J0911 and XTE J1701 carried out as part of the ThunderKAT Large Survey Programme on MeerKAT (Fender et al. 2016). SAX J1808 is reported in the radio, X-ray and the optical from MeerKAT, *Swift*, *NICER* and LCO respectively. The outburst lasted from July to early October 2019, including a main outburst event and a reflare event which started late August to early September 2019. These results suggest the peak of the main outburst is seen in the optical before the X-ray and radio which may imply an outside-in outburst (Ioannou et al. 1999), however, our radio observations were not sampled at a high enough cadence to suggest the mechanism occurred in this system. Furthermore, the reflaring event was associated with a radio re-brightening, indicating a strengthening of the jet in this phase (Baglio et al. 2020). The radio:X-ray correlation of the source in this work (*Swift* and *NICER* detection matches have a slope of $\beta \sim 0.77 \pm 0.13$ and $\beta \sim 0.67 \pm 0.33$ respectively) suggests a similar radiative efficiency compared to the BHXB standard slope of $\beta \sim 0.6$ (Carotenuto et al. 2021, Corbel et al. 2000, 2003, 2013). Finally, the upper limits of MAXI J0911 and XTE J1701 from both MeerKAT and *Swift* place the sources in their respective classes (AMXP the former, Z/Atoll the latter). And while these are non-detections the results encourage continued monitoring of these sources and similar NS-XRBs to improve our understanding and reveal the true nature of the disk and jet coupling in XRBs.

Acknowledgements

KVSG, IMM, PAW and PJG acknowledge support from the University of Cape Town and the National Research Foundation. KVSG would like to thank Dave Russell for making the LCO data published in Baglio et al. (2020) available for the improvement of this paper. KVSG acknowledges Lauren Rhodes for the advice during radio data processing. PJG is supported by NRF SARChI grant 111692. SEM acknowledges financial contribution from the agreement ASI-INAF n.2017-14-H.0, and PRIN-INAF 2019 n.15. DRAW was supported by the Oxford Centre for Astrophysical Surveys, which is funded through generous support from the Hintze Family Charitable Foundation. JvdE is supported by a Lee Hysan Junior Research Fellowship awarded by St. Hilda's College, Oxford. IH acknowledges support from the UK Science and Technology Facilities Council [ST/N000919/1], and from the South African Radio Astronomy Observatory. VAM acknowledges support from the National Research Foundation grant 119466.

The MeerKAT telescope is operated by the South African Radio Astronomy Observatory, which is a facility of the National Research Foundation, an agency of the Department of Science and Innovation. We acknowledge the use of public data from the *Swift*/BAT/XRT data archive. We acknowledge the use of the ilifu cloud computing facility – www.ilifu.ac.za, a partnership between the University of Cape Town, the University of the Western Cape, the University of Stellenbosch, Sol Plaatje University, the Cape Peninsula University of Technology and the South African Radio Astronomy Observatory. The Ilifu facility is supported by contributions from the Inter-University Institute for Data Intensive Astronomy (IDIA – a partnership between the University of Cape Town, the University of Pretoria, the University of the Western Cape and the South African Radio astronomy Observatory), the Computational Biology division at UCT and the Data Intensive Research Initiative of South Africa (DIRISA).

Data Availability

The data underlying this article will be shared on reasonable request to the corresponding author.

Chapter 4

XTE J1701 Publication -

This chapter is based on the work depicted in the XTE J1701 publication. Journal: Monthly Notices of the Royal Astronomical Society, Volume 533, Issue 2, pp.1800-1807.

Radio observations of the 2022 outburst of the transitional Z-Atoll source XTE J1701-462

K. V. S. Gasealahwe,[1,2] I. M. Monageng,[1,2] R. P. Fender,[1,3] P. A. Woudt,[1] A. K. Hughes,[4] S. E. Motta,[3,5] J. van den Eijnden,[6] P. Saikia,[7] E. Tremou,[8]

[1]Department of Astronomy, University of Cape Town, Private Bag X3, 7701 Rondebosch, South Africa
[2]South African Astronomical Observatory, P.O. Box 9, 7935 Observatory, South Africa
[3]Department of Physics, University of Oxford, Denys Wilkinson Building, Keble Road, Oxford OX1 3RH, UK
[4]Department of Physics, University of Alberta, CCIS 4-181, Edmonton, AB T6G 2E1, Canada
[5]Istituto Nazionale di Astrofisica, Osservatorio Astronomico di Brera, via E. Bianchi 46, 23807 Merate (LC), Italy
[6]Department of Physics, University of Warwick, Coventry CV4 7AL, UK
[7]Center for Astrophysics and Space Science (CASS), New York University Abu Dhabi, PO Box 129188, Abu Dhabi, UAE
[8]National Radio Astronomy Observatory, Socorro, NM 87801, USA

Abstract

XTE J1701-462 is a neutron star low mass X-ray binary (NS LMXB) discovered in 2006 as the first system to demonstrate unambiguously that the 'Atoll' and 'Z' classes of accreting neutron stars are separated by accretion rate. Radio observations during the 2006/7 outburst provided evidence for the formation of a relativistic jet, as now expected for all accreting neutron star and black hole X-ray binaries at high accretion rates. The source entered a new outburst in 2022, and we report 29 observations made with the MeerKAT radio telescope. The first radio detection was on the 16th September 2022, we continued detecting the source until mid-December 2022. Thereafter, establishing radio upper limits till 25 March 2023. We present the radio analysis alongside analysis of contemporaneous X-ray observations from MAXI. The radio light curve shows evidence for at least three flare-like events over the first hundred days, the most luminous of which has an associated minimum energy of 1×10^{38} erg. We provide a detailed comparison with the 2006/7 outburst, and demonstrate that we detected radio emission from the source for considerably longer in the more recent outburst, although this is probably a function of sampling. We further constrain the radio emission from the source to have a polarisation of less than 9% at the time of 2022 IXPE detection of X-ray polarisation. Finally, we place the source in the radio – X-ray plane, demonstrating that when detected in radio it sits in a comparable region of parameter space to the other Z-sources.

Keywords

radio continuum: transients – X-rays: binaries – stars: neutron

4.1 Introduction

Low-mass X-ray binaries (LMXBs) consist of a compact object that could be a black hole (BH) or a neutron star (NS) and low-mass star as a binary companion. In these systems the compact object may accrete matter from the companion via an accretion disc showing X-ray outbursts as a result of the mass transfer between the objects. During such outbursts the sources can be detected in the radio due to the synchrotron emission from outflowing jets. The collimated compact jets follow a non-linear radio – X-ray luminosity correlation, where $L_{\rm R} \propto L_{\rm X}^{\beta}$ with $\beta \approx 0.5 - 0.7$ (Corbel et al. 2003, 2013, Gallo et al. 2018), which extends to supermassive BHs through the fundamental plane of BH activity (Falcke et al. 2004, Merloni et al. 2003, Saikia et al. 2015, 2018), suggesting scale invariance of compact jets. The radio – X-ray correlation for BH and NSs is expected to differ considerably due to the physical nature of the compact objects. This is largely due to radiative inefficient accretion assumed for BHs due to gravitational potential being lost across the event horizon. Since matter accretes onto the NS surface it is expected to be more radiatively efficient such that the radio – X-ray correlation is steeper. Studies over the past two decades suggest however, that the efficiency is similar between the two classes of objects with sources following parallel tracks on the correlation plane (Deller et al. 2015, Gallo et al. 2018, Migliari and Fender 2006, Tudose et al. 2009).

Z- and Atoll sources are low magnetic field NS LMXBs (Hasinger and van der Klis 1989, Muno et al. 2002). The systems are classified as Z- or Atoll based on the patterns traced out by their X-ray colour-colour diagrams (CCDs) or their hardness intensity diagrams (HID) (see examples of CCD and HID for Z- and Atoll sources in Figures from Hasinger and van der Klis 1989, Homan et al. 2007a, Lin et al. 2009b, van der Klis 1989, van Straaten et al. 2003). The luminosities reached by the Z-sources are close to and can exceed the Eddington luminosities ($L_{\rm EDD}$) and they trace out roughly Z-shaped tracks in CCDs/HIDs within hours to days (Lin et al. 2009b) during the outbursts. The Z track is divided into the an upper, diagonal, and lower branch, which are

called horizontal, normal, and flaring branches (HB/NB/FB), respectively. Furthermore, Hasinger and van der Klis (1989) groups Z-sources into Sco- (eg. GX 17+2, GX 349+2 and Sco X-1) or Cyg- (eg. Cyg X-2, GX 340+0, GX 5-1) like sources. In the former, the HB is nearly vertical or incomplete and the FB has strong flaring with high count rates, while in the latter the HB is almost horizontal in the HID and count rates decrease on the FB (Homan et al. 2007a, Muñoz-Darias et al. 2014). The Atoll sources span a lower and larger luminosity range (0.001–0.5 L_{EDD} Homan et al. 2007a), tracing out their patterns in CCDs/HIDs on longer timescales (from days to weeks) (Lin et al. 2009b). The X-ray spectra of Atoll sources are soft at high luminosities, but hard when they are faint. The HID patterns of the Atolls are called the extreme island, island, and banana states and Lin et al. (2009b) refers to the Atoll patterns as hard, transitional, and soft states, respectively. Comparing Z- and Atoll sources on the radio – X-ray plane will provide a better understanding of the relationship or transitional nature between Z and Atoll sources.

A source can show transitions between Z and Atoll source signatures. XTE J1701-462 (hereafter XTE J1701) is one such example, while Cir X-1 has also shown these traits (Oosterbroek et al. 1995, Shirey et al. 1998). XTE J1701 is a transient source which showed characteristics of Z-source behaviour when it was first discovered in 2006 (Homan et al. 2007a). It is the first NS transient to show all the characteristics of a Z-source and has a distance estimate of 8.8 $\pm$ 1.32 kpc (Lin et al. 2009b). In the first 10 weeks of its 600 day discovery outburst, XTE J1701 transformed from a Cyg- like source into a Sco- like Z-source, and during the decay it evolved further into an Atoll source. The 2006/7 outburst of XTE J1701 spans a large range in luminosity, from super-Eddington towards quiescence, suggested to imply significant changes in the mass accretion rate as it transitions from Z- to Atoll (Ding et al. 2011). The lightcurve of the XTE J1701 2006/7 outburst was broken down into stages (I – IV) (Lin et al. 2009b) . The last three stages show behaviour of Sco-like sources, and in the fourth stage (IV) it is observed that the HB and NB are no longer present. The CCDs/HIDs resemble those of the bright persistent GX Atoll sources (GX 9+1, GX 9+9, and GX 3+1) which Lin et al. (2009b) classified into the NB/FB vertex and the FB for XTE J1701. Fender et al. (2007) discussed a large scale structure seen in the radio which may be associated with the source; however, Gasealahwe et al. (2023) reported that the structure is likely an extragalactic background source.

The source has since gone into a new outburst during 2022/23 which lasted over 200 days; reports from that outburst include IXPE observations (Cocchi et al. 2023) which were taken on 29-30 September and 8-9 October 2022. Cocchi et al. (2023) reported $\sim$ 4.6 $\pm$ 0.4% linear polarisation of the X-rays from the source during the upper and intermediate horizontal branch, the highest value of polarisation found for this class of source.

In this paper we discuss the new (2022/23) outburst in the radio band with the MeerKAT, comparing it to the first outburst to develop a better understanding of the transitional nature between Z and Atoll. We present a description of the observations in Section 2 and report the results in Section 3. In Section 4.1 we compare the 2006/7 and 2022/23 outbursts, the polarisation constraint in Section 4.2, the in-band spectral index and minimum energy of the flare seen in the 2022/23 lightcurve are reported in Section 4.3. Furthermore, we discuss the position of XTE J1701 on the radio – X-ray correlation in Section 4.4.

Table 4.1: *The table below lists the MeerKAT radio flux densities at 1.28 GHz and assuming a flat spectral index the luminosities at 5 GHz for the 2022/23 outburst. Similarly we list the X-ray flux and luminosities from MAXI calculated with N_H 2.59 and photon index $\Gamma = 1.82$. The MeerKAT radio spectral indices determined for the detections are are also shown in the table below.*

MJD	F_R [mJy/beam]	$L_R \times 10^{29}$ [erg/s]	$F_X \times 10^{-9}$[ergs/cm^2/s]	$L_X \times 10^{37}$ [erg/s]	Spectral index ($\alpha; S_\nu \propto \nu^\alpha$)
59829.50			6.42 ± 0.27	5.95 ± 0.25	
59829.66	<0.07	<0.34			
59831.50			8.73 ± 0.36	8.09 ± 0.33	
59831.71	<0.07	<0.32			
59838.72	0.34 ± 0.02	1.57 ± 0.09			0.26 ± 0.46
59839.50			10.50 ± 2.05	9.73 ± 1.90	
59842.50			15.70 ± 0.81	14.60 ± 0.75	
59842.60	2.62 ± 0.03	12.14 ± 0.14			-0.21 ± 0.26
59846.50			16.40 ± 1.06	15.20 ± 0.98	
59846.74	3.98 ± 0.02	18.44 ± 0.10			-2.53 ± 0.20
59852.54	1.71 ± 0.03	7.90 ± 0.13			-0.08 ± 0.59
59859.50			21 ± 0.60	19.50 ± 0.56	
59859.70	1.31 ± 0.02	6.10 ± 0.11			-0.84 ± 0.25
59867.48	0.92 ± 0.02	4.26 ± 0.10			-0.36 ± 0.21
59867.50			19.60 ± 0.54	18.20 ± 0.50	
59873.50			13.30 ± 0.29	12.30 ± 0. 26	
59873.61	1.32 ± 0.024	6.12 ± 0.11			-0.16 ± 0.22
59880.50			11.30 ± 0.37	10.50 ± 0.34	
59880.64	<0.07	<0.34			
59889.50			7.75 ± 0.39	7.18 ± 0.37	
59889.68	2.53 ± 0.03	11.72 ± 0.13			-1.07 ± 0.21
59894.64	<0.07	<0.32			
59895.50			6.31 ± 0.51	5.85 ± 0.47	
59901.50			12.70 ± 0.74	11.80 ± 0.69	
59901.58	0.80 ± 0.02	3.71 ± 0.11			-0.34 ± 0.19
59909.50			15.30 ± 0.89	14.20 ± 0.82	
59909.58	2.23 ± 0.03	10.33 ± 0.13			-0.74 ± 0.33
59915.50			12.80 ± 0.69	11.90 ± 0.64	
59915.62	0.35 ± 0.02	1.62 ± 0.11			-0.12 ± 0.80
59921.50			7.17 ± 0.94	6.64 ± 0.87	
59922.58	<0.08	<0.35			
59932.35	<0.07	<0.34			
59934.50			9.86 ± 0.44	9.14 ± 0.41	
59939.31	0.22 ± 0.03	1.02 ± 0.12			
59939.50			11.40 ± 0.38	10.6 ± 0.35	
59946.44	<0.08	<0.36			
59946.50			10.50 ± 0.48	9.73 ± 0.45	

Table 4.1: *Continues*

59951.38	<0.09	<0.36		
59951.50			9.40 ± 0.26	8.71 ± 0.24
59958.38	<0.08	<0.35		
59958.50			6.51 ± 0.38	6.03 ± 0.35
59965.42	<0.07	<0.33		
59965.50			6.10 ± 0.68	5.65 ± 0.63
59972.34	<0.14	<0.67		
59972.50			7.13 ± 0.27	6.61 ± 0.25
59979.25	<0.14	<0.66		
59979.50			9.16 ± 0.58	8.49 ± 0.54
59986.38	<0.08	<0.36		
59986.50			6.20 ± 0.53	5.75 ± 0.49
59994.50			5.90 ± 2.82	5.47 ± 2.61
59996.23	<0.14	<0.65		
60001.22	<0.14	<0.65		
60004.50			4.28 ± 0.31	3.97 ± 0.29
60015.25	<0.07	<0.33		
60015.50			1.80 ± 0.17	1.67 ± 0.16
60028.04	<0.07	<0.33		
60028.50			0.01 ± 0.10	0.01 ± 0.10

4.2 Observations

4.2.1 MeerKAT observations

The latest outburst of XTE J1701 triggered follow-up observations with MeerKAT at a central frequency of 1.28 GHz and bandwith of 856 MHz. This was done through the ThunderKAT Large Survey Programme (Fender et al. 2016). XTE J1701 was observed for 29 epochs nearly weekly over a span of seven months from 2022 to 2023. The observations started on the 7 September 2022 (MJD 59829.50) using an average of 61 dishes for a duration of 15 minutes each observation. The semi-automated pipeline, OXKAT[1] (Heywood 2020) was used to reduce the data with observation calibrators J1939-6342 (bandpass, flux calibrator) and J1744-5144 (phase, amplitude calibrator). The first and second generation process of OXKAT were used for this data, using CASA (McMullin et al. 2007) to perform the averaging, flagging steps and do cross- and self-calibration. After the first generation process was complete, the visibility and gain solution plots were inspected and deemed satisfactory, so that the data were then flagged and imaged using the TRICOLOUR and WSCLEAN packages respectively (Offringa et al. 2014). Thereafter, the second generation processing was initiated to do self calibration, plot gain solutions and a second output of images were produced. The flux densities were then determined using PYBDSF (Mohan and Rafferty 2015).

Additionally, we were interested in constraining the polarisation properties of the source during a brief period

[1]for more details see, `https://github.com/IanHeywood/oxkat`

of $\sim$mJy-level flaring between 30 September 2022 and 7 October 2022. We corrected for on-axis instrumental polarisation (which converts unpolarised flux into polarised flux) using the unpolarised bandpass calibrator J1939-6342[1]. Our observations did not include a strongly polarised calibrator, preventing us from correcting the instrumental cross-hand phase. The uncorrected cross-hand phase can cause a circular-to-linear polarisation conversion but does not modify the total amount of polarised flux (see equations 16–19 in, Hales 2017). Therefore, while we cannot measure the relative contributions from circular and linearly polarized emission, we can measure the total polarised flux.

Post-calibration, we produced full I, Q, U, and V Stokes images using WSCLEAN. The Stokes parameters correspond to four fluxes that describe the polarisation state, where I is the total flux, Q and U are related to the linear polarisation, and V is the circularly polarized flux; the total polarised flux is $P = \sqrt{Q^2 + U^2 + V^2}$, and the polarization fraction is P/I. We do not detect a polarised component spatially coincident with XTE J1701. To measure upper limits, we used the CASA task `imfit` to extract the polarised flux by fitting a Gaussian component fixed at the position of the source (i.e., we performed forced aperture photometry). Given that the source is unresolved, we also fixed the shape of the Gaussian to that of the synthesized beam. Using our forced aperture results, we calculated 99.7% (3σ) upper limits on the polarised flux (and polarisation fraction) following the prescription from Vaillancourt (2006). We present our polarisation upper limits in Section 4.2.

4.2.2 MAXI observations

In order to contextualize the radio monitoring with X-ray observations of XTE J1701, we utilized data from the *Monitor of All-Sky X-ray Image* (*MAXI*; Matsuoka et al. 2009b) Gas Slit Camera (GSC). We extracted the daily monitoring light curve of the target in the 2-20 keV band from the public *MAXI* website[2]. For days with a MeerKAT radio observation, we also calculate the X-ray hardness and estimate the X-ray flux. The hardness is calculated by dividing the X-ray count rates in the two sub-bands between 10-20 keV and 2-4 keV. The flux, on the other hand, is estimated by converting the 4-10 keV count rate to the unabsorbed 1-10 keV X-ray flux using WebPIMMS[3]. For this conversion, we assumed an absorbed power law spectral shape with index $\Gamma = 1.82$ and absorption column $N_H = 2.59 \times 10^{22}$ cm^{-2}, as derived in this outburst from observations with the *Neil Gehrel's Swift Observatory* (Chandra 2022).

4.3 Results

During the 2022/23 outburst MeerKAT observed XTE J1701 nearly weekly for 29 epochs. We measured 3σ upper limits for the first two observations (see Table 4.1) and 0.34 ± 0.02 mJy/beam for the first detection. The lightcurve (Figure 4.1) traces the outburst in the radio and the X-ray in the first and second panel respectively. The hardness ratio (10 - 20)/(2 - 4) keV is shown in the third panel, where the points only represent the instances of quasi-simultaneity (Δ t = $\pm$ 1 day) between the MAXI and MeerKAT observations. In the fourth panel of Figure 4.1 we display the in-band radio spectral index over the period of the outburst, where the points are defined by the radio detections. The spectral indices are the slopes determined from 8 frequency bands; 0.91, 1.02, 1.12, 1.23, 1.34, 1.44, 1.55, 1.66 GHz (see Figure 4.4) and at MJDs 59838.72 and 59915.61 the source was

[1]Polarisation calibration was done with a modified version of OXKAT. The calibration routine is available here: `https://github.com/AKHughes1994/polkat`

[2]`https://maxi.riken.jp/top/index.html`

[3]`https://heasarc.gsfc.nasa.gov/cgi-bin/Tools/w3pimms/w3pimms.pl`

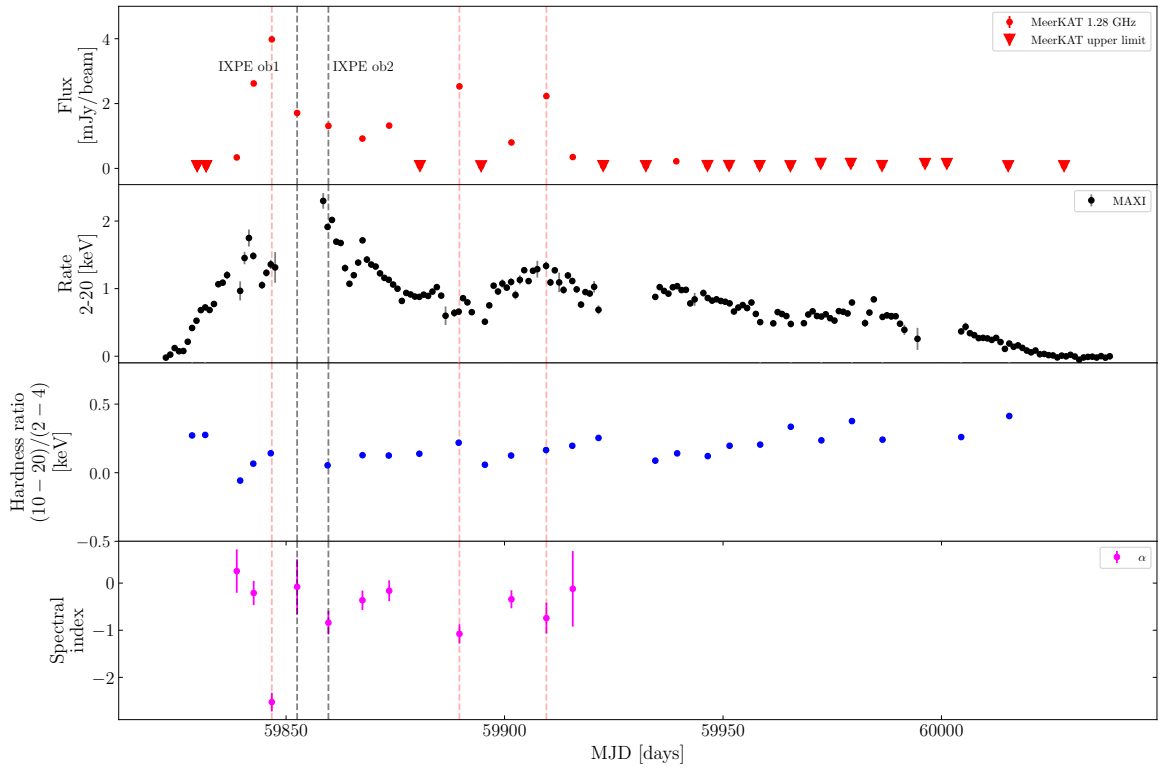

Figure 4.1: *The radio (MeerKAT), X-ray (MAXI), hardness intensity (10-20)/(2-4) keV and radio (MeerKAT) spectral index lightcurves of the 2022/23 outburst of XTE J1701 in the first, second, third and bottom panel respectively. The IXPE observations taken from Cocchi et al. (2023) are indicated with the grey dashed lines and are shown to coincide with our radio detections. The red dashed lines run through the peaks of the radio flares and the radio spectral indices are shown for all the radio detections except the final one from MJD 59939.31 since the source was not detected in several of the lower band frequencies.*

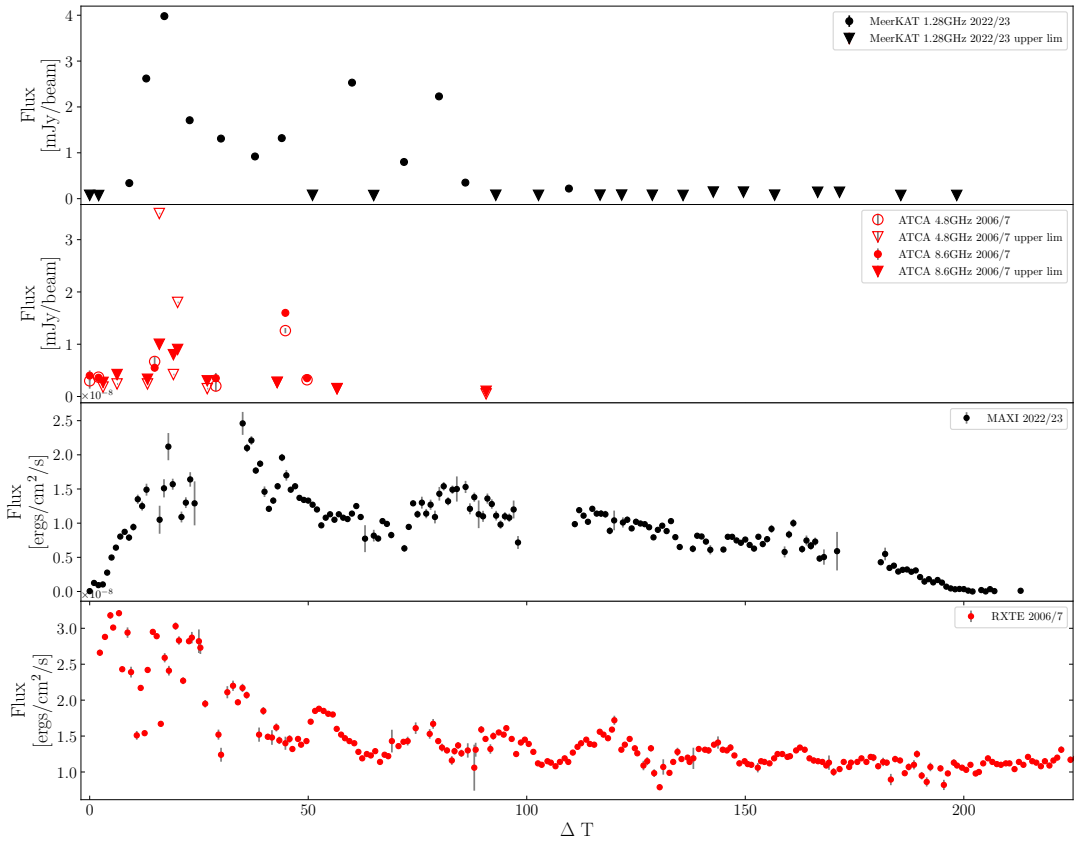

Figure 4.2: *We compare the radio (first two panels) and X-ray (bottom two panels) lightcurves of XTE J1701 for the 2022/23 (black lightcurves) and 2006/7 (red lightcurves) outbursts. T=0 is 53757.91 and 59829.65 for the 2006/7 and 2022/23 outbursts, respectively. In both panels of the radio lightcurves the detections the 3σ upper limits are represented by the upside down triangles.*

not detected in the lower bands but with at least three points we are able to determine a slope for the spectral index. Throughout the outburst we observe the source to go into multiple reflares in the radio and the X-ray. The radio flares peak at 3.98 ± 0.022 mJy/beam (MJD = 59846.74), 2.53 ± 0.029 mJy/beam (MJD = 59889.68) and 2.23 ± 0.027 mJy/beam (MJD = 59909.58). After the first three radio flares MeerKAT did not detect the source after 4 months of observations but XTE J1701 continued detection in the X-ray (see second panel in Figure 4.1).

We place XTE J1701 on the radio – X-ray correlation plane using quasi-simultaneous observations (within the same day) (Figure 4.3). The measurements are the pink circles representing the detection matches and we represent the radio upper limits with pink upside down triangles. A distance of 8.8 kpc was used to determine the radio – X-ray luminosities and assuming a flat spectral index the radio measurements were converted to 5 GHz. We also note that the source lies closely along the averaged Z-source points, an expected result since the source is known to transition from the Z-source to the Atoll during outbursts (Ding et al. 2011, Lin et al.

Table 4.2: *The source size, minimum energy, B-field and temperature of the three flare are calculated using Equations 28, 29, 30 and 31 in Fender and Bright (2019). We use the 1.28 GHz MeerKAT frequency, the flux from each flare peak and a distance of 8.8 kpc is assumed.*

Flare	R [cm]	$E_{\rm min}$ [erg]	$B_{\rm min}$ [G]	$T_{\rm min}$ [K]
First	2×10^{13}	1×10^{38}	0.17	4×10^{10}
Second	2×10^{13}	6×10^{37}	0.18	4×10^{10}
Third	1×10^{13}	5×10^{37}	0.18	4×10^{10}

2009b).

4.4 Discussion

In this section we explore the comparisons of the 2006/7 and 2022/23 outbursts. We measure the in-band spectral energy and minimum energy from the three flares observed in the 2022/23 lightcurve. We then place the transitioning Z-Atoll source on the radio – X-ray correlation plane.

4.4.1 The 2006/7 outburst vs the 2022/23 outburst

The comparison of the two known outbursts of J1701 displayed in Figure 4.2 describe the evolution of the source during those periods. T=0 corresponds to 53757.91 and 59829.65 for the 2006/7 and 2022/23 outbursts, respectively. Lin et al. (2009b) describes Z tracks for the 2006/7 outburst corresponding to MJD 53756.6–53767.3, 53870.5-53876.2, 53893.0–53898.0, 54112.0–54119.0, 54188.0–54196.5, 54268.5–54277.0, and 54290.0–54299.0, respectively. In the last panel of Figure 4.2 we note that in 2006/7 the source was more active past >200 days after the onset of the outburst Lin et al. (2009a) suggested the transition to Atoll only occurred on 25 July 2007 (MJD 54306.57, more than 550 days into the outburst). As a result, we propose the source remained in the Z state throughout the 2022/23 period of our observations. In Figure 4.2 we compare the radio lightcurves from the 2022/23 (top panel) and 2006/7 (second panel) outbursts. We note that more flares were observed in the 2022/23 radio lightcurve compared to the 2006/7 one, however, this is likely due to a difference in sampling since we were able to observe more consistently for a longer period. The X-ray daily averages indicate more flaring in the 2006/7 outburst (Figure 4.2 bottom panel). The hardness ratio was determined using energy bands $(10-20)/(2-4)$ keV and is displayed in the third panel of Figure 4.1. We observe a pattern where the hardness ratio appears to rise with every radio flare observed. We are however, unable to make any strong statements on the connection between X-ray states and radio emission as our weekly radio sampling is much slower than the typical X-ray state change timescale for Z source of $\sim$ hours.

4.4.2 Polarisation constraints

In Figure 4.1 we indicate the IXPE observations Ob1 and Ob2 with grey dashed lines from Cocchi et al. (2023). The authors observe a polarisation of 4.6 ± 0.4 % (Ob1) on the decay of the first flare and later upper limit 1.5% (Ob2). We constrain the polarisation with 3σ upper limits 8.6% and 8.8% for Ob1 and Ob2 respectively. During the 2006/7 outburst, Fender et al. (2007) determined upper limit constraint <6% for linear and circular polarisation when the source was brightest following the NB/HB track. On the other hand Cocchi et al. (2023) argue the polarisation they measure for the 2022/23 outburst is strongest in the intermediate HB track.

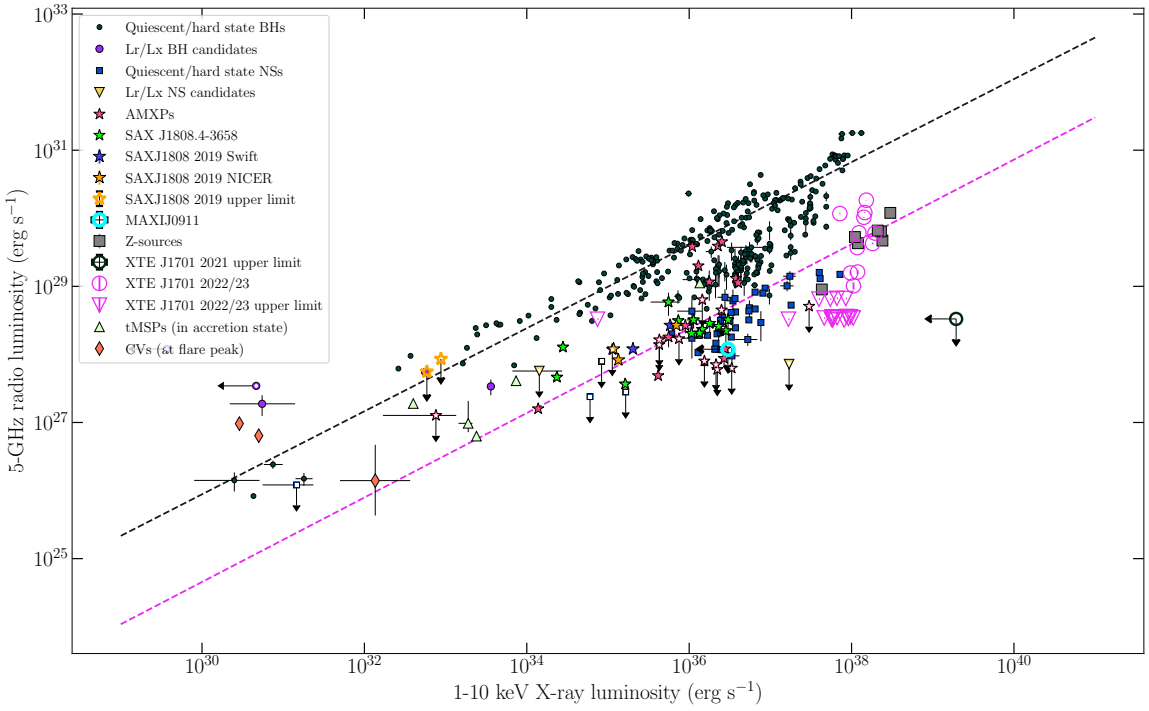

Figure 4.3: *The radio: X-ray correlation plane, including BH and NS star sources from Bahramian et al. 2018, Migliari and Fender 2006. The black dashed line indicates the slope for the standard track for BH systems. On the other hand, the pink slope represents the best fit (0.82 ± 2.4) for our 2022/23 XTE J1701 (pink markers) results and we find that the source lies close to the region of the six quasi-persistent Z-sources (grey squares).*

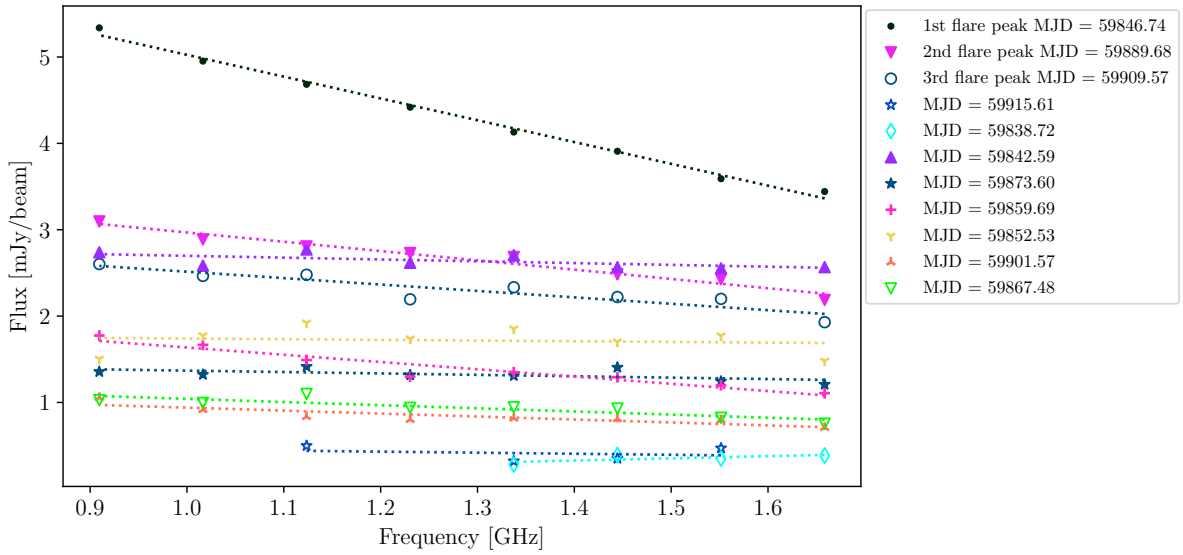

Figure 4.4: *In-band spectra of the MeerKAT detections for the 2022/23 outburst, with slopes representing the spectral indices. The first, second and third radio flare peaks are highlighted in the legend along with the MJDs for the detections.*

4.4.3 In-band spectral index and minimum energy of the 2022/23 flares

We measured the spectral index of the radio detections, including the peaks of the flares from the 2022/23 outburst (see Figure 4.4). Using scipy's linear regression to fit the best fit line, the slope for the flares are -2.53 $\pm$ 0.20 (which we conclude is not a physical result due to the steepness of the measurement), -1.08 $\pm$ 0.21 and -0.74 $\pm$ 0.33 for the first (MJD 59846.74), second (MJD 59889.68) and third (MJD 59909.58) flare respectively (Figure 4.4). These results suggest the flare peaks are optically thin and flatter from the first flare to the third complementing the re-ignition of the jet with the reflaring. The relatively poor sampling and hint of a flatter radio spectrum at our first detected epoch suggests we cannot rule out the flare peaks being due to the transition from optically thick to optically thin ejecta.

Under the assumption that the peaks are due to this evolution in synchrotron self-absorption, the minimum energy produced at the peak of each flare can be estimated using Equation 29 of Fender and Bright (2019), the values are $E_{\rm min} = 1 \times 10^{38}$ erg, $E_{\rm min} = 6 \times 10^{37}$ erg and $E_{\rm min} = 5 \times 10^{37}$ erg for the first, second and third peak respectively. However, as noted in Fender et al. (2023) poor radio sampling can lead to a blending of multiple shorter flares and a consequent *underestimate* of the total output kinetic energy by over an order of magnitude. Assuming a similar scaling, which is uncertain but may be conservative given the known tendency for Z sources to produce many rapid flares, XTE J1701 is likely to have output at least a few times 10^{39} erg in its jets during the outburst. Better sampling, resolution of jets to measure bulk Lorentz factor, etc, in the future are only likely to drive up such estimates. In Table 4.2 we include the value of the source size R, magnetic field (B-field) and temperatures of the three flares. In a BH system like V404 Cyg the minimum energies for the flares range between 10^{38--39} erg and the B-field is about three times as large for V404 Cyg compared to the our results for XTE J1701 (see V404 Cyg results in Fender et al. 2023). Fender and Bright (2019) further discuss that Cyg X-3 and GRS 1915+105 have minimum energies during flaring events that range of the order of 10^{38--45} erg, and the B-fields can reach as high as 2 – 4 times our XTE J1701 results. On the other hand, the three BH systems have temperatures similar to $T_{\rm min}$ described in Table 4.2 and the minimum source size of $R_{\rm min} = 7{\times}10^{13}$ cm for V404 Cyg which is about 3 times what we get for XTE J1701 ($R_{\rm min} = \beta_{\rm m} c \Delta t$ where, $\beta_{\rm m}$ is Equation 28 in Fender and Bright 2019 and Δt is the variability timescale, see also Fender et al. 2023). While the minimum energy for V404 Cyg is similar to XTE J1701, the rest of the BH systems indicate that a NS system like XTE J1701 has less powerful flaring than BH systems.

4.4.4 Radio – X-ray correlation

The radio luminosity and X-ray luminosity correlation is used as a tool to understand the connection between jets (radio) and accretion (X-rays) in X-ray binary systems (e.g. Corbel et al. 2003, 2013, Hannikainen et al. 1998). While in black holes use of the plane is largely limited to sources with quasi-steady compact jets in the hard X-ray state, the sampling of neutron stars in the plane is poor enough, and their flares in general weak enough, that can be instructive to place them in the plane even if not in an equivalent of the black hole hard state (see also discussion in Deller et al. 2015 and a comparison of BH and NS jet production in Muñoz-Darias et al. 2014)

The detection matches of the XTE J1701 (pink points Figure 4.3) once fit using SCIPY linear regression reveals a slope of 0.82 $\pm$ 2.4. The large error in the slope is a result of the broad scatter in the radio luminosity range. The NS systems on the plane lie nearly parallel to the BH slope and XTE J1701 follows along the NS

distribution at the higher end of the luminosity range where $L_R > 10^{29}$ erg/s and $L_X > 10^{38}$ erg/s. Corbel et al. (2013) reveals that GX 339 defines the 'standard' track for BH systems on the correlation plane with slope $\approx$ 0.6 (see track indicated with the black dashed line in Figure 4.3) and BH systems that lie outside the 'standard' track are considered outliers (Corbel et al. 2013). In Gasealahwe et al. (2023) we find a slope ≈ 0.7 for SAX J1808.4-3658 (blue and orange stars in Figure 4.3), this source lies along other NS systems (blue squares in Figure 4.3) and along the luminosity range of the BH outliers. Thus, the addition of the XTE J1701 slope may indicate BH and NS systems could follow a similar trend on the radio – X-ray correlation plane.

4.5 Conclusions

The second recorded outburst of XTE J1701 reveals multiple flare events in both the radio and the X-ray lightcurves. We perform a comprehensive analysis of the outburst and we compare the 2006/7 outburst to the 2022/23 outburst in both the radio and the X-ray and propose the 2022/23 outburst remained in the Z-state throughout the our observation period (lasting ≈ 200 days). We determine the radio spectral index throughout the radio active period and find that the source is optically thin overall and slightly flatter from the first to the final radio flare due to the jet re-ignition during flaring. We calculate the minimum energy for the peaks of the radio flares; $E_{\rm min} = 1 \times 10^{38}$ erg, $E_{\rm min} = 6 \times 10^{37}$ erg and $E_{\rm min} = 5 \times 10^{37}$ erg for the first, second and third peaks respectively and propose that with improved sampling the minimum energy may be $\approx 10^{39}$ erg. We propose that a system like XTE J1701 has weaker flaring mechanism than BH systems because of its smaller source size, minimum energy and magnetic fields compared to BH systems during such flaring events. Furthermore, we place XTE J1701 on the radio – X-ray correlation plane using a quasi-simultaneity of a day for the MeerKAT and MAXI observations. The source is placed in the higher end of the luminosity range, such that it occupies the same region of space as the rest of the Z-sources. We determine a slope 0.82 ± 2.4 and due to the large uncertainty we cannot define strict comparisons to the standard slope of BHs systems (slope range 0.5 – 0.7).

Acknowledgements

KVSG acknowledges support from the University of Cape Town and the South African NRF. RF would like to thank UKRI, the ERC and The Hintze Family charitable foundation for their support. JvdE acknowledges a Warwick Astrophysics prize postdoctoral fellowship made possible thanks to a generous philanthropic donation. IMM is supported by the South African NRF and the UCT VC 2030 Future Leaders Programme.
The MeerKAT telescope is operated by the South African Radio Astronomy Observatory, which is a facility of the National Research Foundation, an agency of the Department of Science and Innovation. We acknowledge the use of the ilifu cloud computing facility – `www.ilifu.ac.za`, a partnership between the University of Cape Town, the University of the Western Cape, Stellenbosch University, Sol Plaatje University and the Cape Peninsula University of Technology. The ilifu facility is supported by contributions from the Inter-University Institute for Data Intensive Astronomy (IDIA – a partnership between the University of Cape Town, the University of Pretoria and the University of the Western Cape), the Computational Biology division at UCT and the Data Intensive Research Initiative of South Africa (DIRISA).

Data Availability

The data underlying this article will be shared on reasonable request to the corresponding author.

Chapter 5

Cir X-1 Publication -

The following chapter is based on the published article for the Cir X-1 results. Journal: Monthly Notices of the Royal Astronomical Society, Volume 541, Issue 4, pp. 4011-4024.

A relativistic jet from a neutron star breaking out of its natal supernova remnant

K. V. S. Gasealahwe,[1,2] K. Savard,[3] I. M. Monageng,[1,2] I. Heywood, [3] R. P. Fender,[1,3] P. A. Woudt,[1] J. English, [4] J. H. Matthews, [3] H. Whitehead, [3] F. J. Cowie,[3] A. K. Hughes,[3] P. Saikia,[5] S. E. Motta,[3,6]

[1]Department of Astronomy, University of Cape Town, Private Bag X3, 7701 Rondebosch, South Africa
[2]South African Astronomical Observatory, P.O. Box 9, 7935 Observatory, South Africa
[3]Department of Physics, University of Oxford, Denys Wilkinson Building, Keble Road, Oxford OX1 3RH, UK
[4] Department of Physics and Astronomy, University of Manitoba, Winnipeg, Manitoba, Canada R3T 2N2
[5]Center for Astrophysics and Space Science (CASS), New York University Abu Dhabi, PO Box 129188, Abu Dhabi, UAE
[6]Istituto Nazionale di Astrofisica, Osservatorio Astronomico di Brera, via E. Bianchi 46, 23807 Merate (LC), Italy

Abstract

The young neutron star X-ray binary, Cir X-1, resides within its natal supernova remnant and experiences ongoing outbursts every 16.5 days, likely due to periastron passage in an eccentric orbit. We present the deepest ever radio image of the field, which reveals relativistic jet-punched bubbles that are aligned with the mean axis of the smaller-scale jets observed close to the X-ray binary core. We are able to measure the minimum energy for the bubble, which is around $E_{min} = 10^{45}$ erg. The nature and morphological structure of the source were investigated through spectral index mapping and numerical simulations. The spectral index map reveals a large fraction of the nebula's radio continuum has a steep slope, associated with optically thin synchrotron emission, although there are distinct regions with flatter spectra. Our data are not sensitive enough to measure the spectral index of the protruding bubbles. We used the PLUTO code to run relativistic hydrodynamic simulations to try and qualitatively reproduce the observations with a combined supernova-plus-jet system. We are able to do so using a simplified model in which the asymmetrical bubbles are best represented by supernova explosion which is closely followed (within 100 years) by a phase of very powerful jets lasting less than 1000 years. These are the first observations revealing the initial breakout of neutron star jets from their natal supernova remnant, and further support the scenario in which Cir X-1 is a younger relation of the archetypal jet source SS433.

Keywords

radio continuum: transients – X-rays: binaries – stars: neutron – stars: jets

5.1 Introduction

Circinus X-1 (hereafter Cir X-1) is a X-ray binary (XRB) that has since its discovery in 1971 (Margon et al. 1971) shown conflicting characteristics. The discovery of X-ray bursts from the European X-ray Observatory Satellite (EXOSAT) (de Korte et al. 1981, Taylor et al. 1981) observations taken in 1984 suggested a neutron star (NS) accretor with possible Type I bursts, however, Type II bursts could not be ruled out (Tennant et al. 1986). Later, Linares et al. (2010b) confirmed that the bursts are Type I using the observations from the Rossi X-ray Timing Explorer (RXTE) (Bradt et al. 1993) and Neil Gehrels Swift telescope (XRT) (*Swift*; Burrows et al. 2005), confirming the compact object is a NS. Moreover, the binary system is probably in an elliptical orbit of period 16.6 days (Kaluzienski et al. 1976).

The source appears to show mildly relativistic jets (Fender et al. 1998) which may be precessing close to the plane of the sky (Coriat et al. 2019) as well as evidence for ultrarelativistic jets with an angle close to the line of sight (Fender et al. 2004b). The X-ray behaviour of Cir X-1 has been studied in detail during outbursts, yielding characteristics from the Hardness Intensity (HID) and Colour-Colour (CD) diagrams of both Z-sources and Atoll sources (Oosterbroek et al. 1995, Shirey et al. 1999). Z-source/Atoll sources are low mass – low magnetic field NS star systems, distinguished by the characteristic patterns they trace in HIDs and CCDs during outbursts (Hasinger and van der Klis 1989). van der Klis (1994) predicted that Cir X-1 may be an Atoll that shows Z-source behaviour during outbursts but Shirey et al. (1999) confirmed complete Z-track behaviour. Therefore, Cir X-1 exhibits properties consistent with both Z and Atoll sources, indicating it is likely a low-mass X-ray binary. And, although the Type I bursts observed from Cir X-1 are consistent with accretion from an H/He enriched companion, the age and nature of the binary system has been a puzzling factor due to the association with the extended nebulae in the region of source.

Clark et al. (1975) suggested that the X-ray binary was born in the nearby supernova remnant G321.9-0.3 (see Fig. 5.1.) moving away from it at high speed due to a large kick in the natal supernova explosion. Later,

distance and age estimates for both were shown to be broadly consistent. Haynes et al. (1986) first reported the smaller diffuse radio nebula centred on the X-ray binary itself and speculated that the southern extension of this nebula towards G 321.9-0.3 supported the hypothesis of Clark et al. (1975). Stewart et al. (1993) reported radio imaging from the Australia Telescope Compact Array (ATCA) of the Cir X-1 nebula and argued that apparently swept-back radio jets further supported the Clark et al. (1975) hypothesis. During the 1990s further detailed radio observations revealed a smaller jet-like structures within the nebula (e.g. Fender et al. 1998), and the association with G321.9-0.3 was widely accepted.

However, Mignani et al. (2002) reported strong upper limits on the proper motion of the optical counterpart using Hubble Space Telescope (HST) observations separated by over 8 years, ruling out an association between G321.9-0.3 and the X-ray binary. Focus returned to understanding the nature of the Cir X-1 nebula itself and associated jets, with increasingly detailed radio images presented variously in Tudose et al. (2008) (which also presented proper motion limits on the core consistent with the HST results of Mignani et al. 2002), Calvelo et al. (2012) and Coriat et al. (2019). Coriat et al. (2019) reported the first detailed study into whether or not the jets were precessing, as hinted at in previous more sparse comparisons of jet images. In the meantime, our understanding of the relationship between the X-ray binary and the nebula had also changed. Heinz et al. (2013) used *Chandra* observations to confirm that the Cir X-1 nebula is the natal supernova remnant of Cir X-1. The authors determined a maximum age of 4600 years for the supernova remnant, thus making Cir X-1 the youngest known XRB. The high-resolution X-ray imaging available with *Chandra* also revealed X-ray structures, within the outer shell of the nebula and aligned with the radio jets (Sell et al. 2010, Soleri et al. 2009). Therefore, prior to the new MeerKAT imaging and analysis presented here, the consensus was that Cir X-1 was a very young neutron star X-ray binary. Johnston et al. (2016) propose that the companion is an unusual "puffed up" star as a result of heating and the deposition of energy from the supernova explosion. Furthermore, Heinz et al. (2013) argue a likely high mass companion following a core collapse supernova explosion. However, the Z-source/Atoll nature of the source supports the alternative evolved low-mass companion scenario the authors discuss. Heinz et al. (2015) determined the position to be at a distance of $9.4^{+0.8}_{-1.0}$ kpc.

In this paper, we present new deep imaging of Cir X-1 with the MeerKAT radio telescope. Due to the striking resemblance, we named the nebula the 'Africa nebula'. The imaging results are supported by detailed numerical simulations, which demonstrate our knowledge of the source was yet an incomplete picture.

5.2 MeerKAT observations

MeerKAT hosted a large monitoring campaign for Cir X-1, observing the source daily for 34 epochs at a central frequency of 1.28 GHz. This was done through the ThunderKAT Large Survey Programme (Fender et al. 2016). Although our MeerKAT data were collected to monitor outbursts over time, we do not present the time-series analysis and focus instead on the deep broadband radio image of Cir X-1 and the surrounding field. A total of 8.5 hrs was spent observing, using an average of 61 dishes for each observation. J1939-6342 was the primary calibrator (flux, bandpass) and the secondary (phase) calibrator was J1424-4913. The semi-automated pipeline, OXKAT[1] (Heywood 2020) was used to reduce the data. Each epoch was imaged using a modified OXKAT recipe for this field because of the multiple bright large-scale structures within the field. The 1GC, Flag-only, 2GC-multiscale and 3GC peeling scripts were used in succession to image each observation (see Heywood et al. 2022 for a detailed description of the calibration and imaging procedures). In order to improve the image, two of the

[1] for more details see, `https://github.com/IanHeywood/oxkat`

bright background sources were peeled (>3 Jy in the North and South region of the field). To create the deep image we made a clean mask with a pixel threshold of 0.002, summing the 30 epochs (total of 7.5 hrs) of the best images (such that the epochs 4, 11, 14, 15, were excluded due to bad artefacts). We then ran a WSCLEAN job with the new mask on the 30 measurements sets, with multiscale parameters 0,3,9,18,36, weighted Briggs of -0.3 and a circular beam to create the final image.

5.3 Results and Analyses

In Fig. 5.1 we present our deep 7.5 hrs radio image of the Cir X-1, Africa Nebula and surrounding field, with a 3σ background rms of $38.37\,\mu Jy/beam$. In Figures 5.2, 5.3 and 5.8, are zoom-in versions of the deep image highlighting Cir X-1 and the surrounding Africa nebula. Fig. 5.2 has detailed labelling. We label the central source as 'Core, XRB' and the surrounding structure of the nebula as 'shell'. Within the shell we identify 'jets/shock' which we label 'NW/SE shock' (previously referred to as 'caps' (Sell et al. 2010)). These are presumably the now slow precessing jets opposed to the fast fixed-axis jets assumed in Section 5.4.2. The region of space perpendicular to the jets is named the 'pockets' (identifying the spectrally flat regions perpendicular to the jets which are seen in Fig. 6.5) and south of the shell is an extension we label the 'southern tip'. Although, these features are visible in the previous radio images (Coriat et al. 2019), we present an exceptionally resolved nebula. Improving the visibility of the asymmetric structures we call 'rings' and revealing previously unobserved features such as those labelled 'bubbles', extending from the base of the rings. In the following, we analyse our observational results through a sub-band intensity map, a spectral index map and determine the minimum energy present in the NW bubble and the nebula (only the region within the shell). Subsequently, we simulate the structure of the nebula and investigate the jet parameters that may have formed the bubbles we observe in the radio image (see Section 5.4 and 5.5).

5.3.1 Sub-band Intensity Map

In order to illustrate the features of the nebula with some indication of which frequencies dominate at which location, we constructed the composite image displayed in Fig. 5.3. Although the full frequency range of the radio continuum observation consists of 8 sub-bands, we only selected the three sub-band FITS files (without primary beam correction; 1.016 GHz, 1.230 GHz and 1.444 GHz) that were the least impacted by striations in their background noise levels. Using the CARTA visualization software[1], we adjusted the intensities of these data using limits on the histogram of values along with logarithmic and non-linear stretches. The grayscale output png files were input into the Gnu Image Manipulation Package (GIMP)[2].

Investigation of the primary beam corrected sub-bands showed that the NW bubble appears intermittently between bands, depending on the signal-to-noise ratio. This bubble is delineated most strongly in the sub-band centred at 1.016 GHz. To highlight this information, we duplicated a segment of this sub-band image capturing the bubble and blended this bubble image with the 1.016 GHz field of view.

We subsequently assigned colours: the bubble-enhanced sub-band centred at 1.016 GHz was assigned rose, the sub-band at 1.230 GHz yellow-green, and 1.444 GHz blue-green. These colour images were intensity adjusted and combined, as described in English (2017), into a resultant colour 'combined sub-band' image. Next the total intensity, full-frequency (i.e. wide-band) image was assigned red. Then the inner region of the full-length of the nebula was masked in the wide-band image using GIMP's 'layer mask' functionality. This exposed the

[1] https://cartavis.org/
[2] https://www.gimp.org/

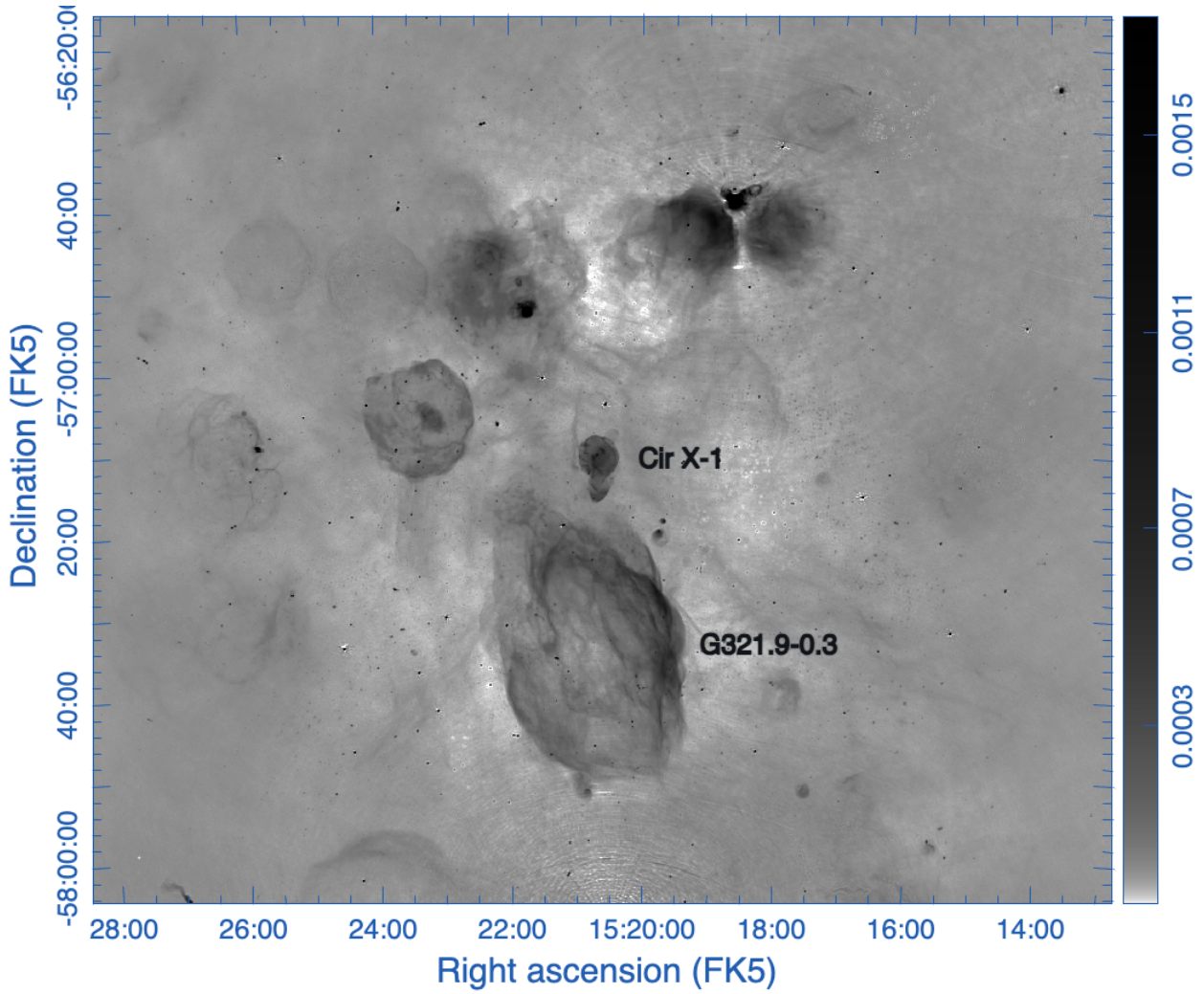

Figure 5.1: *The MeerKAT L band image of the Cir X-1, Africa nebula and surrounding wide field with a primary beam FWHM ∼66(1.1 °), constructed with 30 epochs of data, we label Cir X-1 and the formally assumed supernova remnant of origin G321.9-0.3.*

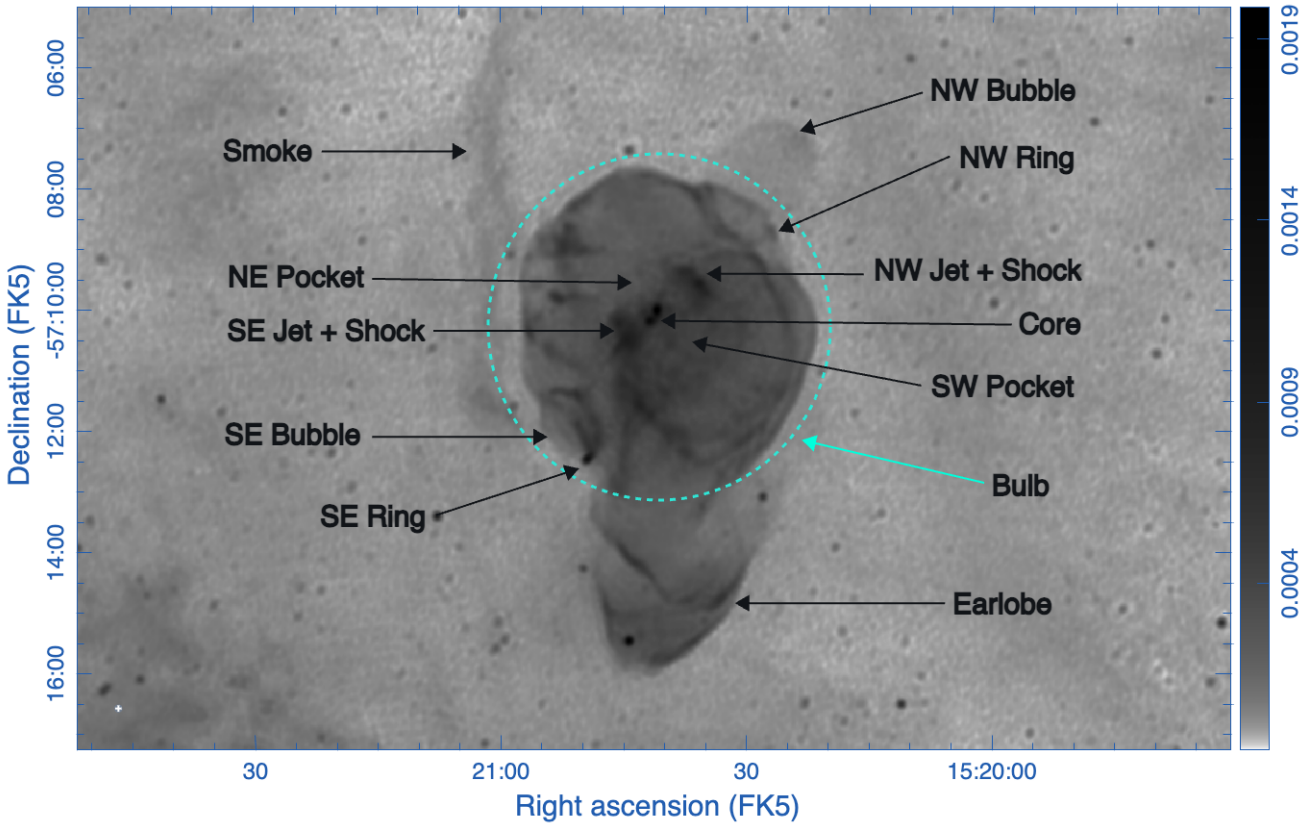

Figure 5.2: *The zoomed-in version of Fig. 1. Highlighting Cir X-1, the Africa nebula and the newly revealed jet-punched bubbles (labelled NW and SE Bubble). We identify and label the core, XRB, the jet shock fronts, rings, pockets (more distinguishable as the spectrally flat regions in line with the core seen in the spectral index map Fig. 6.5). We further separate the nebula into the shell region and name the extension the southern tip.*

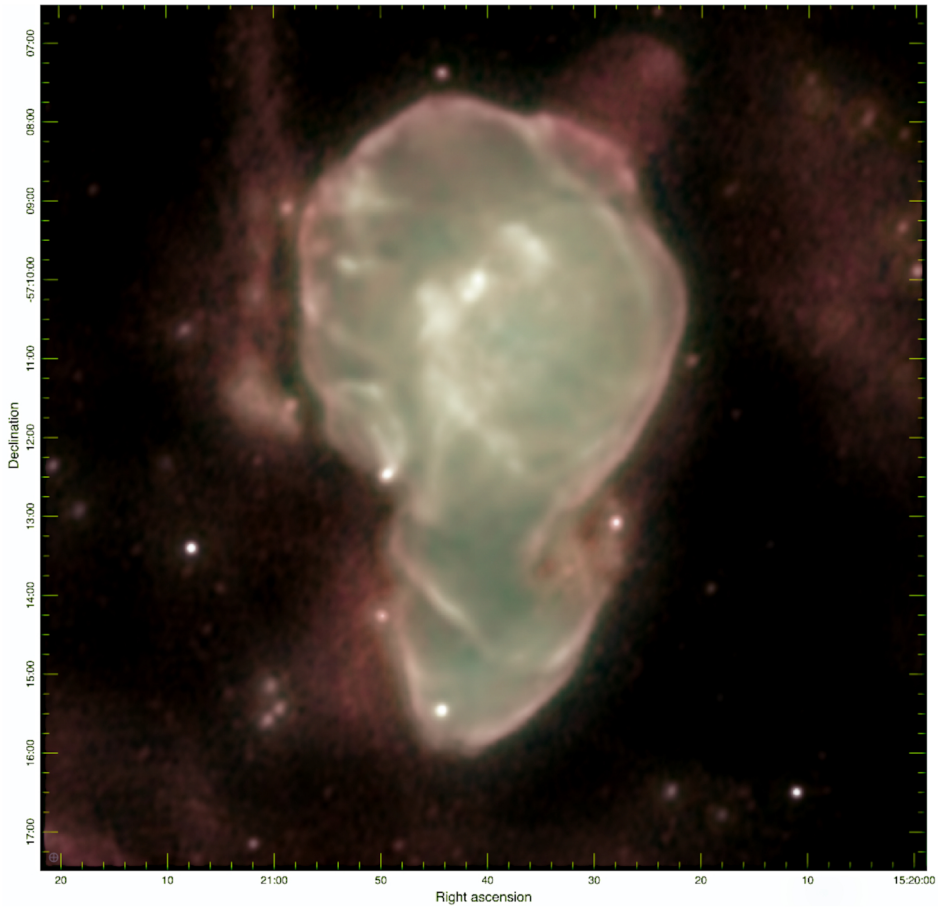

Figure 5.3: *Sub-band Intensity Information. Colour was assigned to three sub-bands of the radio continuum observations, which were subsequently combined and adjusted as described in English (2017). The total intensity wide-band image was assigned red. The central region of the nebula was masked in the wide-band image in order to expose the colour combined sub-band image when their layers in GIMP are blended. See the text for more detail.*

coloured combined-sub-band image (described above) when the layers containing the wide-band and sub-band images were in turn combined. Finally, masks were also employed to adjust the colour and darkness of the surrounding, non-nebular region as well as the white balance of the point sources.

5.3.2 Spectral Index Map

We measure the global spectral index in the shell of the nebula to be -0.49 +/- 0.19. However, as seen in left panel of Fig. 6.5 (the spectral index map), the shell mainly consists of values more negative than -0.8 but the global value is affected by some regions that are much less negative. Perception-based colour schemes (English et al. 2024), used in left panel of Fig. 6.5, distinguish the conventionally 'steep' slopes (spectral index more negative than -0.8) in the Spectral Energy Distribution (SED) from 'flat' slopes and/or noise (spectral index more positive than -0.1). The edges of the full nebula, including edges of the southern tip, are flat, which could be due to the larger uncertainties in these regions of the map (see spectral index error map in right panel of Fig. 6.5). The centres of the shell's pocket regions are also flat, and, the uncertainty is lower in these regions (particularly the SW pocket). The bubbles, including the upper edge of the NW bubble are too faint to have

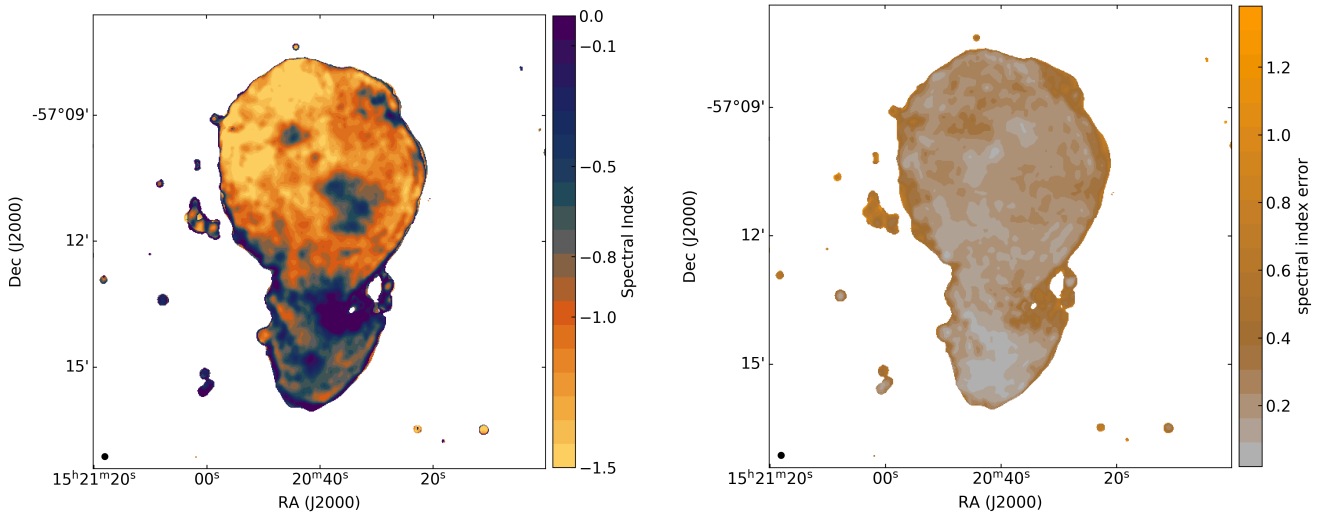

Figure 5.4: *Left panel: Spectral Index Map: Values more positive than -0.1 are conventionally referred to as flat, though these values may also be generated by noise. Values more negative than -0.8, where this colour map has a greyish divergent point, are conventionally referred to as steep. Values more negative than -1.5 are assigned yellow. The perception-based colour tables used in these maps, along with tutorials for applying them, were produced by English et al. (2024) (find at https://github.com/mlarichardson/CosmosCanvas). Right panel: Spectral Index Error Map: Grey is associated with low error. Most regions in the left panel around the edge of the nebula are purple-ish due to this. However there are dark cyan through purple regions interior to the nebula with low noise that therefore have flat spectral slopes. Note that the uncertainty on the alpha values of the central point source and jet-lobes is low.*

measurable spectral indices. We propose that this low luminosity is because they are less dense regions. In the spectral index map (Fig. 6.5 left panel), the jet emission (in shock in Fig. 5.2) appears to be steep (more negative than -0.8). Even steeper are the regions beyond the centres of the pockets contained within the shell (spectral index -1.0 to -1.5). As with other synchrotron nebula from supernova remnants to radio galaxies, the steep spectra are indicative of optically thin synchrotron emission from electrons which may have diffused from their acceleration sites. The flatter regions are likely closer to the sites of particle acceleration and/or have some optical depth.

5.3.3 Minimum energy

We determine the minimum energy for the protruding NW bubble and the nebula. The measured lengths are 1.68‘ for the NW bubble and 5.83‘ for the nebula. Using a distance of 9.4 kpc, we determine the source size R : 7.09×10^{18} cm for the NW bubble and 2.46×10^{19} cm for the nebula. The minimum energy equipartition equation[1] is used when the luminosity and the size of the source are measurable. Therefore, invoking Eq. (5.1), where η is the energy associated with the protons that accompany the electron and is assumed 1 for the minimum energy condition. The filling factor (f) is assumed to be 1 and the luminosity L is given by Eq. (5.2) for MeerKAT frequency range 909 MHz - 1.65 GHz. For the NW bubble $L = 1 \times 10^{30}$ erg/s and for the nebula

[1]see more detail in `https://github.com/robfender/ThunderBooks`

$L = 7 \times 10^{31}$ erg/s, we also determine $c_{12} = 3 \times 10^7$.

$$E_{\min} = 0.92\eta^{\frac{4}{7}} c_{12}^{\frac{4}{7}} f^{\frac{3}{7}} R^{\frac{9}{7}} L^{\frac{4}{7}} \tag{5.1}$$

$$L = 4\pi D^2 F_\nu (\nu_2 - \nu_1) \tag{5.2}$$

The minimum energy that is measured is therefore $4{\times}10^{45}$ erg and $2{\times}10^{47}$ erg for the NW bubble and the nebula respectively. These values are compared to the energy estimates determined from the numerical simulations in Section (5.4.2).

5.4 Numerical Simulation of the Cir X-1 and Africa Nebula system

The deep radio images presented in this work unveil previously unseen features in this system, most notably a large and small bubble (we label NW and SE bubble respectively) symmetrically protruding out of the nebula along the axis of the known jets. The coincidence of these bubbles along the jet axis suggests that past jet activity could indeed be responsible for or at least linked with the formation of these bubbles. We hypothesize that these bubbles are punctures in the supernova remnant caused by the jet launched by Cir X-1: the jet is launched some time post-SN explosion, the jets catch up with the SN remnant, and then they interact with the remnant such that they blow the observed bubbles which we see today.

Although jet activity is visible in this image (presented and discussed in detail in Coriat et al. (2019) and Cowie et al 2025. in prep), the apparent precession angle of these jets simply gauged from the width of their termination shocks appears too wide to be responsible for the comparatively narrow puncture at the base of the bubbles. Additionally, the jets appear to produce termination shocks within the nebula (labelled as shocks in Fig. 5.2), rather than at the surface of the nebula. We therefore propose that there exists at least two jet modes in Cir X-1. Cowie et al. (2025, in prep) propose that the jets responsible for the inner shocks visible in the radio image are relatively slow ($v_{\rm jet} \sim 0.3$c), while we propose a set of fixed-axis fast jets ($v_{\rm jet} \sim$ c) launched at an earlier time are responsible for the radio bubbles we see today.

To test this hypothesis, as a proof of concept, we run numerical simulations representative of the basic components we observe in the system (a supernova explosion, and a set of symmetric jets launched from the core) to try to reproduce the observed morphology.

5.4.1 Numerical Methods

The simulations in this paper are relativistic hydrodynamic (RHD) simulations run using the `PLUTO` code (Mignone et al. 2007a). The code computes the numerical solutions to the RHD system of equations, evolving the conservative set of variables

$$\boldsymbol{U} = (D, m_1, m_2, m_3, \mathcal{E}_t)^T$$

with laboratory mass density D, momenta $m_{1,2,3}$ and total energy $\mathcal{E}_t$ densities, according to the conservation equations

$$\tfrac{\partial}{\partial t} \begin{pmatrix} D \\ m \\ \mathcal{E}_t \end{pmatrix} + \nabla \cdot \begin{pmatrix} D\boldsymbol{v} \\ \boldsymbol{m}\boldsymbol{v} + P\mathcal{I} \\ \boldsymbol{m} \end{pmatrix}^T = \begin{pmatrix} 0 \\ 0 \\ 0 \end{pmatrix}$$

with velocity $\boldsymbol{v}$, thermal pressure P and identity matrix $\mathcal{I}$.

At each timestep, the code converts these conservative variables to primitive variables in the lab-frame (rest-mass density ρ, three-velocity $\boldsymbol{v}$ and pressure p) which make up the outputs of the simulation, as well as the initial and boundary conditions. Lastly, we employ the Taub-Matthews equation of state (Mignone and McKinney 2007, Taub 1948) which describes a relativistic perfect gas as a function of temperature, and is therefore flexible to both relativistic and non-relativistic regimes.

We assume a 2D cylindrical geometry in the simulations, which lends itself well to the observed geometry of the nebula shell and bubbles, neglecting the southern tip feature which we are not aiming to reproduce in the scope of this work. The simulation is aligned such that the jet runs along the axisymmetric axis of the simulations, and the core is in the centre of the simulation.

The domain is a static grid split into 1500×3000 computational cells. This constitutes the 2D grid which is rotated completely about its longest axis, making each cell square toroidal in shape and occupying a pseudo-3D volume. The boundaries are set to be outflowing, with the exception of the axisymmetric boundary the simulation is rotated about.

The simulation runs in non-dimensional 'code' units which are translated to physical units with time and length scales appropriate for the system. These scaling units are defined as: unit density $\rho_0 = 1.673 \times 10^{-24}\,\mathrm{g\ cm^{-3}}$, unit length $L_0 = 3 \times 10^{16}$ cm, and unit velocity $v_0 = c$, making units of time $t_0 = 3.173 \times 10^{-2}$ years, or 1.001×10^6 seconds. Each simulation computational cell is one code unit across, meaning the domain has a physical resolution of $15 \times 30 \times 10^{18}$cm. The resolution was selected such that the morphology of the simulations remained consistent if the resolution was increased, but did not pose excessive computational costs.

In terms of numerical integration, the code offers several choices for spatial reconstruction and time-stepping algorithms. We use a linear reconstruction of primitive variables as the spatial order of integration, and a 2^{nd} order total variation diminishing (TVD) Runge-Kutta scheme to evolve timesteps. To compute the flux between cells, we use the Harten–Lax–van Leer contact (HLLC) Riemann solver (Mignone and Bodo 2005), along with the least diffusive flux limiter available in `PLUTO` (monotized central difference). Lastly, we enable additional dissipation in the proximity of strong shocks ('shock-flattening') with a multi-dimensional strategy.

5.4.2 Simulation Setup

We construct a simulation to reproduce a basic supernova explosion, and a relativistic jet launched from the position of the core. We do so with methods similar to those presented in Goodall et al. (2011), a similar study of an 'older-sibling' analogous system, SS433.

The HMXRB SS433 exhibits remarkably similar properties to Cir X-1, most notably its positioning within its assumed natal supernova remnant (the W50 nebula) which also shows asymmetric bubble-like features along its jet axes. Although SS433 is a comparatively older example of this phenomenon (Likely 10^4 to $< 10^5$ years old), many of the initial simulation conditions that Goodall et al. (2011) used to explore the effects of the inner jets on the morphology of the surrounding nebula translate well to this work. We do not, however, model a precessing jet like in Goodall et al. (2011) but instead launch the jet along a fixed axis, which we expect for reasons outlined at the beginning of this section.

Supernova explosion

To model the initial natal supernova explosion, we simulate a Sedov-Taylor (Sedov 1958, Taylor 1950) spherical blast wave at the centre of the simulation volume. This Sedov expansion is a standard approximation of a

supernova explosion once the swept up mass exceeds the initial supernova ejecta mass, immediately following the initial kinetic 'free-expansion' phase during which the ejecta moves at a constant ejection velocity and expands more quickly than the subsequent Sedov phase. The properties of the emitting gas in the supernova remnant are consistent with a type IIP supernova explosion with progenitor mass ranging from ~ 8 to $\sim 25 M_{\odot}$ (Chevalier 2005), and thus we make a conservative estimate of about $5 M_{\odot}$ of ejected mass. With this mass, the radius at which the Sedov phase of expansion begins is ~ 3.6 pc for a spherical explosion. The current radius of Cir X-1 at 9.4 kpc is roughly 8 pc across and thus is likely currently in the Sedov phase, and was only dominated by the free-expansion phase for the first several hundred years of its evolution, a fraction of this simulation time. Simulating the free-expansion phase would accelerate the growth of the supernova, as it is more rapid in this phase, and would produce a more realistic mass distribution, but would require a much higher resolution simulation that is beyond the scope of this investigation.

To simulate the supernova explosion, we initiate a sphere with pressure

$$p_{\rm SN} = \frac{(\gamma - 1) E_{\rm SN}}{V} \tag{5.3}$$

where $E_{\rm SN} = 3.0 \times 10^{50}$ ergs, we assume a non-relativistic adiabatic index $\gamma = 5/3$, and V is the volume of the initial explosion which we set to be spherical with radius $R_{\rm SN} = 3$ simulation pixels, equivalent to 9×10^{16}cm ($\sim$0.03 pc). Inside the explosion radius, we set the density to be equal to the ambient density.

ISM and Galactic density profile

Outside of the explosion radius, the pressure is set as

$$p_0 = \frac{c_{s,0}^2 \rho_0}{\gamma} \tag{5.4}$$

where the sound speed in the ambient medium is $c_{s,0} = 9 \times 10^5 \mathrm{cm\,s^{-1}}$, the density is set at $\rho_0 = 1.673 \times 10^{-24} \mathrm{g\,cm^{-3}}$, equivalent to $n_0 = 1\,\mathrm{cm^{-3}}$ for a fluid of protons. This pressure is constant everywhere outside of the explosion radius to ensure stability in the surrounding ISM.

The density in the surrounding ISM is not constant, however, as Cir X-1 sits very close to the Galactic plane and therefore likely sits in a region of high density gradient (again, much like its counterpart SS433). To simulate this, we again adopt methods from Goodall et al. (2011) and employ an exponential density profile of the Galactic plane as described by Dehnen and Binney (1998), adopted for the position of Cir X-1 with respect to the galactic plane and normalized such that the number density at the centre of the simulation (the position of the XRB) is unity. We measure the position of Cir X-1 relative to the Galactic centre as $R_{\star} = 5.8$ kpc and $z_{\star} = 6.15$ pc. The jet axis, which we infer to be aligned with the bubbles on either side of the nebula, is perpendicular to the galactic plane, an advantageous feature as it therefore allows us to maintain an axisymmetric geometry in our simulation. Lastly, we inject random Gaussian perturbations in the surrounding ISM of the scale 10^{-4}.

Jet injection

The jet in this simulation is launched after the initial supernova explosion from the centre of the simulation volume and explosion epicentre. We inject the jet as a relativistic flow through a nozzle which is set as an internal boundary, meaning the cells which inject the jet are not evolved according to the fluid equations along

with the rest of the grid. Symmetric jets are injected along the z-axis in the positive and negative direction. The jet nozzle spans 3 pixels in the x-direction and 1 pixel in the z-direction, and therefore the injection radius is 9×10^{16}cm – this being the smallest area for a numerically stable jet, although we note that this is much larger than the orbital separation of the binary system $\sim 10^{12}$cm (Tauris et al. 1999). We set the pressure in the jet as $7.5 \times 10^{-10}\,\mathrm{g\,cm^{-1}\,s^{-2}}$, such that the jet is hot with respect to the ISM, but depending on the pressure within the supernova at the time that the jet is launched, is at times slightly cooler than its surrounding fluid. Jet pressure is kept constant in all simulations as an independent variable.

The main goal of the simulation is to reproduce the morphology of the jet-nebula interaction. As such, we choose to only vary the parameters of the jet, as we assume that this has the largest influence on the resultant morphology, and they are currently poorly understood. The main jet parameters we vary are:

$P_{\rm jet}$: the jet power, mainly through varying the jet Lorentz factor Γ, although in some simulations we test two jet densities $\rho_{\rm jet}$

$t_{\rm jet}$: the jet initial launch time, measured in years since supernova

$\Delta t_{\rm jet}$: the jet injection duration, which contributes to the total injected energy $E_{\rm jet}$

These all have a significant effect on the final morphology of the jet-nebula interaction site, and varying these allows us to understand how certain morphological features of Cir X-1 may have arisen.

5.4.3 Simulation analysis

To compare the simulation directly with the radio data presented here in this work, we estimate a pseudo-emissivity from the simulation data which serves to replicate optically thin synchrotron emission following the prescription outlined by Hardcastle and Krause (2013). Based on the assumption of minimum energy, where there is equipartition between the energy in magnetic fields and electrons, the comoving[1] synchrotron emissivity can be expressed as

$$j'_{\nu'} = A(p, \nu', \gamma, \eta)(\kappa P)^{(p+5)/4} \tag{5.5}$$

where P is the pressure in the simulation, p is the spectral index, $A(p, \nu', \gamma_{1,2}, \eta)$ is the constant prefactor for all simulation cells (see Hardcastle and Krause 2013) which depends on the spectral index, the comoving observing frequency ν', the minimum and maxium Lorentz factors of the electron distribution $\gamma_1 = 10$ and $\gamma_2 = 10^5$, and $\eta = 0.75$ is the partitioning factor between energy in the magnetic fields and electrons. This is related to Equation 5.1 used to calculate the minimum energy from the observed emission, but includes an extra term κ. This term provides a simplistic treatment for particle acceleration, delegating how much of the internal pressure is stored in relativistic electrons and magnetic fields. We set $\kappa = 0.1$, which roughly translates to a particle acceleration efficiency of $\sim 5\%$. This is a reasonable estimate, as we know roughly 10% of shock power from supernova remnants is thought to be funnelled into cosmic ray acceleration (Bell 2013, Helder et al. 2009, Morlino et al. 2013).

The emissivity in Equation 5.5 is a comoving quantity, and relativistic effects should be incorporated when

[1] we denote all comoving quantities with the prime $'$ notation.

Table 5.1: *Jet parameter values adopted in test simulations. A non-comprehensive number of permutations were tested.*

Parameter	Values	Description
$\Gamma_{\rm jet}$:	3, 5, 7, 10	Lorentz factor of the jet
$n_{\rm jet}$:	7.7×10^{-5} , 10^{-6}	Jet density ($\rm cm^{-3}$)
$\Delta t_{\rm jet}$:	500, 550, 800, 1000, 1500	Jet duration (years)
$t_{\rm jet}$:	50, 100, 400, 1000, 2000, 2500, 3000	Jet initial launch time (years)

calculating the flux in the frame of the observer. This flux is given as

$$F_\nu = \frac{\delta^{2-\alpha}}{d_L^2} \int j'_\nu dV \tag{5.6}$$

where V is the lab-frame volume[1] over which the emission is integrated, α (defined as p in Equation 5.5) is the spectral index. While we measure a global spectral index of $\alpha \sim -0.5$ (Section 5.3.2), this is affected by optically thicker pockets. Since we are interested in simulating the optically thin emission, we adopt a spectral index of $\alpha = -1$, which is representative of this emission in the shell (Fig. 6.5). d_L Is the distance to the source, and $\nu = 1.28$GHz is the lab-frame observing frequency. The Doppler factor δ is given as

$$\delta = \Gamma^{-1}(1 - \beta \cos\theta)^{-1} \tag{5.7}$$

where θ is the angle of the velocity vector to the line of sight, β is the speed of the fluid in units of c, and Γ is the Lorentz factor.

We note that when calculating the minimum energy of the nebula and bubbles from the radio data in Section 5.1 we do not make any relativistic corrections. This is predominantly because we do not know the velocities present in the system and therefore can not correct for them, and secondly, as we infer and discuss later given the simulation results, we deem it unlikely that there is a presently active jet producing the bubbles and therefore the Lorentz factor of the observed fluid today is likely not relativistic.

Lastly, if we assume that the emission is optically thin, we are able to make maps of the integrated emission across the 3D volume. To do this, we rotate the 2D cylindrical simulation frames about their z-axis and interpolate them onto a 3D Cartesian grid. This data is then integrated along the line of sight using an in-house the ray-tracing algorithm `DART` to produce images which we then use to compare to the real radio image.

5.5 Simulation Results

We ran several test simulations, varying jet power and duty cycle within a confined parameter space, in order to gauge how the jet-nebula morphology changes as a result. These simulations non-comprehensively spanned the parameters listed in Table 5.1. Although we did not test all permutations, simulations were run in batches with control and independent variables, after which several test simulations of interest were pursued. As a result of this process, we present a fiducial simulation, presented in Figures 5.5, 5.6 and 5.7, which is best able to reproduce the features observed in the radio image Figure 5.2. The fiducial simulation parameters are shown in Table 5.2, as well as the parameters for two select comparison simulations which we present in Figure 5.7.

[1]the `PLUTO` code returns primitive variables (in the comoving frame) but the grid is defined in the lab frame, hence why we integrate over the lab frame volume.

Table 5.2: *Simulation parameters of the fiducial simulation, as well as two select comparison simulations which we present in Figure 5.7.*

Simulation name	$\Gamma_{\rm jet}$	$\Delta t_{\rm jet}$	$t_{\rm jet}$	$n_{\rm jet}$
Fiducial simulation	7	550 years	50 years	7.7×10^{-5} cm^{-3}
Increase $t_{\rm jet}$	7	800 years	2500 years	7.7×10^{-5} cm^{-3}
Increase $\Delta t_{\rm jet}$	7	1500 years	50 years	7.7×10^{-5} cm^{-3}

5.5.1 A fiducial simulation

We are successfully able to reproduce a supernova remnant of the correct size within the age estimate, along with a set of inflated bubbles along the jet axis. The formation of these bubbles, due to the interaction between the jet and the supernova remnant, can be seen clearly in Figure 5.5.

The supernova nebula in the simulation prior to the jet launching is initially spherical. At 50 years, the jet is launched, and shortly after we begin to see protrusions on either side of the nebula where the jet has propagated past the supernova shock radius. While the jet is still on (see panels at 182, 397, and 555 years in Figure 5.5) the jet produces a pointed, conical feature as it drives into the ISM. At this time, these features are in rough pressure equilibrium with the nebula. After the jet turns off at 600 years, the jet is no longer driving the bubble features into the ISM and instead they begin to expand and cool – this results in the previously conical bubbles becoming more rounded at their tip and expanding outwards (see, in particular, the progression from 555-1190 years along the middle row in Figure 5.5). We also begin the see the bubbles become cooler than the inner nebula over this time. The bubbles continue to expand adiabatically, as well as with the supernova explosion itself, and the base of the bubble where the jet had essentially punched a hole into the remnant widens with the expansion of the supernova, resulting in the flattened morphology of the bubble we see at the end of the simulation.

This fiducial simulation presents a scenario where a powerful jet, approximately $\sim 35 L_{\rm Edd}$ for a $1.4 M_{\odot}$ neutron star, is launched early in the evolution of the supernova over a relatively short amount of time. This is consistent with the fact that we do not observe any other features evidencing a recently active powerful jet. Additionally, we observe what seems to be a slower precessing jet unimpeded by any other faster jet activity, such that the slow jet must be launched after the fast jet (or at the very least along another axis).

In addition to the simulated jet producing a pair of bubbles, matching those observed in the data, we are also able to reproduce several other key features present in the radio image. Here, we compare the ray-traced flux as seen in Figure 5.6 with the Cir X-1 radio image.

Firstly, the region where the inflated radio bubbles meet the edge of the supernova remnant in Cir X-1 is slightly enhanced in brightness, producing a ring-shaped base to the bubble – we also reproduce this in the fiducial simulation. Secondly, the tip of the radio bubble is slightly brighter compared to the rest of the bubble which is uniformly illuminated, which we also observe in the simulation, most apparent in the emissivity map of the fiducial simulation in the central panel of Figure 5.7. Lastly, in the radio image, the bubble itself has a strikingly smooth and round shape, especially in contrast to the complex structure seen inside of the supernova remnant. This smooth shape in the bubble is reproduced in the fiducial simulations, although we do not see the same amount of structure in the nebula itself (this is likely due to our simplistic treatment of the supernova explosion, although we do see some structure appear in other simulations which we discuss further in Section 5.5.2).

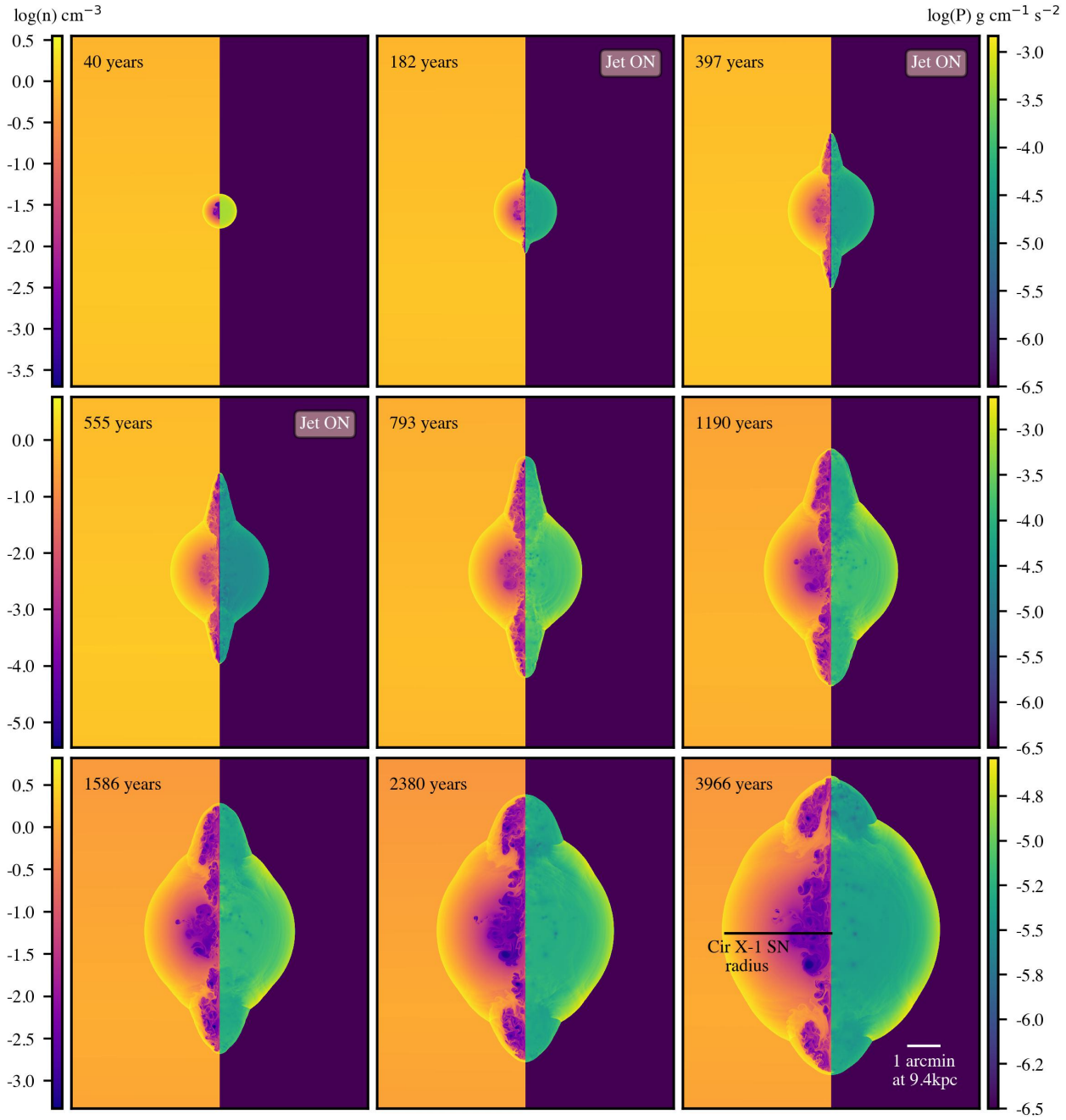

Figure 5.5: *Various timesteps of the fiducial simulation, with the time elapsed since initial supernova indicated in the top-left. Each panel shows the log of the number density on the left-hand side, and the log of the pressure on the right. Each row shares the same colourbar axes on the left (number density; lower densities assigned darkest colours, e.g. purple) and right (pressure; lower pressures assigned darkest colours, e.g. blue and purple) of the row. In the final timestep, we indicate the measured radius of the Cir X-1 supernova remnant as well as the angular scale of the simulation at the same distance as Cir X-1. We indicate in the top-right corner of each panel if the jet is active during that timestep, where the jet is launched between 50-600 years in this simulation.*

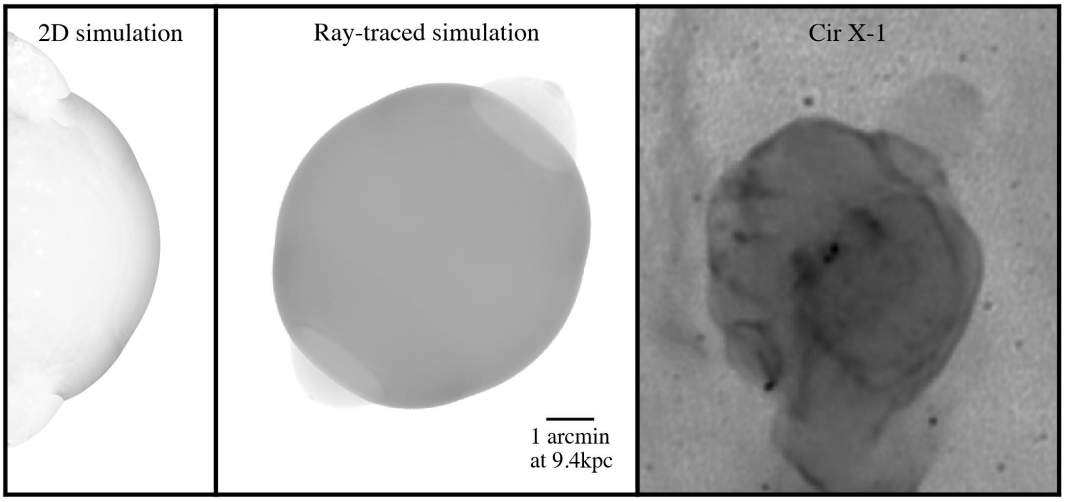

Figure 5.6: *Lab-frame flux of the fiducial simulation compared to the observed radio flux. The 2D axisymmetric simulation (left) is rotated about its axis and the emissivity is integrated along a 60° angle to the line of sight using the in-house ray-tracing software* `DART` *to produce the optically thin flux image (centre). We compare this morphology to the real radio image of Cir X-1 (right). Flux is displayed in log-space, the colour scales of the images are individually and arbitrarily scaled for visual comparison, and the length scales are equal in all panels. We indicate in the central panel the angular scale of the simulation at the same distance as Cir X-1, which also spatially corresponds to 1 arcminute in the real radio image on the right.*

5.5.2 Relations between jet parameters and radio features

With the fiducial simulation we show as a proof of concept a plausible scenario for the formation of these bubbles. However, there are certain features in the radio image which are not reproduced well in the fiducial simulation, but are present in other test simulations (although at the expense of other key features). By running these test simulations, we are able to broadly infer which jet parameters are responsible for various features and in general make statements about how these jets affect their natal supernovae.
Here we enumerate radio features present in the data which we have aimed to reproduce in simulations, and qualitatively discuss how the jet parameters affect the emergence of these features.

Size and brightness of the bubble rings. The ring formed by the intersection of the bubble and the supernova remnant is a prominent feature for both bubbles (NW and SE) in the radio image – the ring is not only slightly brighter than the adjacent emission from the nebula, it is also narrow, in that it occupies a relatively small surface area of the nebula. Comparing the radio image to the fiducial simulation, the rings in the simulation are wider and are slightly less edge-brightened.
Addressing the size of the ring, this is mainly because the jet in the simulation is launched relatively early in the evolution of the supernova. A hole is punched by the jet into the edge of the expanding supernova remnant shortly after launch, as seen in Figure 5.5. As the remnant expands, the puncture also expands with it, producing a wide-radius ring at the end of the simulation evolution. The rings produced by jets launched at late times are narrower, but produce much smaller bubbles for the same power jet, see the left panel in Figure 5.7. These late-launch simulations also show marginally more edge-brightening, but we found this varied inconsistently across simulations and likely relies on more complex interplay between the jet/nebula hydrodynamics.

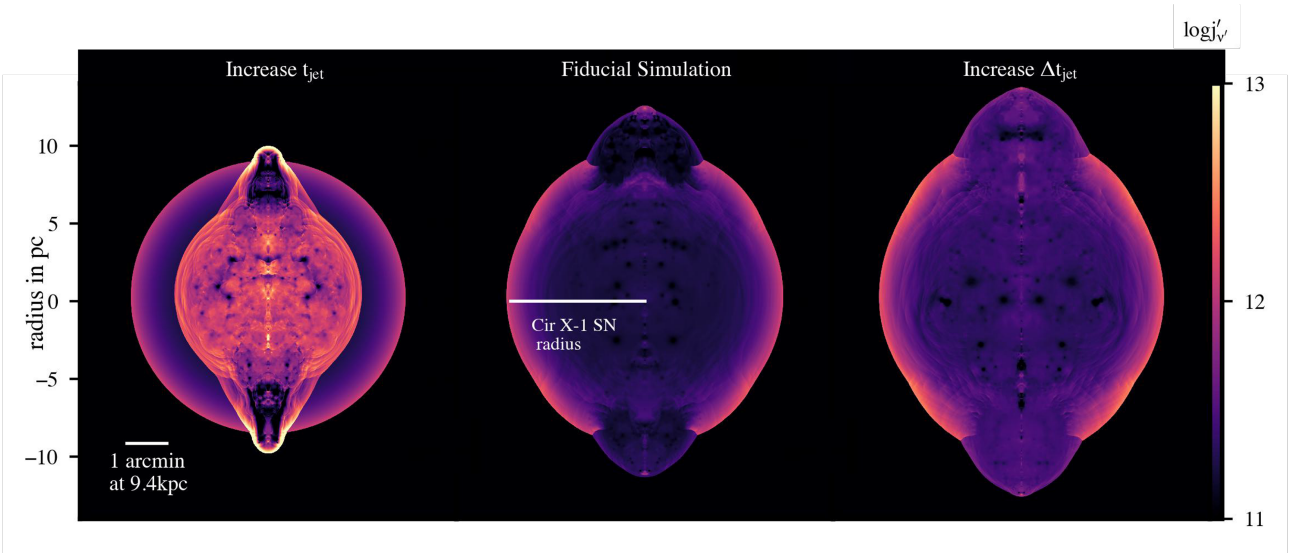

Figure 5.7: *Comparison between the fiducial simulation (centre), a simulation where the jet is launched later in time and for slightly longer (left), and the same simulation but the jet is launched for a longer period of time (right) but starts at the same time as the fiducial. Each simulation is shown at 3966 years old. We indicate the measured radius of the Cir X-1 supernova remnant for comparison, as well as the angular scale of the simulation at the same distance as Cir X-1. Each map is showing the log of the comoving emissivity $j'_{\nu'}$ per pixel. The scale on the left of the image is the radius of the bubble with respect to the centre of the supernova in parsecs. Simulation parameters are specified in Table 5.2.*

Height and shape of the bubble. One of the most striking features of the Cir X-1 bubbles is how prominent the northern bubble is: its height along the axis of the jet is almost equal to the radius of the nebula itself (∼80% of radius). In addition to this, the bubble appears to be widest at halfway between the nebula puncture and its tip, giving it the distinctive 'bubble-like' appearance. We were unable to produce a simulation within our explored parameter space with this 'bubble-like' shape, and all bubbles produced were instead widest at their base. Recently active jets (as seen at t=55 and 793 years in Figure 5.5) produce bubbles which are triangular in shape, and after the jet is turned off the bubbles expand adiabatically to produce more rounded structures. This suggests that the jets in Cir X-1 have been switched off, or at least operating at substantially lower power, for enough time for this expansion to have taken place, as we do not observe a triangular morphology in the radio image. We also note that the jet requires less power to puncture the expanding supernova shell and produce a bubble of sufficient height when launched early, as opposed to late. However, even with a jet power equivalent to $\sim 35 L_{\rm Edd}$ launched only 50 years after supernova (as adopted in the fiducial simulation, at the very high end of what we would expect regarding jet power from a NS), the bubble produced is still too short. Jets which were sustained for a longer $\Delta t_{\rm jet}$ produced bubbles which were taller, but also slightly wider at their base and overall less rounded, as evident in the right panel of Figure 5.7.

Bubble asymmetry. Another remarkable feature of the radio bubbles observed in Cir X-1 is their apparent asymmetry. To reproduce this asymmetry, we include a model of the galactic density profile in some of our tests. This profile results in the southern bubble growing in a denser local environment compared to the northern bubble, resulting in a reduced size and a flatter profile in the southern bubble. However, the extent to which they are asymmetric is not reproduced, and the simple galactic profile is not sufficient to explain the observed asymmetry.

Ratio of bubble and supernova remnant flux density. Although Cir X-1 is relatively well studied, the bubbles were not detected until now due to their low surface brightness. This feature, although somewhat frustrating for earlier observers, is particularly telling of their history. In simulations, the bubbles are bright compared to the expanding nebula when formed, in particular the tip of the bubble which is the working surface of the jet. Only after hundreds of years of cooling do they reach such low surface brightness. We see this in Figure 5.7 between the fiducial simulation and the simulation on the right launched over a longer $\Delta t_{\rm jet}$, where the latter has not had enough time to cool. This adds to the mounting evidence that the jets were launched early in the history of the remnant. Additionally a longer cooling time limits the total energy injected by the jet into the bubble and therefore implies a shorter $\Delta t_{\rm jet}$.

Features inside the supernova remnant. The emissivity inside of the nebula in the fiducial simulation is very uniform due to the smooth pressure profile of the Sedov-Taylor expansion, and the absence of internal shocks from the jet injection. This is not the case, however, for simulations where the jet is launched later in the supernova evolution, see an example in the left panel of Figure 5.7. In these simulations, the interior of the supernova has cooled and the sound speed has decreased, enabling the jet to inflate a cocoon of reheated material which produces a secondary shock within the nebula itself. This secondary shock propagates outwards and fills the space inside the nebula, creating a turbulent spherical structure brighter than the outer remnant. In the radio images, we could interpret some of the inner structure to be of similar morphology, and possibly be caused by jet activity. However, supernova remnants without jet activity have inherently complex turbulent internal structures, and it is likely that a more realistic treatment of the supernova explosion could also produce structures akin to those seen in Cir X-1.

5.6 Discussion / Summary

The jets of Cir X-1 have been identified through radio imaging over the past decades (Calvelo et al. 2012, Coriat et al. 2019, Fender et al. 1998, Moin et al. 2011, Stewart et al. 1993, Tudose et al. 2006). In Stewart et al. (1993) & Tudose et al. (2006) the emissivity and curved structures of the jets are detailed, while Coriat et al. (2019) further revealed additional features in the nebula. Our deep MeerKAT L band image shows these features in much greater detail, such as the rings and bright lines in the southern tip and shell structures. In this work, we make note of new structures in the nebula, such as the diffuse jet-punched bubbles protruding from the position of the rings. These bubbles are positioned in line with the jets of the system. To understand the morphology and physical mechanisms responsible in the object, the spectral index maps were determined and the formation of the bubbles simulated.

5.6.1 The spectral index and how it compares to the simulation results

At the position of the binary system the core is steep with a spectral index around -0.8 in Fig. 6.5 and light pink-purple in Fig. 5.8. The core along with the shock fronts of the jet also have the least error according to the spectral index error map (right panel of Fig. 6.5). The spectral index appears to steepen as one moves from the core to the rest of the nebula (shell). The region between the core and the shock fronts are optically thin, thus emitting synchrotron radiation, indicating loss of energy and deceleration of the electrons. Once the particles/electrons are confronted by the shock front, some distance away from the core, they experience a surge

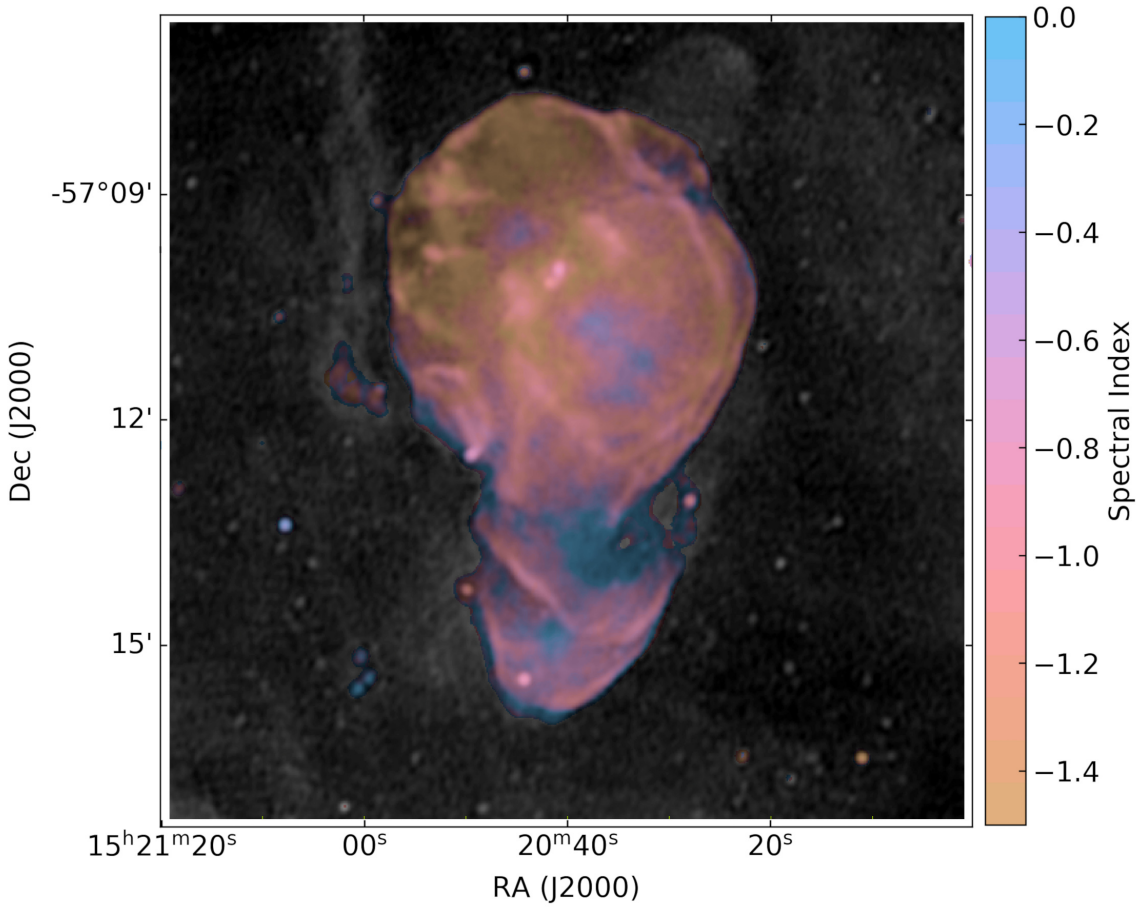

Figure 5.8: *Combined Spectral Index and Intensity. The spectral index was mapped with colours that have the same value (see equilumance mapping at https://github.com/mlarichardson/CosmosCanvas.) This map was blended with a greyscale rendition of intensity using the multiplication mode in GIMP.*

of energy as they move through the currently observed jets. The shock fronts and the jets therefore appear to have a similar spectral index that is slightly steeper than the core as seen in Fig. 5.8 in pink. These features remain identifiable as flatter than the space around them, which is gold in Fig. 5.8. Perpendicular to the jets, are much flatter regions with a spectral index more positive than -0.8, blues in Fig. 5.8. The SW 'pocket' is larger and the spectral index is flatter as the shell in its entirety appears to flatten from the north eastern end to the south western end. A portion of the NW ring at the edge of the nebula has a spectral index more positive than -0.8 (around -0.1 Fig. 6.5), indicating a flatter region compared to the core whereas the SE ring has a spectral index similar to the core. The error in the NW ring spectral index is also quite significant compared to the error of the SE ring. Therefore, the SE ring may be more indicative of the actual spectral index at the rings.

In the fiducial simulation, once the fast fixed-axis jets turn off and no longer drive the bubbles, it is seen that the bubbles are cooler than the inner nebula. This cooler nature, along with the low surface brightness and density of the bubbles may be the reason there is no spectral index measurement of the bubbles. The simulation evidence of the fast fixed-axis jets being launched early on, during the supernova explosion, and having since turned off (with only the slow less-powerful precessing jets remaining), is consistent with the steep spectral index observed in the radio image over the majority of the nebula (shell). Although the simulations suggest the fast fixed-axis jets being off and there are no longer active jets, regular outbursts could feed into slower precessing jets. This is supported by the spectral index being slightly flatter for the shock fronts and the slower precessing jets compared to the region of space between the core and the jets/shock-fronts. Furthermore, the simulations (both fiducial and others) reproduce the bright rings observed in the radio image and the bright features (rings, core) consistently show a flatter spectral index compared to the shell of the nebula outside the pockets. For the rings, this may be due to the interaction when the jets punched at the edge of the supernova remnant and subsequent ISM interaction.

5.6.2 The minimum energy

The integrated energy of the jet over its lifetime is 1.1×10^{50}erg, much higher than the minimum energy of 4×10^{45}erg inferred from the NW bubble in the radio image. In addition, the initial simulated supernova energy is 3×10^{50} erg, also much higher than the inferred 2×10^{47} erg minimum energy of the nebula. This is somewhat expected, as both the remnant and bubbles have had time to cool since the energy was injected in the simulation. However, we might expect that the ratio of energies would be the same between the energy injected in the simulation and the minimum energy inferred from the radio image, which currently differ by about a factor of 10.

We choose not to directly compare the integrated flux of the simulated ray-traced image to the observed radio image, but instead compare the ratio of the supernova nebula flux to the bubble flux, which we believe to be a more reliable comparison as it is less dependent on scaling freedoms in the flux calculation and assuming that the supernova flux is reliable. We are able to reproduce this contrast, meaning that the discrepancy between the injected and inferred energies comes from either the jet energy being lost at a faster rate than the supernova energy, or the jet emission partially contributing to the nebula flux. In Figure 5.7, jets launched early (fiducial and 'increase $\Delta t_{\rm jet}$' simulations) slightly over-inflate the supernova nebula in the north and south compared to the late-launched jet ('increase $t_{\rm jet}$' simulation). This could be due to some of the jet energy being dissipated within the nebula itself at early times, thus requiring a larger jet energy to reproduce the nebula-bubble flux ratio. At late times, this energy is still dissipated inside of the nebula but instead inflates a hot inner cocoon

as seen in Figure 5.7, independent from the outer supernova shock, whereas the jet is able to inflate the nebula itself when launched early.

Overall, by reproducing the flux contrast between the nebula and bubble, we are showing that adiabatic cooling, in addition to the jet energy redistributing into the inner nebula, is sufficient to explain the discrepancy between the calculated minimum energy and the jet injected energy.

5.6.3 Jet properties: considerations and caveats

The fiducial simulation presented in this work which best reproduces our observations implies the existence of a powerful jet launched early in the evolution of the SN. The power of the jet in the simulation is $\sim 35 L_{\rm edd}$, which is particularly high for a typical NS XRB. However, it has been speculated that SS433, albeit a BH XRB, is a hyper-Eddington ultra-luminous X-ray source which appears comparatively faint due to inclination and collimation (Begelman et al. 2006). We can therefore postulate that perhaps Cir X-1 is a less evolved sibling of SS433 and is showing analogous super-Eddington behaviour. However, we caution that the exact jet power implemented in the simulation is not a 'fit' to data, so to speak, and the results simply indicate that a high jet power ($\sim$tens of $L_{\rm edd}$) is a plausible explanation for the radio morphology.

There are also several effects which we have not incorporated in this simulation. Most obviously, although we assume the presence of magnetic fields through synchrotron radiation, we do not invoke them in the simulation. It is possible that large-scale magnetic fields both in the jet itself and the SN nebula could affect the morphology and growth of the bubbles, notably their confinement at the base of the bubble.

In addition, the galactic density profile which we incorporate is a basic model and does not account for local inhomogeneities in the field which, as apparent in our wide-field image (Figure 5.1), are complex and abundant. These local density fluctuations, in particular a possible underdense region to the North of the nebula and/or an overdense region south to the south, could explain the observed asymmetry in the bubbles.

Lastly, we have only explored one formation scenario: a 'two-mode' jet model where a fast fixed-axis jet is launched in contrast to the present-day slow precessing jet. Although we find that this seems to explain much of our observations, we can not rule out all other jet histories. For example, one possibility is that jet activity before or during the SN explosion could be responsible for the morphology, perhaps from a gamma-ray burst (GRB). However, a GRB jet seems unlikely to explain the observed morphology. We require that the jet remains collimated to large scales in order to produce the bubble height, whereas GRBs are estimated to only remain collimated up until maximally the Sedov length ($\sim 10^{17}$ cm), and in reality are likely to undergo lateral spreading much earlier than this (Duffell and Laskar 2018, Granot and Piran 2012, Matthews et al. 2025). Indeed, in the simulations of Zhang and MacFadyen (2009) it is estimated that only after 150 years of evolution the outflow is almost spherical with a radius already about half the size of the final supernova nebula. We note that Shishkin et al. (2024) and Soker and Shishkin (2025) have explored the possibility of bubble formation in other SNRs through alternative jittering jet SN mechanisms.

5.7 Conclusions

We produced a deep-field radio image of Cir X-1 using data acquired with the MeerKAT telescope. The image was constructed with a stack of 30 epochs (a total of 7.5 hrs) such that two full outburst cycles of Cir X-1 were included. The deep radio image revealed a never before seen set of asymmetric jet-punched bubbles. Illustrating a breakout of the jets at the edge of the supernova remnant, similarly seen in the older source, SS433

with supernova remnant W50. We investigate the physical nature of the object from the observational results and simulate the morphological structure to determine the influence of the jets in producing what we observe. We determine that the spectral index map suggests the jets and remnant are largely optically thin. We measure the spectral index of the core presents as slightly flatter than the jets due to the outbursting activity and the 'pocket' areas perpendicular to the jets are even flatter (with slightly larger error in these regions compared to the core and shock front/jets combination).

We ran relativistic hydrodynamic simulations of a simplistic supernova explosion, after which we injected a fixed-axis jet which interacts with the expanding SN shell, and explored jet parameters to try to match the observed radio morphology.

Our results suggest that a powerful jet was launched within the first hundred years post-supernova, and that this jet was particularly powerful, on the order of tens of $L_{\rm Edd}$. We can also conclude that the jet was likely short-lived and constant in power, with respect to the timescales of the remnant evolution. We unable to reproduce two main features: the height of the bubble and the narrowness of the base of the bubble i.e. the ring. The bubble height could likely be increased by a locally under-dense region at the north of the nebula, also providing the extra asymmetry that we observe in the radio image. This kind of low-density region could be a natural result of the complex density field found in the galactic plane.
The narrowness of the ring observed was not reproduced by any test simulation – this could be due to limitations of the simulation setup itself. Due to the range of scales involved in the system, the width of the jet (although only a few pixels across) is much larger than the width of the binary system and this could potentially contribute to a larger puncture in the nebula at early times, but we did not test this and thus the effects are unknown.

Overall, we are able to reconstruct a simplified morphology of Cir X-1 with an early-launched powerful fast fixed-axis jet which produced energies as high as 10^{50} erg. This modeling indicates that the MeerKAT observations are the first to reveal an initial breakout of neutron star jets from their natal supernova remnant, and further support the scenario in which Cir X-1 is a younger relation of the archetypal jet source SS433. The detail of the internal structure of the nebula may be investigated in future works. Additionally, the improved telescope facilities like the new MeerKAT S-band (1.75 – 3.5 GHz) allows for analysis into the jets of the system and their precession (Cowie et al. 2025, in prep) which may help explain the detailed features within the nebula.

Acknowledgements

KVSG acknowledges the University of Cape Town, the National Research Foundation Phd scholarship and the Department of Science and Innovation SAWISA Doctoral Fellowship. KS acknowledges support from the Clarendon Scholarship Program at the University of Oxford and the Lester B. Pearson Studentship at St John's College, Oxford. JHM acknowledges funding from a Royal Society University Research Fellowship (URF\R1\221062).

The authors would like to acknowledge Fernando Camilo for helping name the Africa nebula and Wenfei Yu for the valuable discussion in improving the paper.

We gratefully acknowledge the use of the following software packages: PLUTO (Mignone et al. 2007b), matplotlib (Hunter 2007), and astropy:[1] (Astropy Collaboration et al. 2013, 2018, 2022).

The authors would like to acknowledge the use of the University of Oxford Advanced Research Computing (ARC) facility in carrying out the simulation work (`http://dx.doi.org/10.5281/zenodo.22558`).

The MeerKAT telescope is operated by the South African Radio Astronomy Observatory, which is a facility of

[1] `http://www.astropy.org`

the National Research Foundation, an agency of the Department of Science and Innovation. We acknowledge the use of the ilifu cloud computing facility – www.ilifu.ac.za, a partnership between the University of Cape Town, the University of the Western Cape, Stellenbosch University, Sol Plaatje University and the Cape Peninsula University of Technology. The ilifu facility is supported by contributions from the Inter-University Institute for Data Intensive Astronomy (IDIA – a partnership between the University of Cape Town, the University of Pretoria and the University of the Western Cape), the Computational Biology division at UCT and the Data Intensive Research Initiative of South Africa (DIRISA).

This work made use of the CARTA (Cube Analysis and Rendering Tool for Astronomy) software (Comrie et al. (2021) - DOI 10.5281/zenodo.3377984 – `https://cartavis.github.io`).

Data Availability

The data availability will be subject to the ThunderKAT LSP data release conditions.

Chapter 6

Extended results

6.1 Results extended

In the following section I report on results obtained from the research project that were not included in the papers listed in Chapters (3, 4 and 5) and will form part of future publications. The monitoring of Circinus X-1 in the radio is one of the projects that includes further analysis of the lightcurves and images in addition of what is reported in Chapter 5. Cygnus X-2 is a long term multiwavelength monitoring programme and the latest results and analysis are be reported below.

6.1.1 Cir X-1 timeseries results

Cir X-1 was observed with MeerKAT at 1.28 GHz (L-band) for 34 consecutive days as part of a high-cadence monitoring project. The observations occurred daily such that two full outburst cycles were recorded. The primary calibrator (flux, bandpass) and the secondary (phase) calibrator used were J1939-6342 and J1424-4913, respectively. The data were reduced using OXKAT with detailed steps described in Chapter (Papers). Simultaneous X-ray data was taken with Swift during the MeerKAT monitoring campaign using the Windowed Timing (WT) mode and Photon Counting (PC) mode (Burrows et al. 2005).

Figure. 6.1 displays the lightcurves of Cir X-1 in the radio band as well as the X-rays observed by Swift, MeerKAT and MAXI. The timeline extends from when the source was first observed with MeerKAT in 2021 until the end of the monitoring from the high-cadence campaign. The first panel shows Swift X-ray data in the 1–10 keV energy band, the second panel 1.28 Ghz MeerKAT radio data and the third panel MAXI X-ray data in the 2–20 keV energy band. The rise and fall of two outbursts appear to be correlated closely between radio and X-ray. While the first 4 radio detections showed the source is bright in the radio, the full outburst monitoring revealed that the brightness of the source can reach near 4 mJy/beam.

The source was placed on the radio : X-ray correlation shown in Fig. 6.2, a flat spectral index is assumed, therefore, the radio flux was scaled to 5 GHz and the luminosity was determined using the distance of 9.4 kpc (Heinz et al. 2015). The cyan stars on the correlation plane represent the MeerKAT-MAXI matches which are within a day of quasi-simultaneity (Fig. 6.2). The source is shown here to lie among the Z-sources, complementing the Z-source nature of Cir X-1. It is also among the XTE J1701 region, the only other X-ray binary to have

a transitional Z- Atoll source property. Following these results, further analysis investigating the day-to-day jet variability will be performed. This will be done through producing subtraction images, where each epoch is subtracted from the deep (summed) image.

6.1.2 MeerKAT observations of the Z-sources

A radio imaging campaign to observe the full set of Z-sources was conducted with MeerKAT. The five Z-sources; Cyg X-2, GX 13+1, GX 340+0, GX 349+2 and GX 17+2 (excluded Sco X-1 since it had previously been observed as part of a different campaign), were observed in April 2022 for 15 minutes each at 1.28 GHz. This defines a complete report of the Z-sources with MeerKAT, providing a homogeneous report in the radio. The sources Cyg X-2 (3.68 ± 0.12 mJy/beam), GX 17+2 (0.46 ± 0.041 mJy/beam) and GX 349+2 (0.16 ± 0.022 mJy/beam) were all detected and the other sources were not detected (see Table. 6.1). Cyg X-2 was subsequently monitored with AMI in April 2022 at 15 GHz, after the MeerKAT detection. The LA configuration and the calibrator J2134+4050 was used. Initially, the observations were performed at a cadence of ± 5 days, which was subsequently increased to ± 2 days to potentially observe more flares. Fig. 6.3 shows the variability of the source since the monitoring began in April 2022, and the blue lightcurve represents the automatically generated lightcurve of the source. Three flares have been observed since the observations began with the flux densities of 2.88 mJy/beam, 3.46 mJy/beam and 3.61 mJy/beam for the first(59752.16), second (59843.90) and third (60135.13) flare peak respectively, which do not reveal a clear pattern. However, the long term monitoring is ongoing with the prospect of analysing the flares more closely. The correlation between the hard X-rays and the jet emission on the HB of the source is an interesting feature to explore (Farinelli et al. 2023). Therefore, future analysis may also include determining the radio – X-ray correlation for this source.

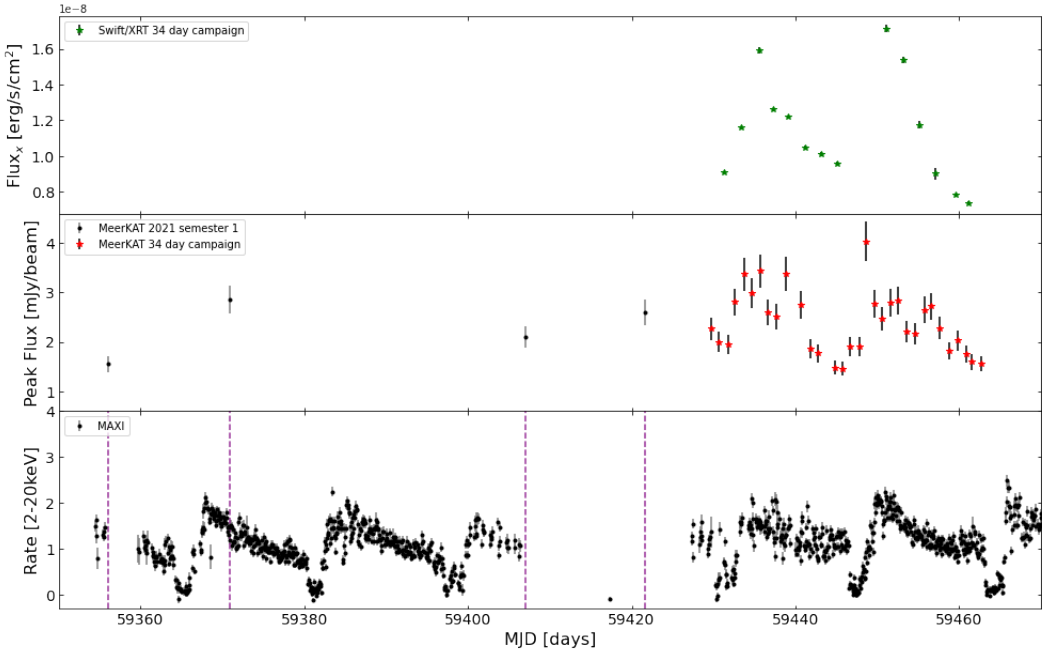

Figure 6.1: *The Cir X-1 lightcurve in the X-ray from Swift (top panel) and MAXI (bottom panel) and the radio peak flux density (middle panel) taken over the 2021 large-high cadence monitoring campaign with MeerKAT.*

Table 6.1: *The MeerKAT radio flux detections and 3σ upper limits of the observed Z-sources at 1.28 GHz*

Target	Flux [mJy/beam]
Cyg X-2	3.68 ± 0.12
GX 13+1	$<$ 0.31
GX 340+0	$<$ 0.22
GX 349+2	0.16 ± 0.022
GX 17+2	0.46 ± 0.041

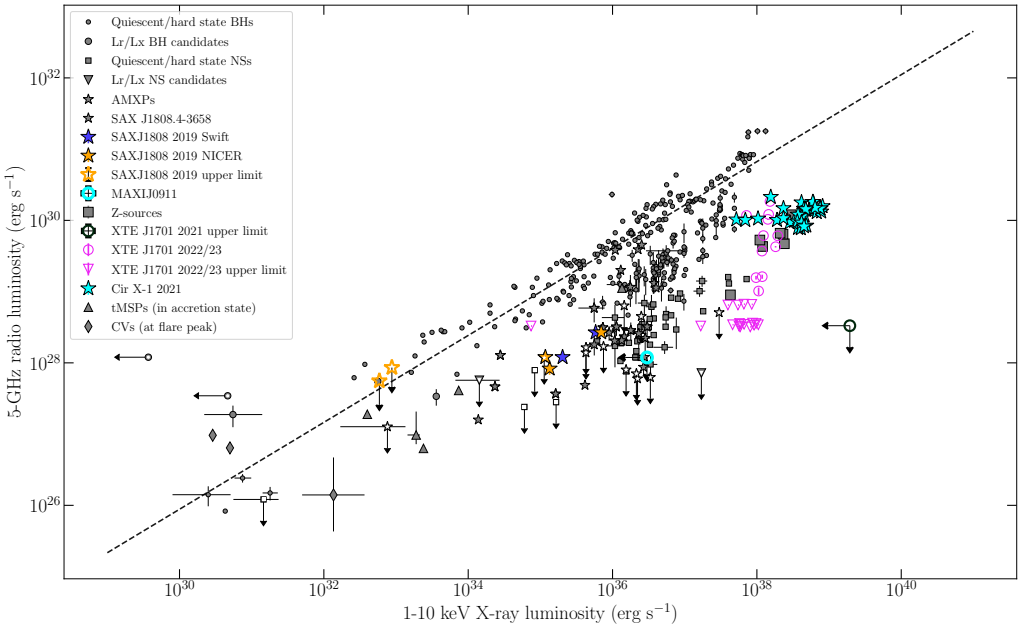

Figure 6.2: *The radio X-ray correlation plane where Cir X-1 is highlighted in the cyan stars, representing the radio and X-ray luminosities from the 2021 high cadence monitoring campaign between the MeerKAT and MAXI matches. The rest of the sources in this research sample are highlighted in orange,blue and pink.*

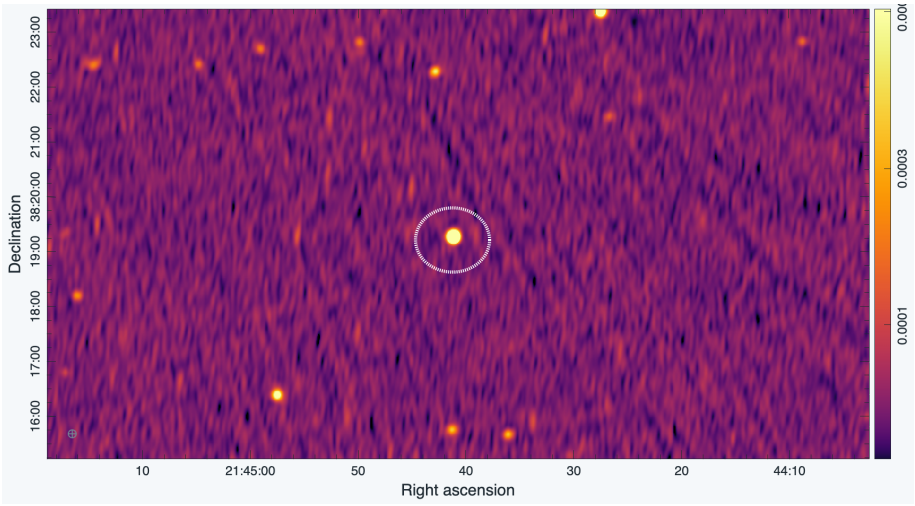

Figure 6.4: *The radio image of Cyg X-2 taken with MeerKAT, the source is detected at 3.68 ± 0.12 mJy/beam*

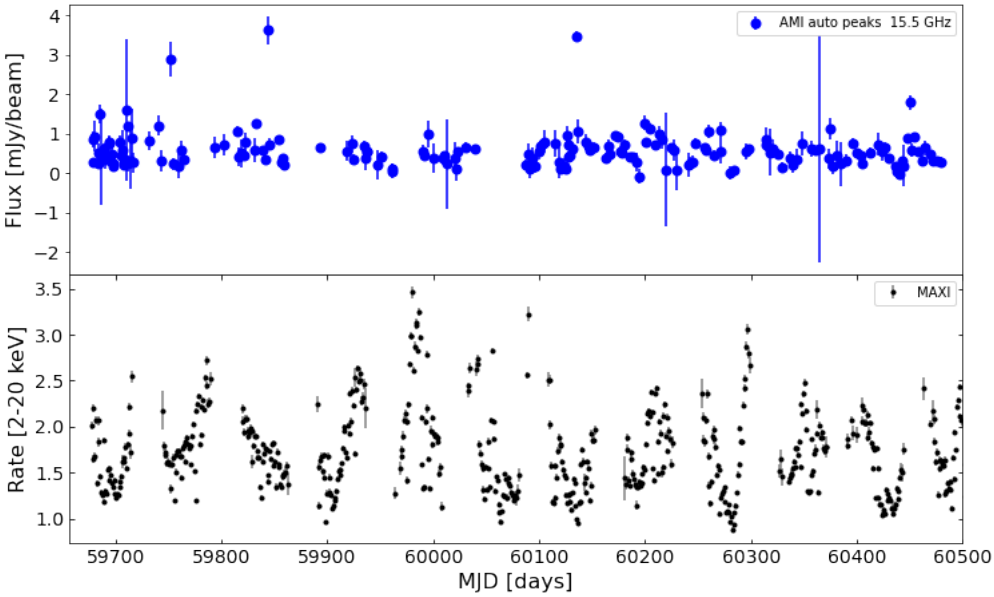

Figure 6.3: *The long-term radio monitoring lightcurve of Cyg X-2 is shown in the top panel of the figure above. We have observed 3 radio flares at a level > 3 mJy/beam over a monitoring period of about 2 years. The X-ray MAXI lightcurve is compared in the bottom panel taken over the same period the source was observed with AMI.*

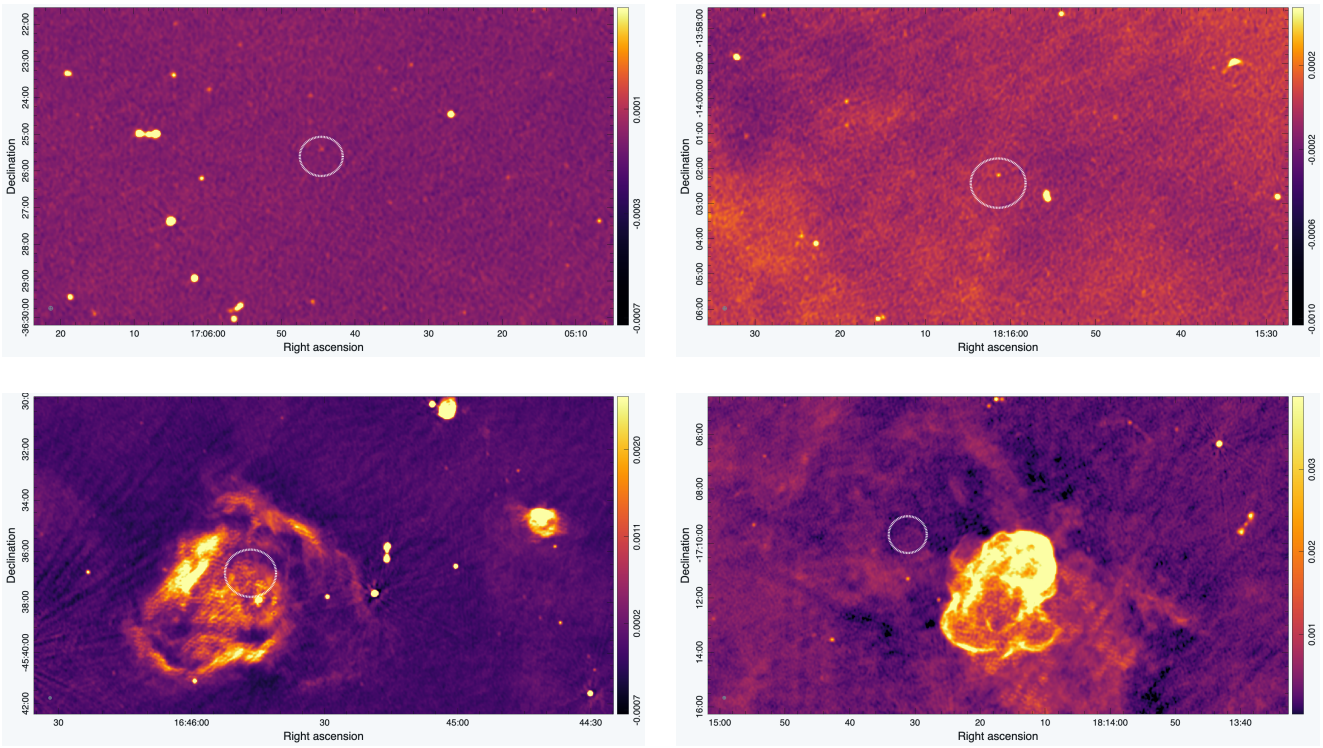

Figure 6.5: *The MeerKAT radio images of the Z-sources. Top left is GX 349+2 detected at 0.16 ± 0.022 mJy/beam. Top right: GX 17+2 is detected at 0.46 ± 0.041 mJy/beam. Bottom left: GX 340+0 is undetected at 3 sigma upper limit 0.22 mJy/beam and bottom right: GX 13+1 is undetected at 3 sigma upper limit 0.31 mJy/beam.*

Chapter 7

Discussion and Conclusion

In the following chapter, the results and analysis outputs of this study are discussed. An interpretation of the results is provided and what it means for jet production in NSXBs. Additionally, the results of NSXBs are compared to BHXBs.

7.1 The radio X-ray correlation of NSXBs

To place the sources on the radio – X-ray plane, there are quasi-simultaneous (Δt < 3 days) observations matched between radio and X-ray luminosities. The spectral index was assumed to be flat for the sources (even XTE J1701 which is shown to vary in Paper 2) to maintain homogeneity. Since all the radio luminosities are from the MeerKAT telescope (1.28 GHz), the flux densities were scaled to 5 GHz for consistency throughout the plane. A best fit for each source was determined using the PYTHON module, LINEAR REGRESSION, in the SKLEARN library. Two slopes were determined for SAX J1808 since *NICER* and *Swift* X-ray luminosities were used. In contrast, XTE J1701 and Cir X-1 each had one slope from the MAXI X-ray luminosities (the quasi-simultaneous *Swift* luminosities are a future work project for Cir X-1). All the slopes were produced from the detection matches and although the upper limits were excluded they remain consistent.

SAX J1808 best fit slopes were $\beta_{SAXJ1808-S}$=0.77 ± 0.13 and $\beta_{SAXJ1808-N}$=0.67 ± 0.33 for *Swift* and *NICER* respectively. XTE J1701 has a slope of $\beta_{XTEJ1701}$= 0.82 ± 2.4.

Table 7.1: *The radio – X-ray correlation slopes β_{source} for the sources (SAX J1808, XTE J1701 and Cir X-1) in our research sample*

Source	radio – X-ray correlation slope
$\beta_{SAXJ1808-Swift}$	0.77 ± 0.13
$\beta_{SAXJ1808-NICER}$	0.67 ± 0.33
$\beta_{XTEJ1701}$	0.82 ± 2.4
β_{CirX-1}	0.11 ± 0.14

The radio – X-ray correlation determined for SAX J1808 was based on the source being in the hard spectral state and the other sources in the sample are assumed to have been in softer spectral state during the observations. Therefore, SAX J1808 is the only source in the sample to truly compare to the BH $L_R : L_X$ correlation. The slope for this source is vastly different to those determined for the NSXBs 4U 1728-34 ($\beta_{4U1728-34} = 1.40 \pm 0.25$

Migliari and Fender 2006) and Aql X-1 ($\beta_{AqlX-1} = 1.38 \pm 0.23$ Migliari and Fender 2006, $1.17^{+0.30}_{-0.21}$ Gusinskaia et al. 2020), in fact it resembles the $\beta_{BH} \sim 0.7$ for BHXBs more. It can be argued that while the radiative efficiency of accretion is assumed to be different for the types of BH and NS XRB systems, our result shows there must be (in some cases) a similarity in the accretion and jet power coupling between the systems.

Migliari and Fender (2006) compare the NS and BH XRBs, concluding that the similarities are; (1) when in the hard spectral state, below luminosities ($L_X < 0.1 \times L_{Edd}$) both types of systems have steady and self absorbed jets observed to show a $L_R : L_X$ relation, (2) at higher luminosities and $L_X \sim L_{Edd}$ there are bright optically thin transient events like the rapid flares discussed in Section. 5.1.

The limitations in our study is that we were only able to definitively compare one of our sources to the BHXB correlation due to the spectral state of the simultaneous radio and X-ray observations. Since the correlation slopes of NSXBs in the soft state cannot be compared to the correlation of BHXBs, a larger sample of systems is required to learn more. Additionally and more generally, a higher cadence in observations will be useful to overcome any sample biases. Moreover, a higher observational cadence will improve the ability to define the spectral states and the changes thereof. Interesting aspects of accretion for BHXBs could be revealed with a large study because the physical nature of the compact object may not be the only contributing factor affecting the accretion. Furthermore, the increased presence of jet power in the soft state NSXBs may reveal a little about the production of the more suppressed jets in BHXBs when they also in the soft state. There is a proposal for an anti correlation of the radio and X-ray where in this case the radio is the jet and the boundary layer is the X-ray. As the jet strengthens the corona heats up and conversely. Marino et al. (2023) suggest that the emitted radiation from the boundary layer drives the evolution of the jet so that the jet switches on when the boundary layer switches off. To learn more about the presence of the jet power, the following section discusses both the X-ray and radio flaring and reflaring events during the outbursts.

7.2 The flaring nature of the research sample

Transient sources like X-ray binaries have varying outburst durations and recurrence times. The sources in my research sample have outbursts recurrence ranging from months to years while one source is more persistent and does not experience quiescence.

The 2019 outburst of SAX J1808 is observed to be active for about a month in the radio and a little over a month in the X-ray band. The radio lightcurve displays a main outburst and rebrightening event considered as a reflare (MJD: 58705.81 – 58726.79) during which the jet brightens. The occurrence of an X-ray reflare after the main radio outburst is also observed in previous X-ray outbursts of the source (Baglio et al. 2020, Patruno et al. 2016). The optical lightcurve from Paper 1 (also seen in Baglio et al. 2020) appears to present multiple brightenings during this reflaring phase. However, the quantity of these events are difficult to state definitively due to the short variability at the optical flux. On the other hand, XTE J1701 has an active radio period spanning over four months (MJD: 59838.72 – 59939.31). During this period, three distinct flares are observed in the radio lightcurve. In the X-ray lightcurve a similar flaring nature is observed to occur and align closely with the radio flare peaks (see red dashed lines in Figure. 1 of Paper 2).

We propose that the amount of flaring seen in the lightcurves of objects depends on the sampling of data

and cadence of observations. Observing objects at high cadence is particularly important for systems like Z-sources that encounter physical (X-ray) changes on the timescales of hours to days. In XTE J1701 we see an increased amount of radio flaring from one outburst to the next (2006/7 to the 2022/23 one) and we suspect this is as a result of the improved sampling. Moreover, due to the daily cadence in X-ray observations with MAXI from the first recorded outbursts to the latest outburst, an increase in X-ray flaring is not observed.

In Figure. 6.1 two outbursts are observed in the radio for Cir X-1, although there is variability within each outburst, flaring cannot be definitively identified from the lightcurve. Overall, the improved sampling in our objects (weekly cadence, in the case of SAX J1808 and XTE J1701 and daily cadence in the case of Cir X-1) has allowed for some flaring to be observed. However, due to the Z-source nature of some of the sources (where Z-source variability is see on timescales of hours to days) it is plausible to conclude there might be a greater amount of flaring that was not captured. The energy produced during the flaring events are typically larger in BHXBs compared to NSXBs. The minimum energies are investigated using the peak flux densities of the flares and the following section discusses in detail the methods used for the determining these minimum energies.

7.3 Minimum energy of NS jets

The minimum energy produced can be determined using the peak flux densities of each flare. If the size of the emitting regions is not directly measurable from the radio image, the region size can be inferred using the following relation: $R_{\rm min} = \beta_{\rm m} c \Delta t$ where, $\beta_{\rm m}$ is Equation 28 in Fender and Bright 2019

$$\beta_m = 5.6 \times 10^1 D_{\rm kpc}^{\frac{16}{17}} F_{\nu,{\rm mJy}}^{\frac{8}{17}} \nu_{\rm GHz}^{\frac{-33}{34}} \Delta t_{\rm sec}^{-1}$$

c is the speed of light and Δt is the duration of the flare, D is the distance to the object, F the flux density and ν the frequency at which the object is observed.
The minimum energy produced during a flare is given by Equation 29 of Fender and Bright (2019),

$$E_m = 1.5 \times 10^{35} D_{\rm kpc}^{\frac{40}{17}} F_{\nu,{\rm mJy}}^{\frac{20}{17}} \nu_{\rm GHz}^{\frac{-23}{34}}$$

For XTE J1701 the values for the first, second and third flares are: $E_{\rm min} = 1 \times 10^{38}$ erg, $E_{\rm min} = 6 \times 10^{37}$ erg and $E_{\rm min} = 5 \times 10^{37}$ erg, respectively.

We assume these quantities are due to a poorer radio sampling than required to observe a truer estimate for a source like this (NSXB), and therefore these are lower limits on the total kinetic (jet) energy output. Improved sampling is especially critical for Z sources or sources that mimic Z-source behaviour with rapid flares and variability ranging on timescales of hours to days. Fender et al. (2023) notes that poor sampling in the radio band may result in a number of short-lived flares blending and resulting in an incorrect estimate of the complete output kinetic energy by more than an order of magnitude.

When the size of the emitting region may be derived through direct measurement like the bubble in Cir X-1, the minimum energy is determined in the following manner; Diameter = distance*angular size for a distance of 9.4,/kpc, assuming a spherical body we determine the volume of the emitting region and source size. Therefore

using the flux density calculate the total radiative luminosity

$$L = 4\pi D^2 F_{\nu_2} \nu_2^{-\alpha} \left(\frac{\nu_2^{\alpha+1} - \nu_2^{\alpha+1}}{\alpha + 1} \right)$$

using the above luminosity the minimum energy becomes

$$E_{min} = 0.92 \eta^{\frac{4}{7}} c_{12}^{\frac{4}{7}} f^{\frac{3}{7}} R^{\frac{9}{7}} L^{\frac{4}{7}}$$

The source size measured for the bubble is $r_{lobe} = 7.09 \times 10^{18}$ cm and for the nebula labeled 'the bulb' is $r_{nebula} = 2.46 \times 10^{19}$ cm such that E_{min} becomes $E_{min-lobe} = 4 \times 10^{45}$ erg for the bubble and $E_{min-nebula} = 2 \times 10^{47}$ erg bulb. The energy produced by the simulations discussed in Paper 3, determine the initial energy of the supernova to be $E = 3 \times 10^{50}$ erg and the energy required from the jets to produce the features of the nebula as $E = 1.1 \times 10^{50}$ erg. The energy estimates show that larger energies are required to produce the bubble and nebula features, therefore, the energies we measure from the radio image are likely due to the jet switching off.

We note that the daily radio observation cadence for Cir X-1 contributed to capturing as much of the rapid flares compared to XTE J1701 which had poorer sampling. We also note that the single short flares like those in XTE J1701 can lead to the larger structures seen in Cir X-1 produced by 1000s of years of jet activity.

7.4 Conclusion

The aim of this research study was to determine a comprehensive analysis of the accretion of NSXBs and more extensively the jets of these systems. This comprised observing and analysing a sample of NSXBs in the X-ray and the radio bands. This was accomplished as part of the ThunderKAT Large survey project, largely making use of the MeerKAT radio telescope with inclusions from the AMI telescope. The X-ray telescopes used were *Swift* (in collaboration with ThunderKAT), *NICER* and MAXI missions. The lightcurves of the sources in the research sample were analysed and with the aim of investigating a correlation between the X-ray and radio for each source, the observations were quasi-simultaneous.

The lightcurves of sources revealed flaring events (more definitively in SAX J1808 and XTE J1701). It is discuss that as the peaks of the flares are approached, the source becomes increasingly optically thin. XTE J1701 has a changing spectral index observed throughout the outburst using the 8 in-band spectral indices from MeerKAT. However, when determining the radio – X-ray correlation for our sources a flat spectral index was assumed of all of them to maintain homogeneity among the objects on the correlation plane. The correlation for each source is determined using the slope β determined from the best fit model. SAX J1808 has a slope $\beta_{SAXJ1808-S}$=0.77 ± 0.13 and $\beta_{SAXJ1808-N}$=0.67 ± 0.33 for *Swift* and *NICER* respectively. XTE J1701 has a slope $\beta_{XTEJ1701}$= 0.82 ± 2.4. Although the large uncertainty for XTE J1701 makes it difficult to compare to the other sources, we note that our results (for SAX J1808 and XTE J1701) reveal a closer link between the radiative efficiencies of NS and BH XRBs. For Cir X-1 the radio image was analysed, revealing a never before seen nebula structure we label 'bubble' (a result of the jet punching through the nebula). To investigate the structures of the nebula and the jets of Cir X-1 more closely, a hydrodynamic simulation was run to mimic the features of the object. We are able to model the basic structure of the object using a simple supernova explosion and determine that the jet must have been launched within the first hundred years of the supernova explosion.

Together, these forms of analysis reveal that the sources that have large structures like those seen in Cir X-1 require powerful jets and the jet activity in the other sources create multiple short lived flares. Furthermore, NSXBs are able to maintain a relationship between the jet production and the accretion activity that may be similar to the relationship observed for BHXBs.

Since the radio X-ray correlation results for our NSXB sample have nearly parallel slopes to the BHXB slope, similarly to what has been observed in Migliari and Fender (2006) and Gallo et al. (2018), it suggests accretion flow dynamics need to be re-evaluated for NSXBs. This result impacts the field of X-ray binaries greatly because it interrogates the widely accepted physics of accretion onto a NS and the affects thereof. Whether the accretions results from strong winds, the spinning of the NS or magnetic fields interactions. Therefore suggesting there is a lot to consider about the relationship between the jet activity and the accretion flow for NSXBs.

Unfortunately due to the compact jets in NSXBs not being as bright as the BH counterparts, it limits the extent of detections, measured brightness and resolvability. The current telescopes like MeerKAT have improved the odds dramatically but better is still required. Continuing from the homogeneity of this study with regards to the radio telescope used, will further strengthen the impact of future studies in this field. Such that the hard spectral states of NSXBs are comparable to BHXBs, but the soft state of NSXBs as well (since the radio outflows are also present during NSXB soft states).

7.4.1 Future work

To truly understand and perform an improved comparative study of NS vs BH XRB jets, a larger research sample is required with observations performed at a high cadence to investigate the flaring activity more closely. The aim of the future work is increase the sample with NS sources and further populate the radio – X-ray correlation plane with these systems. The first task is to complete the long-term monitoring of Cyg X-2 and investigate the nature of its outbursts. Analyses of Cir X-1 will continue beyond this Phd project, introducing more investigative aspects of the jets in the object. This includes analysing the time-series of the object through the lightcurve and short-term variability of the jets (by comparing the day to day radio images of the object).

Appendix A

Tables

Table A.1: *The MeerKAT radio flux at 1.28 GHz, MAXI X-ray flux in the 4 - 10 keV band and Swift/XRT X-ray flux in the 1 - 10 keV band for Cir X-1.*

MDJ	F_r [mJy]	$F_{MAXI} \times 10^{-8}$ [erg/s/cm^2]	$F_{Swift} \times 10^{-8}$ [erg/s/cm^2]
59429.45833		3.84 ± 0.41	
59429.65103	2.27 ± 0.38		
59430.53111		0.98 ± 0.41	
59430.63284	2 ± 0.26		
59431.32402			$0.91^{+0.0078}_{-0.0079}$
59431.46889		0.49 ± 0.25	
59431.75889	1.94 ± 0.032		
59432.5		2.21 ± 0.41	
59432.6034	2.8 ± 0.12		
59433.344		5.72 ± 0.57	
59433.38095			$1.16^{+0.0077}_{-0.014}$
59433.76307	3.37 ± 0.026		
59434.63822	2.99 ± 0.11		
59434.75		7.69 ± 0.49	
59435.5		5.64 ± 0.49	
59435.56221			$1.59^{+0.016}_{-0.017}$
59435.70051	3.43 ± 0.041		
59436.5		4.99 ± 0.41	
59436.59024	2.6 ± 0.2		
59437.2872			1.26±0.010
59437.5		7.36 ± 0.65	
59437.62767	2.51 ± 0.11		
59438.46846		3.93 ± 0.65	
59438.82691	3.37 ± 0.02		
59439.14068			1.22±0.0096
59440.43714		4.25 ± 0.41	

Table A.1: *The MeerKAT radio flux taken at 1.28 GHz, MAXI X-ray flux in the 4 - 10 keV band and Swift/XRT X-ray flux in the 1 - 10 keV band for Cir X-1 (continued).*

59440.63901	2.75 ± 0.1		
59441.12889			$1.05^{+0.0082}_{-0.0083}$
59441.4375		3.11 ± 0.33	
59441.84281	1.86 ± 0.33		
59442.43923		2.7 ± 0.33	
59442.7421	1.77 ± 0.03		
59443.13375			1.01±0.010
59444.44923		3.52 ± 0.33	
59444.76293	1.48 ± 0.064		
59445.05736			0.096±0.012
59445.47733		3.84 ± 0.41	
59445.74083	1.46 ± 0.12		
59446.51067		1.8 ± 0.25	
59446.59044	1.91 ± 0.17		
59447.5		0.65 ± 0.25	
59447.86135	1.91 ± 0.26		
59448.51067		1.47 ± 0.25	
59448.55823	4.03 ± 0.023		
59449.5		7.2 ± 0.49	
59449.66837	2.76 ± 0.017		
59451.02818			1.28 ± 0.18
59450.51467		6.38 ± 0.41	
59450.56158	2.47 ± 0.069		
59451.5		7.11 ± 0.49	
59451.59994	2.79 ± 0.026		
59452.48643		6.05 ± 0.41	
59452.55634	2.84 ± 0.08		
59453.15109			1.71±0.020
59453.55956	2.2 ± 0.039		
59453.59385		4.33 ± 0.41	
59454.51867		4.01 ± 0.41	
59454.59706	2.17 ± 0.15		
59455.06431			1.54±0.019
59455.5		4.5 ± 0.41	
59455.71695	2.65 ± 0.017		
59456.52267		4.5 ± 0.41	
59456.58249	2.72 ± 0.045		
59457.06499			$1.17^{+0.021}_{-0.022}$
59457.5		3.52 ± 0.33	
59457.57375	2.27 ± 0.09		
59458.52733		3.48 ± 0.33	

Table A.1: *The MeerKAT radio flux taken at 1.28 GHz, MAXI X-ray flux in the 4 - 10 keV band and Swift/XRT X-ray flux in the 1 - 10 keV band for Cir X-1 (continued).*

59458.71827	1.82 ± 0.041		
59459.46867		2.21 ± 0.33	
59459.57749			$0.90^{+0.031}_{-0.033}$
59459.85521	2.03 ± 0.1		
59460.52714		3.93 ± 0.41	
59460.8046	1.76 ± 0.22		
59461.04764			$0.78^{+0.0096}_{-0.0097}$
59461.498		4.58 ± 0.74	
59461.54082	1.59 ± 0.072		
59462.52692			0.74±0.01
59462.65603	1.56 ± 0.03	4.25 ± 0.41	

Appendix B

Keywords and Acronyms

B.1 Keywords

Transient
X-ray binary
Black hole
Neutron star
Accretion disk
Jet
Radio (continuum)

B.2 Abbreviations & Acronyms

- Accreting millisecond pulsar (AMXP)
- Active galactic nucleus (AGN)
- All Sky Monitors (ASMs)
- Arcminute Microkelvin Imager (AMI)
- Australia Telescope Compact Array (ATCA)
- Black Hole (BH)
- Blandford–Payne (BP)
- Blandford–Znajek (BZ)
- Burst Alert Telescope (BAT)
- Cataclysmic variables (CV)
- Centre for High Performance Computing (CHPC)

- Charge-Coupled Device (CCD)
- Colour-colour diagram (CD)
- Disk instability model (DIM)
- Field of view (FOV)
- Flaring branch (FB)
- Focal Plane Camera Assembly (FPCA)
- Gamma-ray burst (GRB)
- Gas slit camera (GS)
- Hardness intensity diagram (HID)
- Harten–Lax–van Leer contact (HLLC)
- High mass X-ray binary (HMXRB)
- Horizontal branch (HB)
- Inner most stable circular orbit (ISCO)
- Institute for Data Intensive Astronomy (IDIA)
- Intermediate state (IS)
- International Space Station (ISS)
- Interstellar medium (ISM)
- Island state (I)
- Long array (LA)
- LOw Frequency ARray (LOFAR)
- Low mass X-ray binary (LMXB)
- Lower banana (LB)
- Massachusetts Institute of Technology (MIT)
- MeerKAT Large Survey Projects (MLSPs)
- Millisecond Pulsar (MSP)
- Modified Julian Date (MJD)
- Monitor of All-sky X-ray Image (MAXI)
- Neutron star (NS)
- Neutron star Interior Composition ExploreR (NICER)

- Normal branch (NB)
- North WEST (NW)
- Neutron star X-ray binary (NSXB)
- Photon Counting (PC)
- Poynting-Robertson cosmic battery (PRCB)
- Quasi-periodic oscillations (QPOs)
- Relativistic hydrodynamic (RHD)
- Rossi X-ray Timing Explorer (RXTE)
- Small array (SA)
- Solid-state slit camera (SSC),
- South African Radio Astronomy Observatory (SARAO)
- South East (SE)
- Spectral energy distribution (SED)
- Square Kilometre Array (SKA)
- Supernova (SN)
- Telescope Alignment mirror (TAM)
- Thermoelectric cooler (TEC)
- Total variation diminishing (TVD)
- Very high state (VHS)
- Very Long Baseline Interferometry (VLBI)
- Ultravoilet/Optical Telescope (UVOT)
- Upper banana (UB)
- Windowed Timing (WT)
- X-ray binary (XRB)
- X-ray Telescope (XRT)

Bibliography

M. A. Alpar, A. F. Cheng, M. A. Ruderman, and J. Shaham. A new class of radio pulsars. Nature, 300(5894): 728–730, December 1982. doi: 10.1038/300728a0.

F. Ambrosino, A. Miraval Zanon, A. Papitto, F. Coti Zelati, S. Campana, P. D'Avanzo, L. Stella, T. Di Salvo, L. Burderi, P. Casella, A. Sanna, D. de Martino, M. Cadelano, A. Ghedina, F. Leone, F. Meddi, P. Cretaro, M. C. Baglio, E. Poretti, R. P. Mignani, D. F. Torres, G. L. Israel, M. Cecconi, D. M. Russell, M. D. Gonzalez Gomez, A. L. Riverol Rodriguez, H. Perez Ventura, M. Hernandez Diaz, J. J. San Juan, D. M. Bramich, and F. Lewis. Optical and ultraviolet pulsed emission from an accreting millisecond pulsar. *Nature Astronomy*, 5:552–559, January 2021. doi: 10.1038/s41550-021-01308-0.

R. P. Armstrong, R. P. Fender, G. D. Nicolson, S. Ratcliffe, M. Linares, J. Horrell, L. Richter, M. P. E. Schurch, M. Coriat, P. Woudt, J. Jonas, R. Booth, and B. Fanaroff. A return to strong radio flaring by Circinus X-1 observed with the Karoo Array Telescope test array KAT-7. MNRAS, 433(3):1951–1957, August 2013. doi: 10.1093/mnras/stt860.

K. A. Arnaud. XSPEC: The First Ten Years. In George H. Jacoby and Jeannette Barnes, editors, *Astronomical Data Analysis Software and Systems V*, volume 101 of *Astronomical Society of the Pacific Conference Series*, page 17, January 1996.

Astropy Collaboration, T. P. Robitaille, E. J. Tollerud, P. Greenfield, M. Droettboom, E. Bray, T. Aldcroft, M. Davis, A. Ginsburg, A. M. Price-Whelan, W. E. Kerzendorf, A. Conley, N. Crighton, K. Barbary, D. Muna, H. Ferguson, F. Grollier, M. M. Parikh, P. H. Nair, H. M. Unther, C. Deil, J. Woillez, S. Conseil, R. Kramer, J. E. H. Turner, L. Singer, R. Fox, B. A. Weaver, V. Zabalza, Z. I. Edwards, K. Azalee Bostroem, D. J. Burke, A. R. Casey, S. M. Crawford, N. Dencheva, J. Ely, T. Jenness, K. Labrie, P. L. Lim, F. Pierfederici, A. Pontzen, A. Ptak, B. Refsdal, M. Servillat, and O. Streicher. Astropy: A community Python package for astronomy. A&A, 558:A33, October 2013. doi: 10.1051/0004-6361/201322068.

Astropy Collaboration, A. M. Price-Whelan, B. M. Sipőcz, H. M. Günther, P. L. Lim, S. M. Crawford, S. Conseil, D. L. Shupe, M. W. Craig, N. Dencheva, A. Ginsburg, J. T. Vand erPlas, L. D. Bradley, D. Pérez-Suárez, M. de Val-Borro, T. L. Aldcroft, K. L. Cruz, T. P. Robitaille, E. J. Tollerud, C. Ardelean, T. Babej, Y. P. Bach, M. Bachetti, A. V. Bakanov, S. P. Bamford, G. Barentsen, P. Barmby, A. Baumbach, K. L. Berry, F. Biscani, M. Boquien, K. A. Bostroem, L. G. Bouma, G. B. Brammer, E. M. Bray, H. Breytenbach, H. Buddelmeijer, D. J. Burke, G. Calderone, J. L. Cano Rodríguez, M. Cara, J. V. M. Cardoso, S. Cheedella, Y. Copin, L. Corrales, D. Crichton, D. D'Avella, C. Deil, É. Depagne, J. P. Dietrich, A. Donath, M. Droettboom, N. Earl, T. Erben, S. Fabbro, L. A. Ferreira, T. Finethy, R. T. Fox, L. H. Garrison, S. L. J. Gibbons, D. A. Goldstein, R. Gommers, J. P. Greco, P. Greenfield, A. M. Groener, F. Grollier, A. Hagen, P. Hirst, D. Homeier,

A. J. Horton, G. Hosseinzadeh, L. Hu, J. S. Hunkeler, Ž. Ivezić, A. Jain, T. Jenness, G. Kanarek, S. Kendrew, N. S. Kern, W. E. Kerzendorf, A. Khvalko, J. King, D. Kirkby, A. M. Kulkarni, A. Kumar, A. Lee, D. Lenz, S. P. Littlefair, Z. Ma, D. M. Macleod, M. Mastropietro, C. McCully, S. Montagnac, B. M. Morris, M. Mueller, S. J. Mumford, D. Muna, N. A. Murphy, S. Nelson, G. H. Nguyen, J. P. Ninan, M. Nöthe, S. Ogaz, S. Oh, J. K. Parejko, N. Parley, S. Pascual, R. Patil, A. A. Patil, A. L. Plunkett, J. X. Prochaska, T. Rastogi, V. Reddy Janga, J. Sabater, P. Sakurikar, M. Seifert, L. E. Sherbert, H. Sherwood-Taylor, A. Y. Shih, J. Sick, M. T. Silbiger, S. Singanamalla, L. P. Singer, P. H. Sladen, K. A. Sooley, S. Sornarajah, O. Streicher, P. Teuben, S. W. Thomas, G. R. Tremblay, J. E. H. Turner, V. Terrón, M. H. van Kerkwijk, A. de la Vega, L. L. Watkins, B. A. Weaver, J. B. Whitmore, J. Woillez, V. Zabalza, and Astropy Contributors. The Astropy Project: Building an Open-science Project and Status of the v2.0 Core Package. AJ, 156(3):123, September 2018. doi: 10.3847/1538-3881/aabc4f.

Astropy Collaboration, Adrian M. Price-Whelan, Pey Lian Lim, Nicholas Earl, Nathaniel Starkman, Larry Bradley, David L. Shupe, Aarya A. Patil, Lia Corrales, C. E. Brasseur, Maximilian N"othe, Axel Donath, Erik Tollerud, Brett M. Morris, Adam Ginsburg, Eero Vaher, Benjamin A. Weaver, James Tocknell, William Jamieson, Marten H. van Kerkwijk, Thomas P. Robitaille, Bruce Merry, Matteo Bachetti, H. Moritz G"unther, Thomas L. Aldcroft, Jaime A. Alvarado-Montes, Anne M. Archibald, Attila B'odi, Shreyas Bapat, Geert Barentsen, Juanjo Baz'an, Manish Biswas, M'ed'eric Boquien, D. J. Burke, Daria Cara, Mihai Cara, Kyle E. Conroy, Simon Conseil, Matthew W. Craig, Robert M. Cross, Kelle L. Cruz, Francesco D'Eugenio, Nadia Dencheva, Hadrien A. R. Devillepoix, J"org P. Dietrich, Arthur Davis Eigenbrot, Thomas Erben, Leonardo Ferreira, Daniel Foreman-Mackey, Ryan Fox, Nabil Freij, Suyog Garg, Robel Geda, Lauren Glattly, Yash Gondhalekar, Karl D. Gordon, David Grant, Perry Greenfield, Austen M. Groener, Steve Guest, Sebastian Gurovich, Rasmus Handberg, Akeem Hart, Zac Hatfield-Dodds, Derek Homeier, Griffin Hosseinzadeh, Tim Jenness, Craig K. Jones, Prajwel Joseph, J. Bryce Kalmbach, Emir Karamehmetoglu, Mikolaj Kaluszy'nski, Michael S. P. Kelley, Nicholas Kern, Wolfgang E. Kerzendorf, Eric W. Koch, Shankar Kulumani, Antony Lee, Chun Ly, Zhiyuan Ma, Conor MacBride, Jakob M. Maljaars, Demitri Muna, N. A. Murphy, Henrik Norman, Richard O'Steen, Kyle A. Oman, Camilla Pacifici, Sergio Pascual, J. Pascual-Granado, Rohit R. Patil, Gabriel I. Perren, Timothy E. Pickering, Tanuj Rastogi, Benjamin R. Roulston, Daniel F. Ryan, Eli S. Rykoff, Jose Sabater, Parikshit Sakurikar, Jes'us Salgado, Aniket Sanghi, Nicholas Saunders, Volodymyr Savchenko, Ludwig Schwardt, Michael Seifert-Eckert, Albert Y. Shih, Anany Shrey Jain, Gyanendra Shukla, Jonathan Sick, Chris Simpson, Sudheesh Singanamalla, Leo P. Singer, Jaladh Singhal, Manodeep Sinha, Brigitta M. SipHocz, Lee R. Spitler, David Stansby, Ole Streicher, Jani Sumak, John D. Swinbank, Dan S. Taranu, Nikita Tewary, Grant R. Tremblay, Miguel de Val-Borro, Samuel J. Van Kooten, Zlatan Vasovi'c, Shresth Verma, Jos'e Vin'icius de Miranda Cardoso, Peter K. G. Williams, Tom J. Wilson, Benjamin Winkel, W. M. Wood-Vasey, Rui Xue, Peter Yoachim, Chen Zhang, Andrea Zonca, and Astropy Project Contributors. The Astropy Project: Sustaining and Growing a Community-oriented Open-source Project and the Latest Major Release (v5.0) of the Core Package. ApJ, 935(2):167, August 2022. doi: 10.3847/1538-4357/ac7c74.

D. C. Backer, S. R. Kulkarni, C. Heiles, M. M. Davis, and W. M. Goss. A millisecond pulsar. Nature, 300 (5893):615–618, December 1982. doi: 10.1038/300615a0.

M. C. Baglio, D. M. Russell, S. Crespi, S. Covino, A. Johar, J. Homan, D. M. Bramich, P. Saikia, S. Campana, P. D'Avanzo, R. P. Fender, P. Goldoni, A. J. Goodwin, F. Lewis, N. Masetti, A. Miraval Zanon, S. E. Motta, T. Muñoz-Darias, and T. Shahbaz. Probing Jet Launching in Neutron Star X-Ray Binaries: The Variable and Polarized Jet of SAX J1808.4-3658. ApJ, 905(2):87, December 2020. doi: 10.3847/1538-4357/abc685.

Arash Bahramian, James Miller-Jones, Jay Strader, Alexandra Tetarenko, Richard Plotkin, Anthony Rushton, Vlad Tudor, Sara Motta, and Laura Shishkovsky. Radio/X-ray correlation database for X-ray binaries, May 2018. URL `https://doi.org/10.5281/zenodo.1252036`.

G. T. Bath and J. E. Pringle. The evolution of viscous discs. I - Mass transfer variations. MNRAS, 194:967–986, March 1981. doi: 10.1093/mnras/194.4.967.

MC Begelman, Andrew R King, and JE Pringle. The nature of ss433 and the ultraluminous x-ray sources. *Monthly Notices of the Royal Astronomical Society*, 370(1):399–404, 2006.

Mitchell C. Begelman, Roger D. Blandford, and Martin J. Rees. Theory of extragalactic radio sources. *Reviews of Modern Physics*, 56(2):255–351, April 1984. doi: 10.1103/RevModPhys.56.255.

A. R. Bell. Cosmic ray acceleration. *Astroparticle Physics*, 43:56–70, March 2013. doi: 10.1016/j.astropartphys.2012.05.022.

D. Bhattacharya and E. P. J. van den Heuvel. Formation and evolution of binary and millisecond radio pulsars. Phys. Rep., 203(1-2):1–124, January 1991. doi: 10.1016/0370-1573(91)90064-S.

G. R. Bhuvana and Anuj Nandi. Accretion disc dynamics in extragalactic black hole X-ray binaries: a comprehensive study of M33 X-7, NGC 300 X-1, and IC 10 X-1. MNRAS, 536(1):827–844, January 2025. doi: 10.1093/mnras/stae2651.

R. D. Blandford and A. Königl. Relativistic jets as compact radio sources. ApJ, 232:34–48, August 1979. doi: 10.1086/157262.

R. D. Blandford and D. G. Payne. Hydromagnetic flows from accretion disks and the production of radio jets. MNRAS, 199:883–903, June 1982. doi: 10.1093/mnras/199.4.883.

R. D. Blandford and R. L. Znajek. Electromagnetic extraction of energy from Kerr black holes. MNRAS, 179: 433–456, May 1977. doi: 10.1093/mnras/179.3.433.

Steven Bloemen, Paul Groot, Patrick Woudt, Marc Klein Wolt, Vanessa McBride, Gijs Nelemans, Elmar Körding, Margaretha L. Pretorius, Ronald Roelfsema, Felix Bettonvil, Harry Balster, Roy Bakker, Peter Dolron, Arjen van Elteren, Eddy Elswijk, Arno Engels, Rob Fender, Marc Fokker, Menno de Haan, Klaas Hagoort, Jasper de Hoog, Rik ter Horst, Giel van der Kevie, Stanisław Kozłowski, Jan Kragt, Grzegorz Lech, Rudolf Le Poole, Dirk Lesman, Johan Morren, Ramon Navarro, Willem-Jelle Paalberends, Kerry Paterson, Rafal Pawłaszek, Wim Pessemier, Gert Raskin, Harrie Rutten, Bart Scheers, Menno Schuil, and Piotr W. Sybilski. MeerLICHT and BlackGEM: custom-built telescopes to detect faint optical transients. In Helen J. Hall, Roberto Gilmozzi, and Heather K. Marshall, editors, *Ground-based and Airborne Telescopes VI*, volume 9906 of *Society of Photo-Optical Instrumentation Engineers (SPIE) Conference Series*, page 990664, July 2016. doi: 10.1117/12.2232522.

H. V. Bradt, R. E. Rothschild, and J. H. Swank. X-ray timing explorer mission. A&AS, 97(1):355–360, January 1993.

H. V. D. Bradt and J. E. McClintock. The optical Counterparts of Compact discrete galactic X-Ray sources. ARA&A, 21:13–66, January 1983. doi: 10.1146/annurev.aa.21.090183.000305.

Peter Bult, Gaurava K. Jaisawal, Tolga Güver, Tod E. Strohmayer, Diego Altamirano, Zaven Arzoumanian, David R. Ballantyne, Deepto Chakrabarty, Jérôme Chenevez, Keith C. Gendreau, Sebastien Guillot, and Renee M. Ludlam. A NICER Thermonuclear Burst from the Millisecond X-Ray Pulsar SAX J1808.4-3658. ApJ, 885(1):L1, November 2019. doi: 10.3847/2041-8213/ab4ae1.

Peter Bult, Deepto Chakrabarty, Zaven Arzoumanian, Keith C. Gendreau, Sebastien Guillot, Christian Malacaria, Paul. S. Ray, and Tod E. Strohmayer. Timing the Pulsations of the Accreting Millisecond Pulsar SAX J1808.4-3658 during Its 2019 Outburst. ApJ, 898(1):38, July 2020. doi: 10.3847/1538-4357/ab9827.

David N. Burrows, J. E. Hill, J. A. Nousek, J. A. Kennea, A. Wells, J. P. Osborne, A. F. Abbey, A. Beardmore, K. Mukerjee, A. D. T. Short, G. Chincarini, S. Campana, O. Citterio, A. Moretti, C. Pagani, G. Tagliaferri, P. Giommi, M. Capalbi, F. Tamburelli, L. Angelini, G. Cusumano, H. W. Bräuninger, W. Burkert, and G. D. Hartner. The Swift X-Ray Telescope. Space Sci. Rev., 120(3-4):165–195, October 2005. doi: 10.1007/s11214-005-5097-2.

D. E. Calvelo, R. P. Fender, A. K. Tzioumis, N. Kawai, J. W. Broderick, and M. E. Bell. Radio observations of Circinus X-1 over a complete orbit at an historically faint epoch. MNRAS, 419(1):436–451, January 2012. doi: 10.1111/j.1365-2966.2011.19708.x.

Sergio Campana and Tiziana Di Salvo. Accreting Pulsars: Mixing-up Accretion Phases in Transitional Systems. In Luciano Rezzolla, Pierre Pizzochero, David Ian Jones, Nanda Rea, and Isaac Vidaña, editors, *Astrophysics and Space Science Library*, volume 457 of *Astrophysics and Space Science Library*, page 149, January 2018. doi: 10.1007/978-3-319-97616-7_4.

Xinwu Cao and Dong Lai. Jet production in black hole X-ray binaries and active galactic nuclei: mass feeding and advection of magnetic fields. MNRAS, 485(2):1916–1923, May 2019. doi: 10.1093/mnras/stz580.

C. L. Carilli, R. A. Perley, J. W. Dreher, and J. P. Leahy. Multifrequency Radio Observations of Cygnus A: Spectral Aging in Powerful Radio Galaxies. ApJ, 383:554, December 1991. doi: 10.1086/170813.

F. Carotenuto, S. Corbel, E. Tremou, T. D. Russell, A. Tzioumis, R. P. Fender, P. A. Woudt, S. E. Motta, J. C. A. Miller-Jones, A. J. Tetarenko, and G. R. Sivakoff. The hybrid radio/X-ray correlation of the black hole transient MAXI J1348-630. MNRAS, 505(1):L58–L63, July 2021. doi: 10.1093/mnrasl/slab049.

CASA Team, Ben Bean, Sanjay Bhatnagar, Sandra Castro, Jennifer Donovan Meyer, Bjorn Emonts, Enrique Garcia, Robert Garwood, Kumar Golap, Justo Gonzalez Villalba, Pamela Harris, Yohei Hayashi, Josh Hoskins, Mingyu Hsieh, Preshanth Jagannathan, Wataru Kawasaki, Aard Keimpema, Mark Kettenis, Jorge Lopez, Joshua Marvil, Joseph Masters, Andrew McNichols, David Mehringer, Renaud Miel, George Moellenbrock, Federico Montesino, Takeshi Nakazato, Juergen Ott, Dirk Petry, Martin Pokorny, Ryan Raba, Urvashi Rau, Darrell Schiebel, Neal Schweighart, Srikrishna Sekhar, Kazuhiko Shimada, Des Small, Jan-Willem Steeb, Kanako Sugimoto, Ville Suoranta, Takahiro Tsutsumi, Ilse M. van Bemmel, Marjolein Verkouter, Akeem Wells, Wei Xiong, Arpad Szomoru, Morgan Griffith, Brian Glendenning, and Jeff Kern. CASA, the Common Astronomy Software Applications for Radio Astronomy. PASP, 134(1041):114501, November 2022. doi: 10.1088/1538-3873/ac9642.

Sandip Chakrabarti and Lev G. Titarchuk. Spectral Properties of Accretion Disks around Galactic and Extragalactic Black Holes. ApJ, 455:623, December 1995. doi: 10.1086/176610.

Deepto Chakrabarty and Edward H. Morgan. The two-hour orbit of a binary millisecond X-ray pulsar. Nature, 394(6691):346–348, July 1998. doi: 10.1038/28561.

Amar Deo Chandra. Rapid X-ray brightening of XTE J1701-462. *The Astronomer's Telegram*, 15602:1, September 2022.

Roger A. Chevalier. Young Core-Collapse Supernova Remnants and Their Supernovae. ApJ, 619(2):839–855, February 2005. doi: 10.1086/426584.

D. H. Clark, J. H. Parkinson, and J. L. Caswell. Is CIR X-1 a runaway binary. Nature, 254:674–676, April 1975. doi: 10.1038/254674a0.

Massimo Cocchi, Andrea Gnarini, Sergio Fabiani, Francesco Ursini, Juri Poutanen, Fiamma Capitanio, Anna Bobrikova, Ruben Farinelli, Adamantia Paizis, Lara Sidoli, Alexandra Veledina, Stefano Bianchi, Alessandro Di Marco, Adam Ingram, Jari J. E. Kajava, Fabio La Monaca, Giorgio Matt, Christian Malacaria, Romana Mikušincová, John Rankin, Silvia Zane, Iván Agudo, Lucio A. Antonelli, Matteo Bachetti, Luca Baldini, Wayne H. Baumgartner, Ronaldo Bellazzini, Stephen D. Bongiorno, Raffaella Bonino, Alessandro Brez, Niccolò Bucciantini, Simone Castellano, Elisabetta Cavazzuti, Chien-Ting Chen, Stefano Ciprini, Enrico Costa, Alessandra De Rosa, Ettore Del Monte, Laura Di Gesu, Niccolò Di Lalla, Immacolata Donnarumma, Victor Doroshenko, Michal Dovčiak, Steven R. Ehlert, Teruaki Enoto, Yuri Evangelista, Riccardo Ferrazzoli, Javier A. Garcia, Shuichi Gunji, Kiyoshi Hayashida, Jeremy Heyl, Wataru Iwakiri, Svetlana G. Jorstad, Philip Kaaret, Vladimir Karas, Fabian Kislat, Takao Kitaguchi, Jeffery J. Kolodziejczak, Henric Krawczynski, Luca Latronico, Ioannis Liodakis, Simone Maldera, Alberto Manfreda, Frédéric Marin, Andrea Marinucci, Alan P. Marscher, Herman L. Marshall, Francesco Massaro, Ikuyuki Mitsuishi, Tsunefumi Mizuno, Fabio Muleri, Michela Negro, Chi-Yung Ng, Stephen L. O'Dell, Nicola Omodei, Chiara Oppedisano, Alessandro Papitto, George G. Pavlov, Abel L. Peirson, Matteo Perri, Melissa Pesce-Rollins, Pierre-Olivier Petrucci, Maura Pilia, Andrea Possenti, Simonetta Puccetti, Brian D. Ramsey, Ajay Ratheesh, Oliver J. Roberts, Roger W. Romani, Carmelo Sgrò, Patrick Slane, Paolo Soffitta, Gloria Spandre, Douglas A. Swartz, Toru Tamagawa, Fabrizio Tavecchio, Roberto Taverna, Yuzuru Tawara, Allyn F. Tennant, Nicholas E. Thomas, Francesco Tombesi, Alessio Trois, Sergey S. Tsygankov, Roberto Turolla, Jacco Vink, Martin C. Weisskopf, Kinwah Wu, and Fei Xie. Discovery of strongly variable X-ray polarization in the neutron star low-mass X-ray binary transient XTE J1701−462. A&A, 674:L10, June 2023. doi: 10.1051/0004-6361/202346275.

Angus Comrie, Kuo-Song Wang, Shou-Chieh Hsu, Anthony Moraghan, Pamela Harris, Qi Pang, Adrianna Pińska, Cheng-Chin Chiang, Tien-Hao Chang, Yu-Hsuan Hwang, Hengtai Jan, Ming-Yi Lin, and Rob Simmonds. CARTA: The Cube Analysis and Rendering Tool for Astronomy, June 2021.

P. S. Conti. Mass loss in early-type stars. ARA&A, 16:371–392, January 1978. doi: 10.1146/annurev.aa.16.090178.002103.

Ioannis Contopoulos and Demosthenes Kazanas. A Cosmic Battery. ApJ, 508(2):859–863, December 1998. doi: 10.1086/306426.

S. Corbel, R. P. Fender, A. K. Tzioumis, M. Nowak, V. McIntyre, P. Durouchoux, and R. Sood. Coupling of the X-ray and radio emission in the black hole candidate and compact jet source GX 339-4. A&A, 359:251–268, July 2000.

S. Corbel, M. A. Nowak, R. P. Fender, A. K. Tzioumis, and S. Markoff. Radio/X-ray correlation in the low/hard state of GX 339-4. A&A, 400:1007–1012, March 2003. doi: 10.1051/0004-6361:20030090.

S. Corbel, M. Coriat, C. Brocksopp, A. K. Tzioumis, R. P. Fender, J. A. Tomsick, M. M. Buxton, and C. D. Bailyn. The 'universal' radio/X-ray flux correlation: the case study of the black hole GX 339-4. MNRAS, 428(3):2500–2515, January 2013. doi: 10.1093/mnras/sts215.

M. Coriat, S. Corbel, L. Prat, J. C. A. Miller-Jones, D. Cseh, A. K. Tzioumis, C. Brocksopp, J. Rodriguez, R. P. Fender, and G. R. Sivakoff. Accretion-outflow connection in the outliers of the "universal" radio/X-ray correlation. In Gustavo E. Romero, Rashid A. Sunyaev, and Tomaso Belloni, editors, *Jets at All Scales*, volume 275, pages 255–259, February 2011. doi: 10.1017/S174392131001611X.

M. Coriat, R. P. Fender, C. Tasse, O. Smirnov, A. K. Tzioumis, and J. W. Broderick. The twisted jets of Circinus X-1. MNRAS, 484(2):1672–1686, April 2019. doi: 10.1093/mnras/stz099.

R. Cornelisse, J. J. M. in't Zand, F. Verbunt, E. Kuulkers, J. Heise, P. R. den Hartog, M. Cocchi, L. Natalucci, A. Bazzano, and P. Ubertini. Six years of BeppoSAX Wide Field Cameras observations of nine galactic type I X-ray bursters. A&A, 405:1033–1042, July 2003. doi: 10.1051/0004-6361:20030629.

Flavio D'Amico, William A. Heindl, Richard E. Rothschild, and Duane E. Gruber. High-Energy X-Ray Timing Experiment Detections of Hard X-Ray Tails in Scorpius X-1. ApJ, 547(2):L147–L150, February 2001. doi: 10.1086/318902.

Kris Davidson and Jeremiah P. Ostriker. Neutron-Star Accretion in a Stellar Wind: Model for a Pulsed X-Ray Source. ApJ, 179:585–598, January 1973. doi: 10.1086/151897.

R. E. Davies and J. E. Pringle. On accretion from an inhomogeneous medium. MNRAS, 191:599–604, May 1980. doi: 10.1093/mnras/191.3.599.

P. A. J. de Korte, J. A. M. Bleeker, A. J. F. den Boggende, G. Branduardi-Raymont, A. C. Brinkman, J. L. Culhane, E. H. B. M. Gronenschild, I. Mason, and S. P. McKechnie. The X-Ray Imaging Telescopes on EXOSAT. Space Sci. Rev., 30(1-4):495–511, March 1981. doi: 10.1007/BF01246070.

Walter Dehnen and James Binney. Mass models of the milky way. *Monthly Notices of the Royal Astronomical Society*, 294(3):429–438, 1998.

A. T. Deller, J. Moldon, J. C. A. Miller-Jones, A. Patruno, J. W. T. Hessels, A. M. Archibald, Z. Paragi, G. Heald, and N. Vilchez. Radio Imaging Observations of PSR J1023+0038 in an LMXB State. ApJ, 809(1): 13, August 2015. doi: 10.1088/0004-637X/809/1/13.

G. Q. Ding, J. L. Qu, and T. P. Li. Evolution of Hard X-Ray Spectra along the Branches in Circinus X-1. ApJ, 596(2):L219–L222, October 2003. doi: 10.1086/379338.

G. Q. Ding, S. N. Zhang, N. Wang, J. L. Qu, and S. P. Yan. On the Nature of the First Transient Z Source XTE J1701-462: Its Accretion Disk Structure, Neutron Star Magnetic Field Strength, and Hard Tail. AJ, 142(2):34, August 2011. doi: 10.1088/0004-6256/142/2/34.

Paul C. Duffell and Tanmoy Laskar. On the Deceleration and Spreading of Relativistic Jets. I. Jet Dynamics. ApJ, 865(2):94, October 2018. doi: 10.3847/1538-4357/aadb9c.

Jayanne English. Canvas and cosmos: Visual art techniques applied to astronomy data. *International Journal of Modern Physics D*, 26(4):1730010, January 2017. doi: 10.1142/S0218271817300105.

Jayanne English, Mark L. A. Richardson, Gilles Ferrand, and Nathan Deg. CosmosCanvas: Useful color maps for different astrophysical properties. Astrophysics Source Code Library, record ascl:2401.005, January 2024.

H. Falcke and P. L. Biermann. The jet-disk symbiosis. I. Radio to X-ray emission models for quasars. A&A, 293:665–682, January 1995. doi: 10.48550/arXiv.astro-ph/9411096.

H. Falcke and P. L. Biermann. Galactic jet sources and the AGN connection. A&A, 308:321–329, April 1996. doi: 10.48550/arXiv.astro-ph/9506138.

H. Falcke, E. Körding, and S. Markoff. A scheme to unify low-power accreting black holes. Jet-dominated accretion flows and the radio/X-ray correlation. A&A, 414:895–903, February 2004. doi: 10.1051/0004-6361:20031683.

R. Farinelli, A. Paizis, R. Landi, and L. Titarchuk. The X-ray spectral evolution of Cygnus X-2 in the framework of bulk Comptonization. A&A, 498(2):509–516, May 2009. doi: 10.1051/0004-6361/200810422.

R. Farinelli, S. Fabiani, J. Poutanen, F. Ursini, C. Ferrigno, S. Bianchi, M. Cocchi, F. Capitanio, A. De Rosa, A. Gnarini, F. Kislat, G. Matt, R. Mikusincova, F. Muleri, I. Agudo, L. A. Antonelli, M. Bachetti, L. Baldini, W. H. Baumgartner, R. Bellazzini, S. D. Bongiorno, R. Bonino, A. Brez, N. Bucciantini, S. Castellano, E. Cavazzuti, S. Ciprini, E. Costa, E. Del Monte, L. Di Gesu, N. Di Lalla, A. Di Marco, I. Donnarumma, V. Doroshenko, M. Dovčiak, S. R. Ehlert, T. Enoto, Y. Evangelista, R. Ferrazzoli, J. A. Garcia, S. Gunji, K. Hayashida, J. Heyl, W. Iwakiri, S. G. Jorstad, V. Karas, T. Kitaguchi, J. J. Kolodziejczak, H. Krawczynski, F. La Monaca, L. Latronico, I. Liodakis, S. Maldera, A. Manfreda, F. Marin, A. P. Marscher, H. L. Marshall, I. Mitsuishi, T. Mizuno, C. Y. Ng, S. L. O'Dell, N. Omodei, C. Oppedisano, A. Papitto, G. G. Pavlov, A. L. Peirson, M. Perri, M. Pesce-Rollins, P. O. Petrucci, M. Pilia, A. Possenti, S. Puccetti, B. D. Ramsey, J. Rankin, A. Ratheesh, R. W. Romani, C. Sgrò, P. Slane, P. Soffitta, G. Spandre, T. Tamagawa, F. Tavecchio, R. Taverna, Y. Tawara, A. F. Tennant, N. E. Thomas, F. Tombesi, A. Trois, S. S. Tsygankov, R. Turolla, J. Vink, M. C. Weisskopf, K. Wu, F. Xie, and S. Zane. Accretion geometry of the neutron star low mass X-ray binary Cyg X-2 from X-ray polarization measurements. MNRAS, 519(3):3681–3690, March 2023. doi: 10.1093/mnras/stac3726.

R. Fender, P. A. Woudt, S. Corbel, M. Coriat, F. Daigne, H. Falcke, J. Girard, I. Heywood, A. Horesh, J. Horrell, P. G. Jonker, T. Joseph, A. Kamble, C. Knigge, E. Körding, M. Kotze, C. Kouveliotou, C. Lynch, T. Maccarone, P. Meintjes, S. Migliari, T. Murphy, T. Nagayama, G. Nelemans, G. Nicholson, T. O'Brien, A. Oodendaal, N. Oozeer, J. Osborne, M. Pérez-Torres, S. Ratcliffe, V. A. R. M. Ribeiro, E. Rol, A. Rushton, A. Scaife, M. Schurch, G. Sivakoff, T. Staley, D. Steeghs, I. Stewart, J. D. Swinbank, S. Vergani, B. Warner, K. Wiersema, R. Armstrong, P. Groot, V. McBride, J. C. A. Miller-Jones, K. Mooley, B. Stappers, R. A. M. J. Wijers, M. Bietenholz, S. Blyth, M. Böttcher, D. Buckley, P. Charles, L. Chomiuk, D. Coppejans, W. J. G. de Blok, K. van der Heyden, A. van der Horst, and B. van Soelen. ThunderKAT: The MeerKAT Large Survey Project for Image-Plane Radio Transients. In *MeerKAT Science: On the Pathway to the SKA*, page 13, January 2016.

R. P. Fender and E. Kuulkers. On the peak radio and X-ray emission from neutron star and black hole candidate X-ray transients. MNRAS, 324(4):923–930, July 2001. doi: 10.1046/j.1365-8711.2001.04345.x.

R. P. Fender, T. M. Belloni, and E. Gallo. Towards a unified model for black hole X-ray binary jets. MNRAS, 355(4):1105–1118, December 2004a. doi: 10.1111/j.1365-2966.2004.08384.x.

R. P. Fender, M. Dahlem, J. Homan, S. Corbel, R. Sault, and T. M. Belloni. The variable radio counterpart and possible large-scale jet of the new Z source XTE J1701-462. MNRAS, 380(1):L25–L29, September 2007. doi: 10.1111/j.1745-3933.2007.00350.x.

R. P. Fender, J. Homan, and T. M. Belloni. Jets from black hole X-ray binaries: testing, refining and extending empirical models for the coupling to X-rays. MNRAS, 396(3):1370–1382, July 2009. doi: 10.1111/j.1365-2966.2009.14841.x.

R. P. Fender, K. P. Mooley, S. E. Motta, J. S. Bright, D. R. A. Williams, A. P. Rushton, R. J. Beswick, J. C. A. Miller-Jones, M. Kimura, K. Isogai, and T. Kato. Comprehensive coverage of particle acceleration and kinetic feedback from the stellar mass black hole V404 Cygni. MNRAS, 518(1):1243–1259, January 2023. doi: 10.1093/mnras/stac1836.

Rob Fender and Tomaso Belloni. Stellar-Mass Black Holes and Ultraluminous X-ray Sources. *Science*, 337 (6094):540, August 2012. doi: 10.1126/science.1221790.

Rob Fender and Joe Bright. Synchrotron self-absorption and the minimum energy of optically thick radio flares from stellar mass black holes. MNRAS, 489(4):4836–4846, November 2019. doi: 10.1093/mnras/stz2000.

Rob Fender, Kinwah Wu, Helen Johnston, Tasso Tzioumis, Peter Jonker, Ralph Spencer, and Michiel van der Klis. An ultra-relativistic outflow from a neutron star accreting gas from a companion. Nature, 427(6971): 222–224, January 2004b. doi: 10.1038/nature02137.

Robert Fender, Ralph Spencer, Tasso Tzioumis, Kinwah Wu, Michiel van der Klis, Jan van Paradijs, and Helen Johnston. An Asymmetric Arcsecond Radio Jet from Circinus X-1. ApJ, 506(2):L121–L125, October 1998. doi: 10.1086/311660.

Ryuichi Fujimoto, Kazuhisa Mitsuda, Dan Mccammon, Yoh Takei, Michael Bauer, Yoshitaka Ishisaki, Scott F. Porter, Hiroya Yamaguchi, Kiyoshi Hayashida, and Noriko Y. Yamasaki. Evidence for Solar-Wind Charge-Exchange X-Ray Emission from the Earth's Magnetosheath. PASJ, 59:133–140, January 2007. doi: 10.1093/pasj/59.sp1.S133.

E. Gallo, R. P. Fender, and G. G. Pooley. A universal radio-X-ray correlation in low/hard state black hole binaries. MNRAS, 344(1):60–72, September 2003. doi: 10.1046/j.1365-8711.2003.06791.x.

E. Gallo, J. C. A. Miller-Jones, D. M. Russell, P. G. Jonker, J. Homan, R. M. Plotkin, S. Markoff, B. P. Miller, S. Corbel, and R. P. Fender. The radio/X-ray domain of black hole X-ray binaries at the lowest radio luminosities. MNRAS, 445(1):290–300, November 2014. doi: 10.1093/mnras/stu1599.

Elena Gallo, Nathalie Degenaar, and Jakob van den Eijnden. Hard state neutron star and black hole X-ray binaries in the radio:X-ray luminosity plane. MNRAS, 478(1):L132–L136, July 2018. doi: 10.1093/mnrasl/sly083.

Duncan K. Galloway and Andrew Cumming. Helium-rich Thermonuclear Bursts and the Distance to the Accretion-powered Millisecond Pulsar SAX J1808.4-3658. ApJ, 652(1):559–568, November 2006. doi: 10.1086/507598.

K. V. S. Gasealahwe, I. M. Monageng, R. P. Fender, P. A. Woudt, S. E. Motta, J. van den Eijnden, D. R. A. Williams, I. Heywood, S. Bloemen, P. J. Groot, P. Vreeswijk, V. McBride, M. Klein-Wolt, E. Körding, R. Le Poole, D. Pieterse, and S. de Wet. The 2019 outburst of AMXP SAX J1808.4-3658 and radio follow up of MAXI J0911-655 and XTE J1701-462. MNRAS, 521(2):2806–2813, May 2023. doi: 10.1093/mnras/stad649.

Keith C. Gendreau, Zaven Arzoumanian, and Takashi Okajima. The Neutron star Interior Composition ExploreR (NICER): an Explorer mission of opportunity for soft x-ray timing spectroscopy. In Tadayuki Takahashi, Stephen S. Murray, and Jan-Willem A. den Herder, editors, *Space Telescopes and Instrumentation 2012: Ultraviolet to Gamma Ray*, volume 8443 of *Society of Photo-Optical Instrumentation Engineers (SPIE) Conference Series*, page 844313, September 2012a. doi: 10.1117/12.926396.

Keith C. Gendreau, Zaven Arzoumanian, and Takashi Okajima. The Neutron star Interior Composition ExploreR (NICER): an Explorer mission of opportunity for soft x-ray timing spectroscopy. In Tadayuki Takahashi, Stephen S. Murray, and Jan-Willem A. den Herder, editors, *Space Telescopes and Instrumentation 2012: Ultraviolet to Gamma Ray*, volume 8443 of *Society of Photo-Optical Instrumentation Engineers (SPIE) Conference Series*, page 844313, September 2012b. doi: 10.1117/12.926396.

Keith C. Gendreau, Zaven Arzoumanian, Phillip W. Adkins, Cheryl L. Albert, John F. Anders, Andrew T. Aylward, Charles L. Baker, Erin R. Balsamo, William A. Bamford, Suyog S. Benegalrao, Daniel L. Berry, Shiraz Bhalwani, J. Kevin Black, Carl Blaurock, Ginger M. Bronke, Gary L. Brown, Jason G. Budinoff, Jeffrey D. Cantwell, Thoniel Cazeau, Philip T. Chen, Thomas G. Clement, Andrew T. Colangelo, Jerry S. Coleman, Jonathan D. Coopersmith, William E. Dehaven, John P. Doty, Mark D. Egan, Teruaki Enoto, Terry W. Fan, Deneen M. Ferro, Richard Foster, Nicholas M. Galassi, Luis D. Gallo, Chris M. Green, Dave Grosh, Kong Q. Ha, Monther A. Hasouneh, Kristofer B. Heefner, Phyllis Hestnes, Lisa J. Hoge, Tawanda M. Jacobs, John L. Jørgensen, Michael A. Kaiser, James W. Kellogg, Steven J. Kenyon, Richard G. Koenecke, Robert P. Kozon, Beverly LaMarr, Mike D. Lambertson, Anne M. Larson, Steven Lentine, Jesse H. Lewis, Michael G. Lilly, Kuochia Alice Liu, Andrew Malonis, Sridhar S. Manthripragada, Craig B. Markwardt, Bryan D. Matonak, Isaac E. Mcginnis, Roger L. Miller, Alissa L. Mitchell, Jason W. Mitchell, Jelila S. Mohammed, Charles A. Monroe, Kristina M. Montt de Garcia, Peter D. Mulé, Louis T. Nagao, Son N. Ngo, Eric D. Norris, Dwight A. Norwood, Joseph Novotka, Takashi Okajima, Lawrence G. Olsen, Chimaobi O. Onyeachu, Henry Y. Orosco, Jacqualine R. Peterson, Kristina N. Pevear, Karen K. Pham, Sue E. Pollard, John S. Pope, Daniel F. Powers, Charles E. Powers, Samuel R. Price, Gregory Y. Prigozhin, Julian B. Ramirez, Winston J. Reid, Ronald A. Remillard, Eric M. Rogstad, Glenn P. Rosecrans, John N. Rowe, Jennifer A. Sager, Claude A. Sanders, Bruce Savadkin, Maxine R. Saylor, Alexander F. Schaeffer, Nancy S. Schweiss, Sean R. Semper, Peter J. Serlemitsos, Larry V. Shackelford, Yang Soong, Jonathan Struebel, Michael L. Vezie, Joel S. Villasenor, Luke B. Winternitz, George I. Wofford, Michael R. Wright, Mike Y. Yang, and Wayne H. Yu. The Neutron star Interior Composition Explorer (NICER): design and development. In Jan-Willem A. den Herder, Tadayuki Takahashi, and Marshall Bautz, editors, *Space Telescopes and Instrumentation 2016: Ultraviolet to Gamma Ray*, volume 9905 of *Society of Photo-Optical Instrumentation Engineers (SPIE) Conference Series*, page 99051H, July 2016. doi: 10.1117/12.2231304.

Marek Gierliński, Andrzej A. Zdziarski, Juri Poutanen, Paolo S. Coppi, Ken Ebisawa, and W. Neil Johnson. Radiation mechanisms and geometry of Cygnus X-1 in the soft state. MNRAS, 309(2):496–512, October 1999. doi: 10.1046/j.1365-8711.1999.02875.x.

Paul T. Goodall, Fathallah Alouani-Bibi, and Katherine M. Blundell. When microquasar jets and supernova collide: hydrodynamically simulating the SS 433-W 50 interaction. MNRAS, 414(4):2838–2859, July 2011. doi: 10.1111/j.1365-2966.2011.18388.x.

A. J. Goodwin, D. M. Russell, D. K. Galloway, M. C. Baglio, A. S. Parikh, D. A. H. Buckley, J. Homan, D. M. Bramich, J. J. M. in't Zand, C. O. Heinke, E. J. Kotze, D. de Martino, A. Papitto, F. Lewis, and R. Wijnands. Enhanced optical activity 12 d before X-ray activity, and a 4 d X-ray delay during outburst rise, in a low-mass X-ray binary. MNRAS, 498(3):3429–3439, November 2020. doi: 10.1093/mnras/staa2588.

Jonathan Granot and Tsvi Piran. On the lateral expansion of gamma-ray burst jets. MNRAS, 421(1):570–587, March 2012. doi: 10.1111/j.1365-2966.2011.20335.x.

Paul J. Groot. The multi-colour dynamic Universe explored. *Nature Astronomy*, 3:1160–1160, December 2019. doi: 10.1038/s41550-019-0964-z.

N. V. Gusinskaia, J. W. T. Hessels, N. Degenaar, A. T. Deller, J. C. A. Miller-Jones, A. M. Archibald, C. O. Heinke, J. Moldón, A. Patruno, J. A. Tomsick, and R. Wijnands. Quasi-simultaneous radio and X-ray observations of Aql X-1 : probing low luminosities. MNRAS, 492(2):2858–2871, February 2020. doi: 10.1093/mnras/stz3420.

Christopher A. Hales. Calibration Errors in Interferometric Radio Polarimetry. AJ, 154(2):54, August 2017. doi: 10.3847/1538-3881/aa7aef.

D. C. Hannikainen, R. W. Hunstead, D. Campbell-Wilson, and R. K. Sood. MOST radio monitoring of GX 339-4. A&A, 337:460–464, September 1998. doi: 10.48550/arXiv.astro-ph/9805332.

M. J. Hardcastle and M. G. H. Krause. Numerical modelling of the lobes of radio galaxies in cluster environments. MNRAS, 430(1):174–196, March 2013. doi: 10.1093/mnras/sts564.

Jacob M. Hartman, Alessandro Patruno, Deepto Chakrabarty, Craig B. Markwardt, Edward H. Morgan, Michiel van der Klis, and Rudy Wijnands. A Decade of Timing an Accretion-powered Millisecond Pulsar: The Continuing Spin Down and Orbital Evolution of SAX J1808.4-3658. ApJ, 702(2):1673–1678, September 2009. doi: 10.1088/0004-637X/702/2/1673.

G. Hasinger and M. van der Klis. Two patterns of correlated X-ray timing and spectral behaviour in low-mass X-ray binaries. A&A, 225:79–96, November 1989.

John F. Hawley, Christian Fendt, Martin Hardcastle, Elena Nokhrina, and Alexander Tchekhovskoy. Disks and Jets. Gravity, Rotation and Magnetic Fields. Space Sci. Rev., 191(1-4):441–469, October 2015. doi: 10.1007/s11214-015-0174-7.

R. F. Haynes, M. M. Komesaroff, A. G. Little, D. L. Jauncey, J. L. Caswell, D. K. Milne, M. J. Kesteven, K. J. Wellington, and R. A. Preston. A radio nebula associated with Circinus X-1. Nature, 324(6094):233–235, November 1986. doi: 10.1038/324233a0.

S. Heinz, P. Sell, R. P. Fender, P. G. Jonker, W. N. Brandt, D. E. Calvelo-Santos, A. K. Tzioumis, M. A. Nowak, N. S. Schulz, R. Wijnands, and M. van der Klis. The Youngest Known X-Ray Binary: Circinus X-1 and Its Natal Supernova Remnant. ApJ, 779(2):171, December 2013. doi: 10.1088/0004-637X/779/2/171.

S. Heinz, M. Burton, C. Braiding, W. N. Brandt, P. G. Jonker, P. Sell, R. P. Fender, M. A. Nowak, and N. S. Schulz. Lord of the Rings: A Kinematic Distance to Circinus X-1 from a Giant X-Ray Light Echo. ApJ, 806 (2):265, June 2015. doi: 10.1088/0004-637X/806/2/265.

E. A. Helder, J. Vink, C. G. Bassa, A. Bamba, J. A. M. Bleeker, S. Funk, P. Ghavamian, K. J. van der Heyden, F. Verbunt, and R. Yamazaki. Measuring the Cosmic-Ray Acceleration Efficiency of a Supernova Remnant. *Science*, 325(5941):719, August 2009. doi: 10.1126/science.1173383.

I. Heywood, M. J. Jarvis, C. L. Hale, I. H. Whittam, H. L. Bester, B. Hugo, J. S. Kenyon, M. Prescott, O. M. Smirnov, C. Tasse, J. M. Afonso, P. N. Best, J. D. Collier, R. P. Deane, B. S. Frank, M. J. Hardcastle, K. Knowles, N. Maddox, E. J. Murphy, I. Prandoni, S. M. Randriamampandry, M. G. Santos, S. Sekhar, F. Tabatabaei, A. R. Taylor, and K. Thorat. MIGHTEE: total intensity radio continuum imaging and the COSMOS/XMM-LSS Early Science fields. MNRAS, 509(2):2150–2168, January 2022. doi: 10.1093/mnras/stab3021.

Ian Heywood. oxkat: Semi-automated imaging of MeerKAT observations. Astrophysics Source Code Library, record ascl:2009.003, September 2020.

Jeroen Homan, Rudy Wijnands, Michiel van der Klis, Tomaso Belloni, Jan van Paradijs, Marc Klein-Wolt, Rob Fender, and Mariano Méndez. Correlated X-Ray Spectral and Timing Behavior of the Black Hole Candidate XTE J1550-564: A New Interpretation of Black Hole States. ApJS, 132(2):377–402, February 2001. doi: 10.1086/318954.

Jeroen Homan, Tomaso Belloni, Michiel van der Klis, Piergiorgio Casella, Mariano Mendez, Walter Lewin, Rob Fender, Elena Gallo, and Neil Gehrels. Continuing RXTE observations of XTE J1701-462: a new "Z" in town? *The Astronomer's Telegram*, 725:1, February 2006a.

Jeroen Homan, Tomaso Belloni, Michiel van der Klis, Piergiorgio Casella, Mariano Mendez, Walter Lewin, Rob Fender, Elena Gallo, and Neil Gehrels. Spectral evolution and kHz QPOs in the transient Z source XTE J1701-462. *The Astronomer's Telegram*, 748:1, February 2006b.

Jeroen Homan, Michiel van der Klis, Rudy Wijnands, Tomaso Belloni, Rob Fender, Marc Klein-Wolt, Piergiorgio Casella, Mariano Méndez, Elena Gallo, Walter H. G. Lewin, and Neil Gehrels. Rossi X-Ray Timing Explorer Observations of the First Transient Z Source XTE J1701-462: Shedding New Light on Mass Accretion in Luminous Neutron Star X-Ray Binaries. ApJ, 656(1):420–430, February 2007a. doi: 10.1086/510447.

Jeroen Homan, Rudy Wijnands, Diego Altamirano, and Tomaso Belloni. Rapid decay of the neutron star transient XTE J1701-462. *The Astronomer's Telegram*, 1165:1, August 2007b.

Jeroen Homan, Michiel van der Klis, Joel K. Fridriksson, Ronald A. Remillard, Rudy Wijnands, Mariano Méndez, Dacheng Lin, Diego Altamirano, Piergiorgio Casella, Tomaso M. Belloni, and Walter H. G. Lewin. XTE J1701-462 and Its Implications for the Nature of Subclasses in Low-magnetic-field Neutron Star Low-mass X-ray Binaries. ApJ, 719(1):201–212, August 2010. doi: 10.1088/0004-637X/719/1/201.

Jeroen Homan, Gregory Sivakoff, David Pooley, Craig Heinke, Jay Strader, Vlad Tudor, and James Miller-Jones. Chandra identification of the X-ray transient MAXI J0911-635/Swift J0911.9-6452 in NGC 2808. *The Astronomer's Telegram*, 8971:1, April 2016.

J. D. Hunter. Matplotlib: A 2d graphics environment. *Computing in Science & Engineering*, 9(3):90–95, 2007. doi: 10.1109/MCSE.2007.55.

Giulia Illiano, Alessandro Papitto, Andrea Sanna, Peter Bult, Filippo Ambrosino, Arianna Miraval Zanon, Francesco Coti Zelati, Luigi Stella, Diego Altamirano, Maria Cristina Baglio, Enrico Bozzo, Luciano Burderi, Domitilla de Martino, Alessandro Di Marco, Tiziana di Salvo, Carlo Ferrigno, Vladislav Loktev, Alessio Marino, Mason Ng, Maura Pilia, Juri Poutanen, and Tuomo Salmi. Timing Analysis of the 2022 Outburst of the Accreting Millisecond X-Ray Pulsar SAX J1808.4-3658: Hints of an Orbital Shrinking. ApJ, 942(2):L40, January 2023. doi: 10.3847/2041-8213/acad81.

J. J. M. in 't Zand, J. Heise, J. M. Muller, A. Bazzano, M. Cocchi, L. Natalucci, and P. Ubertini. Discovery of the X-ray transient SAX J1808.4-3658, a likely low-mass X-ray binary. A&A, 331:L25–L28, March 1998.

Zach Ioannou, T. Naylor, W. F. Welsh, M. S. Catalán, W. J. Worraker, and N. D. James. The 'outside-in' outburst of HT Cassiopeiae. MNRAS, 310(2):398–406, December 1999. doi: 10.1046/j.1365-8711.1999.03001.x.

Keith Jahoda, Craig B. Markwardt, Yana Radeva, Arnold H. Rots, Michael J. Stark, Jean H. Swank, Tod E. Strohmayer, and William Zhang. Calibration of the Rossi X-Ray Timing Explorer Proportional Counter Array. ApJS, 163(2):401–423, April 2006. doi: 10.1086/500659.

Helen M. Johnston, Roberto Soria, and Joel Gibson. The nature of the companion star in Circinus X-1. MNRAS, 456(1):347–355, February 2016. doi: 10.1093/mnras/stv2669.

J. Jonas and MeerKAT Team. The MeerKAT Radio Telescope. In *MeerKAT Science: On the Pathway to the SKA*, page 1, January 2016. doi: 10.22323/1.277.0001.

P. C. Joss, Y. Avni, and S. Rappaport. Accreting neutron stars in highly compact binary systems and the nature of 3U 1626-67. ApJ, 221:645–651, April 1978. doi: 10.1086/156068.

L. J. Kaluzienski, S. S. Holt, E. A. Boldt, and P. J. Serlemitsos. Evidence for a 16.6 day period from Circinus X-1. ApJ, 208:L71–L75, September 1976. doi: 10.1086/182235.

J. S. Kenyon, O. M. Smirnov, T. L. Grobler, and S. J. Perkins. CubiCal: Suite for fast radio interferometric calibration. Astrophysics Source Code Library, record ascl:1805.031, May 2018.

N. D. Kylafis, I. Contopoulos, D. Kazanas, and D. M. Christodoulou. Formation and destruction of jets in X-ray binaries. A&A, 538:A5, February 2012. doi: 10.1051/0004-6361/201117052.

F. K. Lamb, C. J. Pethick, and D. Pines. A Model for Compact X-Ray Sources: Accretion by Rotating Magnetic Stars. ApJ, 184:271–290, August 1973. doi: 10.1086/152325.

Jean-Pierre Lasota. The disc instability model of dwarf novae and low-mass X-ray binary transients. , 45(7): 449–508, June 2001. doi: 10.1016/S1387-6473(01)00112-9.

C. Leibovitz and D. P. Hube. On the Detection of Black Holes. A&A, 15:251, November 1971.

Alan M. Levine, Hale Bradt, Wei Cui, J. G. Jernigan, Edward H. Morgan, Ronald Remillard, Robert E. Shirey, and Donald A. Smith. First Results from the All-Sky Monitor on the Rossi X-Ray Timing Explorer. ApJ, 469:L33, September 1996. doi: 10.1086/310260.

Walter H. G. Lewin, Jan van Paradijs, and Edward Peter Jacobus van den Heuvel. *X-ray Binaries*. 1997.

A. P. Lightman. Time-dependent accretion disks around compact objects. I. Theory and basic equations. ApJ, 194:419–427, December 1974. doi: 10.1086/153259.

Alan P. Lightman and Douglas M. Eardley. Black Holes in Binary Systems: Instability of Disk Accretion. ApJ, 187:L1, January 1974. doi: 10.1086/181377.

Dacheng Lin, Diego Altamirano, Jeroen Homan, Ronald A. Remillard, Rudy Wijnands, and Tomaso Belloni. Type I X-ray Bursts from the Neutron-star Transient XTE J1701-462. ApJ, 699(1):60–65, July 2009a. doi: 10.1088/0004-637X/699/1/60.

Dacheng Lin, Ronald A. Remillard, and Jeroen Homan. Spectral States of XTE J1701 - 462: Link Between Z and Atoll Sources. ApJ, 696(2):1257–1277, May 2009b. doi: 10.1088/0004-637X/696/2/1257.

M. Linares, P. Soleri, A. Watts, D. Altamirano, M. Armas-Padilla, Y. Cavecchi, N. Degenaar, M. Kalamkar, R. Kaur, M. van der Klis, A. Patruno, R. Wijnands, Y. Yang, P. Casella, and N. Rea. RXTE detects X-ray bursts from Circinus X-1. *The Astronomer's Telegram*, 2643:1, May 2010a.

M. Linares, A. Watts, D. Altamirano, P. Soleri, N. Degenaar, Y. Yang, R. Wijnands, P. Casella, J. Homan, D. Chakrabarty, N. Rea, M. Armas-Padilla, Y. Cavecchi, M. Kalamkar, R. Kaur, A. Patruno, and M. van der Klis. The Return of the Bursts: Thermonuclear Flashes from Circinus X-1. ApJ, 719(1):L84–L89, August 2010b. doi: 10.1088/2041-8205/719/1/L84.

S. H. Lubow and F. H. Shu. Gas dynamics of semidetached binaries. ApJ, 198:383–405, June 1975. doi: 10.1086/153614.

Bruce Margon, Michael Lampton, Stuart Bowyer, and Ray Cruddace. A Pulsing X-Ray Source in Circinus. ApJ, 169:L23, October 1971. doi: 10.1086/180806.

A. Marino, T. D. Russell, M. Del Santo, A. Beri, A. Sanna, F. Coti Zelati, N. Degenaar, D. Altamirano, E. Ambrosi, A. Anitra, F. Carotenuto, A. D'Aì, T. Di Salvo, A. Manca, S. E. Motta, C. Pinto, F. Pintore, N. Rea, and J. van den Eijnden. The accretion/ejection link in the neutron star X-ray binary 4U 1820-30 I: a boundary layer-jet coupling? MNRAS, 525(2):2366–2379, October 2023. doi: 10.1093/mnras/stad2386.

S. Markoff, H. Falcke, and R. Fender. A jet model for the broadband spectrum of XTE J1118+480. Synchrotron emission from radio to X-rays in the Low/Hard spectral state. A&A, 372:L25–L28, June 2001. doi: 10.1051/0004-6361:20010420.

N. Masetti, F. Frontera, L. Stella, M. Orlandini, A. N. Parmar, S. Del Sordo, L. Amati, E. Palazzi, D. Dal Fiume, G. Cusumano, G. Pareschi, I. Lapidus, and R. A. Remillard. Hard X-rays from Type II bursts of the Rapid Burster and its transition toward quiescence. A&A, 363:188–197, November 2000. doi: 10.48550/arXiv.astro-ph/0009044.

Masaru Matsuoka, Kazuyoshi Kawasaki, Shiro Ueno, Hiroshi Tomida, Mitsuhiro Kohama, Motoko Suzuki, Yasuki Adachi, Masaki Ishikawa, Tatehiro Mihara, Mutsumi Sugizaki, Naoki Isobe, Yujin Nakagawa, Hiroshi Tsunemi, Emi Miyata, Nobuyuki Kawai, Jun Kataoka, Mikio Morii, Atsumasa Yoshida, Hitoshi Negoro, Motoki Nakajima, Yoshihiro Ueda, Hirotaka Chujo, Kazutaka Yamaoka, Osamu Yamazaki, Satoshi Nakahira, Tetsuya You, Ryoji Ishiwata, Sho Miyoshi, Satoshi Eguchi, Kazuo Hiroi, Haruyoshi Katayama, and Ken

Ebisawa. The MAXI Mission on the ISS: Science and Instruments for Monitoring All-Sky X-Ray Images. PASJ, 61:999, October 2009a. doi: 10.1093/pasj/61.5.999.

Masaru Matsuoka, Kazuyoshi Kawasaki, Shiro Ueno, Hiroshi Tomida, Mitsuhiro Kohama, Motoko Suzuki, Yasuki Adachi, Masaki Ishikawa, Tatehiro Mihara, Mutsumi Sugizaki, Naoki Isobe, Yujin Nakagawa, Hiroshi Tsunemi, Emi Miyata, Nobuyuki Kawai, Jun Kataoka, Mikio Morii, Atsumasa Yoshida, Hitoshi Negoro, Motoki Nakajima, Yoshihiro Ueda, Hirotaka Chujo, Kazutaka Yamaoka, Osamu Yamazaki, Satoshi Nakahira, Tetsuya You, Ryoji Ishiwata, Sho Miyoshi, Satoshi Eguchi, Kazuo Hiroi, Haruyoshi Katayama, and Ken Ebisawa. The MAXI Mission on the ISS: Science and Instruments for Monitoring All-Sky X-Ray Images. PASJ, 61:999, October 2009b. doi: 10.1093/pasj/61.5.999.

James H. Matthews, Alex J. Cooper, Lauren Rhodes, Katherine Savard, Rob Fender, Francesco Carotenuto, Fraser J. Cowie, Emma L. Elley, Joe Bright, Andrew K. Hughes, and Sara E. Motta. Blast waves and reverse shocks: from ultra-relativistic GRBs to moderately relativistic X-ray binaries. MNRAS, 539(3):2665–2684, May 2025. doi: 10.1093/mnras/staf609.

Dan McCammon and Wilton T. Sanders. The soft X-ray background and its origins. ARA&A, 28:657–688, January 1990. doi: 10.1146/annurev.aa.28.090190.003301.

J. P. McMullin, B. Waters, D. Schiebel, W. Young, and K. Golap. CASA Architecture and Applications. In R. A. Shaw, F. Hill, and D. J. Bell, editors, *Astronomical Data Analysis Software and Systems XVI*, volume 376 of *Astronomical Society of the Pacific Conference Series*, page 127, October 2007.

Andrea Merloni, Sebastian Heinz, and Tiziana di Matteo. A Fundamental Plane of black hole activity. MNRAS, 345(4):1057–1076, November 2003. doi: 10.1046/j.1365-2966.2003.07017.x.

F. Meyer and E. Meyer-Hofmeister. On the elusive cause of cataclysmic variable outbursts. A&A, 104:L10–L12, January 1981.

S. Migliari and R. P. Fender. Jets in neutron star X-ray binaries: a comparison with black holes. MNRAS, 366 (1):79–91, February 2006. doi: 10.1111/j.1365-2966.2005.09777.x.

S. Migliari, R. P. Fender, M. Rupen, P. G. Jonker, M. Klein-Wolt, R. M. Hjellming, and M. van der Klis. Disc-jet coupling in an atoll-type neutron star X-ray binary: 4U 1728-34 (GX 354-0). MNRAS, 342(4):L67–L71, July 2003. doi: 10.1046/j.1365-8711.2003.06795.x.

S. Migliari, R. P. Fender, M. Rupen, S. Wachter, P. G. Jonker, J. Homan, and M. van der Klis. Radio detections of the neutron star X-ray binaries 4U 1820 - 30 and Ser X-1 in soft X-ray states. MNRAS, 351(1):186–192, June 2004. doi: 10.1111/j.1365-2966.2004.07768.x.

R. P. Mignani, A. De Luca, P. A. Caraveo, and I. F. Mirabel. HST observations rule out the association between Cir X-1 and SNR G321.9-0.3. A&A, 386:487–491, May 2002. doi: 10.1051/0004-6361:20020224.

A. Mignone and G. Bodo. An HLLC Riemann solver for relativistic flows - I. Hydrodynamics. MNRAS, 364: 126–136, November 2005. ISSN 0035-8711. doi: 10.1111/j.1365-2966.2005.09546.x. URL `http://adsabs.harvard.edu/abs/2005MNRAS.364..126M`.

A. Mignone and Jonathan C. McKinney. Equation of state in relativistic magnetohydrodynamics: variable versus constant adiabatic index. MNRAS, 378:1118–1130, July 2007. ISSN 0035-8711. doi: 10.1111/j.1365-2966.2007.11849.x. URL `http://adsabs.harvard.edu/abs/2007MNRAS.378.1118M`.

A. Mignone, G. Bodo, S. Massaglia, T. Matsakos, O. Tesileanu, C. Zanni, and A. Ferrari. PLUTO: A Numerical Code for Computational Astrophysics. *The Astrophysical Journal Supplement Series*, 170(1):228–242, 2007a. ISSN 0067-0049. doi: 10.1086/513316.

A. Mignone, G. Bodo, S. Massaglia, T. Matsakos, O. Tesileanu, C. Zanni, and A. Ferrari. PLUTO: A Numerical Code for Computational Astrophysics. ApJS, 170:228–242, May 2007b. ISSN 0067-0049. doi: 10.1086/513316. URL `http://adsabs.harvard.edu/abs/2007ApJS..170..228M`.

Tatehiro Mihara, Motoki Nakajima, Mutsumi Sugizaki, Motoko Serino, Masaru Matsuoka, Mitsuhiro Kohama, Kazuyoshi Kawasaki, Hiroshi Tomida, Shiro Ueno, Nobuyuki Kawai, Jun Kataoka, Mikio Morii, Atsumasa Yoshida, Kazutaka Yamaoka, Satoshi Nakahira, Hitoshi Negoro, Naoki Isobe, Makoto Yamauchi, and Ikuya Sakurai. Gas Slit Camera (GSC) onboard MAXI on ISS. PASJ, 63:S623–S634, November 2011. doi: 10.1093/pasj/63.sp3.S623.

K. Mitsuda, H. Inoue, K. Koyama, K. Makishima, M. Matsuoka, Y. Ogawara, N. Shibazaki, K. Suzuki, Y. Tanaka, and T. Hirano. Energy spectra of low-mass binary X-ray sources observed from Tenma. PASJ, 36:741–759, January 1984.

Kazuhisa Mitsuda, Hajime Inoue, Norio Nakamura, and Yasuo Tanaka. Luminosity-related changes of the energy spectrum of X 1608-522. PASJ, 41:97–111, January 1989.

Niruj Mohan and David Rafferty. PyBDSF: Python Blob Detection and Source Finder, February 2015.

A. Moin, C. Reynolds, J. C. A. Miller-Jones, S. J. Tingay, C. J. Phillips, A. K. Tzioumis, G. D. Nicolson, and R. P. Fender. e-VLBI observations of Circinus X-1: monitoring of the quiescent and flaring radio emission on au scales. MNRAS, 414(4):3551–3556, July 2011. doi: 10.1111/j.1365-2966.2011.18660.x.

Aditya S. Mondal, B. Raychaudhuri, and G. C. Dewangan. Evidence of disc reflection in the X-ray spectrum of the neutron star low-mass X-ray binary 4U 1636-536. MNRAS, 504(1):1331–1339, June 2021. doi: 10.1093/mnras/stab921.

G. Morlino, P. Blasi, R. Bandiera, and E. Amato. Broad Balmer line emission and cosmic ray acceleration efficiency in supernova remnant shocks. A&A, 558:A25, October 2013. doi: 10.1051/0004-6361/201322006.

Donald C. Morton. Neutron Stars as X-Ray Sources. ApJ, 140:460, August 1964. doi: 10.1086/147940.

M. Moscibrodzka. What is the hard spectral state in X-ray binaries? Insights from GRRMHD accretion flows simulations and polarization of their X-ray emission. Ap&SS, 369(7):68, July 2024. doi: 10.1007/s10509-024-04333-3.

T. Muñoz-Darias, R. P. Fender, S. E. Motta, and T. M. Belloni. Black hole-like hysteresis and accretion states in neutron star low-mass X-ray binaries. MNRAS, 443(4):3270–3283, October 2014. doi: 10.1093/mnras/stu1334.

Michael P. Muno, Ronald A. Remillard, and Deepto Chakrabarty. How Do Z and Atoll X-Ray Binaries Differ? ApJ, 568(1):L35–L39, March 2002. doi: 10.1086/340269.

M. Ng, P. M. Bult, T. E. Strohmayer, A. Sanna, K. C. Gendreau, W. C. G. Ho, and Z. Arzoumanian. NICER Follow-up of the UCXB MAXI J0911-655. *The Astronomer's Telegram*, 14767:1, July 2021.

Michael A. Nowak. Toward a Unified View of Black-Hole High-Energy States. PASP, 107:1207, December 1995. doi: 10.1086/133679.

A. R. Offringa, B. McKinley, N. Hurley-Walker, F. H. Briggs, R. B. Wayth, D. L. Kaplan, M. E. Bell, L. Feng, A. R. Neben, J. D. Hughes, J. Rhee, T. Murphy, N. D. R. Bhat, G. Bernardi, J. D. Bowman, R. J. Cappallo, B. E. Corey, A. A. Deshpande, D. Emrich, A. Ewall-Wice, B. M. Gaensler, R. Goeke, L. J. Greenhill, B. J. Hazelton, L. Hindson, M. Johnston-Hollitt, D. C. Jacobs, J. C. Kasper, E. Kratzenberg, E. Lenc, C. J. Lonsdale, M. J. Lynch, S. R. McWhirter, D. A. Mitchell, M. F. Morales, E. Morgan, N. Kudryavtseva, D. Oberoi, S. M. Ord, B. Pindor, P. Procopio, T. Prabu, J. Riding, D. A. Roshi, N. Udaya Shankar, K. S. Srivani, R. Subrahmanyan, S. J. Tingay, M. Waterson, R. L. Webster, A. R. Whitney, A. Williams, and C. L. Williams. WSCLEAN: an implementation of a fast, generic wide-field imager for radio astronomy. MNRAS, 444(1):606–619, October 2014. doi: 10.1093/mnras/stu1368.

T. Oosterbroek, M. van der Klis, E. Kuulkers, J. van Paradijs, and W. H. G. Lewin. Circinus X-1 revisited: fast-timing properties in relation to spectral state. A&A, 297:141–158, May 1995.

J. R. Oppenheimer and G. M. Volkoff. On Massive Neutron Cores. *Physical Review*, 55(4):374–381, February 1939. doi: 10.1103/PhysRev.55.374.

A. Paizis, R. Farinelli, L. Titarchuk, T. J. L. Courvoisier, A. Bazzano, V. Beckmann, F. Frontera, P. Goldoni, E. Kuulkers, S. Mereghetti, J. Rodriguez, and O. Vilhu. Average hard X-ray emission from NS LMXBs: observational evidence of different spectral states in NS LMXBs. A&A, 459(1):187–197, November 2006. doi: 10.1051/0004-6361:20065792.

A. Parikh, J. José, G. Sala, and C. Iliadis. Nucleosynthesis in type I X-ray bursts. *Progress in Particle and Nuclear Physics*, 69:225–253, March 2013. doi: 10.1016/j.ppnp.2012.11.002.

A. Patruno, D. Maitra, P. A. Curran, C. D'Angelo, J. K. Fridriksson, D. M. Russell, M. Middleton, and R. Wijnands. The Reflares and Outburst Evolution in the Accreting Millisecond Pulsar SAX J1808.4-3658: A Disk Truncated Near Co-Rotation? ApJ, 817(2):100, February 2016. doi: 10.3847/0004-637X/817/2/100.

A. Patruno, B. Haskell, and N. Andersson. The Spin Distribution of Fast-spinning Neutron Stars in Low-mass X-Ray Binaries: Evidence for Two Subpopulations. ApJ, 850(1):106, November 2017. doi: 10.3847/1538-4357/aa927a.

Alessandro Patruno and Anna L. Watts. Accreting Millisecond X-ray Pulsars. In Tomaso M. Belloni, Mariano Méndez, and Chengmin Zhang, editors, *Timing Neutron Stars: Pulsations, Oscillations and Explosions*, volume 461 of *Astrophysics and Space Science Library*, pages 143–208, January 2021. doi: 10.1007/978-3-662-62110-3_4.

Alessandro Patruno, Peter Bult, Achamveedu Gopakumar, Jacob M. Hartman, Rudy Wijnands, Michiel van der Klis, and Deepto Chakrabarty. Accelerated Orbital Expansion and Secular Spin-down of the Accreting Millisecond Pulsar SAX J1808.4-3658. ApJ, 746(2):L27, February 2012. doi: 10.1088/2041-8205/746/2/L27.

J. A. Petterson. On the occurrence of streams and disks in massive X-ray binary systems. ApJ, 224:625–630, September 1978. doi: 10.1086/156411.

David Pines, Fred K. Lamb, and Christopher J. Pethick. Models for Compact X-Ray Sources. In Dennis J. Hegyi, editor, *Sixth Texas Symposium on Relativistic Astrophysics*, volume 224, page 237, January 1973. doi: 10.1111/j.1749-6632.1973.tb41458.x.

J. Poutanen. Accretion disc-corona models and X/γ-ray spectra of accreting black holes. In M. A. Abramowicz, G. Björnsson, and J. E. Pringle, editors, *Theory of Black Hole Accretion Disks*, pages 100–122, January 1998. doi: 10.48550/arXiv.astro-ph/9805025.

Juri Poutanen and Marek Gierliński. On the nature of the X-ray emission from the accreting millisecond pulsar SAX J1808.4-3658. MNRAS, 343(4):1301–1311, August 2003. doi: 10.1046/j.1365-8711.2003.06773.x.

J. E. Pringle and M. J. Rees. Accretion Disc Models for Compact X-Ray Sources. A&A, 21:1, October 1972.

Ralph E. Pudritz, Conrad S. Rogers, and Rachid Ouyed. Controlling the collimation and rotation of hydromagnetic disc winds. MNRAS, 365(4):1131–1148, February 2006. doi: 10.1111/j.1365-2966.2005.09766.x.

V. Radhakrishnan and G. Srinivasan. On the origin of the recently discovered ultra-rapid pulsar. *Current Science*, 51:1096–1099, December 1982.

Steve Rawlings and Richard Saunders. Evidence for a common central-engine mechanism in all extragalactic radio sources. Nature, 349(6305):138–140, January 1991. doi: 10.1038/349138a0.

Pablo Reig. Be/X-ray binaries. Ap&SS, 332(1):1–29, March 2011. doi: 10.1007/s10509-010-0575-8.

R. A. Remillard, D. Lin, ASM Team at MIT, and NASA/GSFC. New X-ray Transient, XTE J1701-462. *The Astronomer's Telegram*, 696:1, January 2006.

Christopher S. Reynolds and Michael A. Nowak. Fluorescent iron lines as a probe of astrophysical black hole systems. Phys. Rep., 377(6):389–466, April 2003. doi: 10.1016/S0370-1573(02)00584-7.

Thomas D. Russell, Nathalie Degenaar, Jakob van den Eijnden, Thomas Maccarone, Alexandra J. Tetarenko, Celia Sánchez-Fernández, James C. A. Miller-Jones, Erik Kuulkers, and Melania Del Santo. Thermonuclear explosions on neutron stars reveal the speed of their jets. Nature, 627(8005):763–766, March 2024. doi: 10.1038/s41586-024-07133-5.

Payaswini Saikia, Elmar Körding, and Heino Falcke. The Fundamental Plane of black hole activity in the optical band. MNRAS, 450(3):2317–2326, July 2015. doi: 10.1093/mnras/stv731.

Payaswini Saikia, Elmar Körding, and Salome Dibi. 1.4 GHz on the Fundamental Plane of black hole activity. MNRAS, 477(2):2119–2127, June 2018. doi: 10.1093/mnras/sty754.

A. Sanna, T. Di Salvo, L. Burderi, A. Riggio, F. Pintore, A. F. Gambino, R. Iaria, M. Tailo, F. Scarano, and A. Papitto. On the timing properties of SAX J1808.4-3658 during its 2015 outburst. MNRAS, 471(1):463–477, October 2017a. doi: 10.1093/mnras/stx1588.

A. Sanna, A. Papitto, L. Burderi, E. Bozzo, A. Riggio, T. Di Salvo, C. Ferrigno, N. Rea, and R. Iaria. Discovery of a new accreting millisecond X-ray pulsar in the globular cluster NGC 2808. A&A, 598:A34, February 2017b. doi: 10.1051/0004-6361/201629406.

L. I. Sedov. Examples of Gas Motion and Certain Hypotheses on the Mechanism of Stellar Outbursts. *Reviews of Modern Physics*, 30:1077–1079, July 1958. ISSN 0034-6861. doi: 10.1103/RevModPhys.30.1077. URL `https://ui.adsabs.harvard.edu/abs/1958RvMP...30.1077S`.

P. H. Sell, S. Heinz, D. E. Calvelo, V. Tudose, P. Soleri, R. P. Fender, P. G. Jonker, N. S. Schulz, W. N. Brandt, M. A. Nowak, R. Wijnands, M. van der Klis, and P. Casella. Parsec-scale Bipolar X-ray Shocks Produced by Powerful Jets from the Neutron Star Circinus X-1. ApJ, 719(2):L194–L198, August 2010. doi: 10.1088/2041-8205/719/2/L194.

M. Serino, K. Tanaka, H. Negoro, H. A. Krimm, J. A. Kennea, P. Romano, H. Tomida, S. Nakahira, M. Ishikawa, Y. E. Nakagawa, T. Mihara, M. Sugizaki, M. Shidatsu, T. Takagi, J. Sugimoto, M. Matsuoka, N. Kawai, M. Arimoto, T. Yoshii, Y. Tachibana, Y. Ono, T. Fujiwara, A. Yoshida, T. Sakamoto, Y. Kawakubo, H. Ohtsuki, H. Tsunemi, R. Imatani, M. Nakajima, T. Masumitsu, Y. Ueda, T. Kawamuro, T. Hori, A. Tanimoto, Y. Tsuboi, S. Kanetou, Y. Nakamura, R. Sasaki, M. Yamauchi, D. Itoh, K. Furuya, K. Yamaoka, and M. Morii. MAXI/GSC and Swift/BAT detections of a new X-ray outburst from MAXI J0911-655/Swift J0911.9-6452. *The Astronomer's Telegram*, 8872:1, March 2016.

N. I. Shakura and R. A. Sunyaev. Black holes in binary systems. Observational appearance. A&A, 24:337–355, January 1973.

S. L. Shapiro and A. P. Lightman. Black holes in X-ray binaries: marginal existence and rotation reversals of accretion disks. ApJ, 204:555–560, March 1976. doi: 10.1086/154203.

Robert E. Shirey, Hale V. Bradt, Alan M. Levine, and Edward H. Morgan. Quasi-periodic Oscillations Associated with Spectral Branches in Rossi X-Ray Timing Explorer Observations of Circinus X-1. ApJ, 506(1): 374–383, October 1998. doi: 10.1086/306247.

Robert E. Shirey, Hale V. Bradt, and Alan M. Levine. The Complete "Z" Track of Circinus X-1. ApJ, 517(1): 472–487, May 1999. doi: 10.1086/307188.

Dmitry Shishkin, Roy Kaye, and Noam Soker. Identifying jittering jet-shaped ejecta in the cygnus loop supernova remnant. *The Astrophysical Journal*, 975(2):281, 2024.

J. Smak. Accretion in cataclysmic binaries. I - Modified alpha-disks with convection. , 32(3-4):199–211, January 1982.

Noam Soker and Dmitry Shishkin. The Vela Supernova Remnant: The Unique Morphological Features of Jittering Jets. *Research in Astronomy and Astrophysics*, 25(3):035008, March 2025. doi: 10.1088/1674-4527/adb4cc.

P. Soleri, S. Heinz, R. Fender, R. Wijnands, V. Tudose, D. Altamirano, P. G. Jonker, M. van der Klis, L. Kuiper, C. Kaiser, and P. Casella. A parsec scale X-ray extended structure from the X-ray binary Circinus X-1. MNRAS, 397(1):L1–L5, July 2009. doi: 10.1111/j.1745-3933.2008.00574.x.

R. E. Spencer, A. P. Rushton, M. Bałucińska-Church, Z. Paragi, N. S. Schulz, J. Wilms, G. G. Pooley, and M. J. Church. Radio and X-ray observations of jet ejection in Cygnus X-2. MNRAS, 435(1):L48–L52, October 2013. doi: 10.1093/mnrasl/slt090.

G. Srinivasan. Recycled pulsars. , 54(3-6):93–100, March 2010. doi: 10.1016/j.newar.2010.09.026.

R. Staubert, J. Trümper, E. Kendziorra, D. Klochkov, K. Postnov, P. Kretschmar, K. Pottschmidt, F. Haberl, R. E. Rothschild, A. Santangelo, J. Wilms, I. Kreykenbohm, and F. Fürst. Cyclotron lines in highly magnetized neutron stars. A&A, 622:A61, February 2019. doi: 10.1051/0004-6361/201834479.

R. T. Stewart, J. L. Caswell, R. F. Haynes, and G. J. Nelson. Circinus X-1: a runaway binary with curved radio jets. MNRAS, 261:593–598, April 1993. doi: 10.1093/mnras/261.3.593.

R. A. Sunyaev and L. G. Titarchuk. Comptonization of X-Rays in Plasma Clouds - Typical Radiation Spectra. A&A, 86:121, June 1980.

Ronald E. Taam and B. A. Fryxell. On Nonsteady Accretion in Stellar Wind–fed X-Ray Sources. ApJ, 327: L73, April 1988. doi: 10.1086/185143.

Y. Tanaka and J. A. M. Bleeker. The diffuse soft X-ray sky. Astrophysics related to cosmic soft X-rays in the energy range 0.1-2.0 keV. Space Sci. Rev., 20(6):815–888, November 1977. doi: 10.1007/BF02431836.

AH Taub. Relativistic rankine-hugoniot equations. *Physical Review*, 74(3):328, 1948.

T. M. Tauris and E. P. J. van den Heuvel. Formation and evolution of compact stellar X-ray sources. In Walter H. G. Lewin and Michiel van der Klis, editors, *Compact stellar X-ray sources*, volume 39, pages 623–665. 2006. doi: 10.48550/arXiv.astro-ph/0303456.

T. M. Tauris, R. P. Fender, E. P. J. van den Heuvel, H. M. Johnston, and K. Wu. Circinus X-1: survivor of a highly asymmetric supernova. MNRAS, 310(4):1165–1169, December 1999. doi: 10.1046/j.1365-8711.1999.03068.x.

B. G. Taylor, R. D. Andresen, A. Peacock, and R. Zobl. The EXOSAT Mission. Space Sci. Rev., 30(1-4): 479–494, March 1981. doi: 10.1007/BF01246069.

Geoffrey Taylor. The Formation of a Blast Wave by a Very Intense Explosion. I. Theoretical Discussion. *Proceedings of the Royal Society of London Series A*, 201(1065):159–174, March 1950. doi: 10.1098/rspa.1950.0049.

A. F. Tennant, A. C. Fabian, and R. A. Shafer. The discovery of X-ray bursts from CIR X-1. MNRAS, 219: 871–881, April 1986. doi: 10.1093/mnras/219.4.871.

V. Tudor, A. Bahramian, G. Sivakoff, L. Chomiuk, C. Heinke, R. Li, T. Maccarone, J. Miller-Jones, R. Plotkin, T. Russell, J. Strader, A. Tetarenko, and E. Tremou. Radio non-detection during nearly-simultaneous Swift/XRT observations of MAXI J0911-635/Swift J0911.9-6452 in NGC 2808. *The Astronomer's Telegram*, 8914:1, April 2016.

V. Tudor, J. C. A. Miller-Jones, A. Patruno, C. R. D'Angelo, P. G. Jonker, D. M. Russell, T. D. Russell, F. Bernardini, F. Lewis, A. T. Deller, J. W. T. Hessels, S. Migliari, R. M. Plotkin, R. Soria, and R. Wijnands. Disc-jet coupling in low-luminosity accreting neutron stars. MNRAS, 470(1):324–339, September 2017. doi: 10.1093/mnras/stx1168.

V. Tudose, R. P. Fender, C. R. Kaiser, A. K. Tzioumis, M. van der Klis, and R. E. Spencer. The large-scale jet-powered radio nebula of Circinus X-1. MNRAS, 372(1):417–424, October 2006. doi: 10.1111/j.1365-2966.2006.10873.x.

V. Tudose, R. P. Fender, A. K. Tzioumis, R. E. Spencer, and M. van der Klis. A decade of radio imaging the relativistic outflow in the peculiar X-ray binary CircinusX-1. MNRAS, 390(1):447–464, October 2008. doi: 10.1111/j.1365-2966.2008.13788.x.

V. Tudose, R. P. Fender, M. Linares, D. Maitra, and M. van der Klis. The disc-jet coupling in the neutron star X-ray binary Aquila X-1. MNRAS, 400(4):2111–2121, December 2009. doi: 10.1111/j.1365-2966.2009.15604.x.

John E. Vaillancourt. Placing Confidence Limits on Polarization Measurements. PASP, 118(847):1340–1343, September 2006. doi: 10.1086/507472.

J. van den Eijnden, N. Degenaar, T. D. Russell, R. Wijnands, A. Bahramian, J. C. A. Miller-Jones, J. V. Hernández Santisteban, E. Gallo, P. Atri, R. M. Plotkin, T. J. Maccarone, G. Sivakoff, J. M. Miller, M. Reynolds, D. M. Russell, D. Maitra, C. O. Heinke, M. Armas Padilla, and A. W. Shaw. A new radio census of neutron star X-ray binaries. MNRAS, 507(3):3899–3922, November 2021. doi: 10.1093/mnras/stab1995.

M. van der Klis. The Z/atoll Classification. In J. Hunt and B. Battrick, editors, *Two Topics in X-Ray Astronomy, Volume 1: X Ray Binaries. Volume 2: AGN and the X Ray Background*, volume 1 of *ESA Special Publication*, page 203, November 1989.

M. van der Klis. Similarities in Neutron Star and Black Hole Accretion. ApJS, 92:511, June 1994. doi: 10.1086/192006.

M. van der Klis. Kilohertz Quasi-Periodic Oscillations in Low-Mass X-Ray Binaries. In R. Buccheri, J. van Paradijs, and A. Alpar, editors, *The Many Faces of Neutron Stars.*, volume 515 of *NATO Advanced Study Institute (ASI) Series C*, page 337, January 1998.

Jan van Paradijs and Frank Verbunt. A comparison of soft x-ray transients and dwarf novae. In S. E. Woosley, editor, *High Energy Transients in AstroPhysics*, volume 115 of *American Institute of Physics Conference Series*, pages 49–62. AIP, May 1984. doi: 10.1063/1.34556.

Steve van Straaten, Michiel van der Klis, and Mariano Méndez. The Atoll Source States of 4U 1608-52. ApJ, 596(2):1155–1176, October 2003. doi: 10.1086/378155.

D. A. Verner, G. J. Ferland, K. T. Korista, and D. G. Yakovlev. Atomic Data for Astrophysics. II. New Analytic FITS for Photoionization Cross Sections of Atoms and Ions. ApJ, 465:487, July 1996. doi: 10.1086/177435.

Paul Vreeswijk and Kerry Paterson. BlackBOX: BlackGEM and MeerLICHT image reduction software, May 2021.

N. E. White, J. L. Kaluzienski, and J. H. Swank. The spectra of x-ray transients. In S. E. Woosley, editor, *High Energy Transients in AstroPhysics*, volume 115 of *American Institute of Physics Conference Series*, pages 31–48. AIP, May 1984. doi: 10.1063/1.34536.

N. E. White, A. Peacock, G. Hasinger, K. O. Mason, G. Manzo, B. G. Taylor, and G. Branduardi-Raymont. A study of the continuum and iron K line emission from low-mass X-raybinaries. MNRAS, 218:129–138, January 1986. doi: 10.1093/mnras/218.1.129.

N. E. White, L. Stella, and A. N. Parmar. The X-Ray Spectral Properties of Accretion Disks in X-Ray Binaries. ApJ, 324:363, January 1988. doi: 10.1086/165901.

Rudy Wijnands and Michiel van der Klis. The Broadband Power Spectrum of SAX J1808.4-3658. ApJ, 507(1): L63–L66, November 1998a. doi: 10.1086/311676.

Rudy Wijnands and Michiel van der Klis. A millisecond pulsar in an X-ray binary system. Nature, 394(6691): 344–346, July 1998b. doi: 10.1038/28557.

Rudy Wijnands, Jeroen Homan, Michiel van der Klis, Erik Kuulkers, Jan van Paradijs, Walter H. G. Lewin, Frederick K. Lamb, Dimitrios Psaltis, and Brian Vaughan. Discovery of kHz Quasi-periodic Oscillations in the Z Source Cygnus X-2. ApJ, 493(2):L87–L90, February 1998. doi: 10.1086/311138.

David Williams, Sara Motta, Rob Fender, Patrick Woudt, and James Miller-Jones. MeerKAT detection of SAXJ1808.4-3658 at 1.3 GHz. *The Astronomer's Telegram*, 13026:1, August 2019.

J. Wilms, A. Allen, and R. McCray. On the Absorption of X-Rays in the Interstellar Medium. ApJ, 542(2): 914–924, October 2000. doi: 10.1086/317016.

Weiqun Zhang and Andrew MacFadyen. The Dynamics and Afterglow Radiation of Gamma-Ray Bursts. I. Constant Density Medium. ApJ, 698(2):1261–1272, June 2009. doi: 10.1088/0004-637X/698/2/1261.

J. T. L. Zwart, R. W. Barker, P. Biddulph, D. Bly, R. C. Boysen, A. R. Brown, C. Clementson, M. Crofts, T. L. Culverhouse, J. Czeres, R. J. Dace, M. L. Davies, R. D'Alessandro, P. Doherty, K. Duggan, J. A. Ely, M. Felvus, F. Feroz, W. Flynn, T. M. O. Franzen, J. Geisbüsch, R. Génova-Santos, K. J. B. Grainge, W. F. Grainger, D. Hammett, R. E. Hills, M. P. Hobson, C. M. Holler, N. Hurley-Walker, R. Jilley, M. E. Jones, T. Kaneko, R. Kneissl, K. Lancaster, A. N. Lasenby, P. J. Marshall, F. Newton, O. Norris, I. Northrop, D. M. Odell, G. Petencin, J. C. Pober, G. G. Pooley, M. W. Pospieszalski, V. Quy, C. Rodríguez-Gonzálvez, R. D. E. Saunders, A. M. M. Scaife, J. Schofield, P. F. Scott, C. Shaw, T. W. Shimwell, H. Smith, A. C. Taylor, D. J. Titterington, M. Velić, E. M. Waldram, S. West, B. A. Wood, G. Yassin, and AMI Consortium. The Arcminute Microkelvin Imager. MNRAS, 391(4):1545–1558, December 2008. doi: 10.1111/j.1365-2966.2008.13953.x.